NORTHWESTERN UNIVERSITY

Theoretical Study of Model Atom + Polyatom Reactions in the Gas Phase:

Adiabatic and Nonadiabatic Dynamics

A DISSERTATION

SUBMITTED TO THE GRADUATE SCHOOL

IN PARTIAL FULFILLMENT OF THE REQUIREMENTS

for the degree

DOCTOR OF PHILOSOPHY

Field of Chemistry

By

Wenfang Hu

EVANSTON, ILLINOIS

December 2007

ABSTRACT

Theoretical Study of Model Atom + Polyatom Reactions in the Gas Phase:

Adiabatic and Nonadiabatic Dynamics

Wenfang Hu

Direct dynamics quasiclassical trajectory (QCT) calculations are performed to study the dynamics of model atom + polyatom reactions. In the first part of this thesis, we examine adiabatic dynamics of H/O reaction with simple alkanes, CD_4 and C_2H_6. Overall good agreement with state-of-the-art experiments shows that the molecular motion is largely confined to the ground electronic potential energy surface (PES). For the $H + CD_4$ abstraction reaction, we consider several PESs, including an analytical surface EG, and the B3LYP/6-31G** surface. The best agreement with experiment over the 1.21—2.36 eV collision energy range is found on the B3LYP surface. In particular, the CD_3 products are broadly sideways scattered at 1.2 eV and shift to backward directions as energy increases, indicating the increasing importance of the stripping mechanism. Regions of the surface away from the minimum energy path are found to play an important role in high-energy dynamics.

We further study the hyperthermal $O(^3P)$ collisions with C_2H_6 for understanding materials erosion of spacecraft in low Earth orbit. By running QCT trajectories on the MSINDO and B3LYP/6-31G** surfaces, we examine the dynamics associated with the three primary reaction channels, H abstraction, H elimination and C-C breakage, and achieve generally good agreement with experiment as to product translational and angular distributions and the product relative yields at 90 kcal mol^{-1}.

In the second part, our focus is on chemical reactions where the Born-Oppenheimer approximation breaks down. Specifically we study intersystem crossing effects in the $O(^3P)$ + C_2H_4 reaction at a low collision energy of 0.56 eV, and at a hyperthermal energy of 3.0 eV. We use a simplified version of the trajectory surface hopping method with surface transitions only allowed at the triplet—singlet crossing points along the B3LYP/6-31G** trajectory. The transition probability is evaluated according to the Landau-Zener formula and we use an average spin-orbit coupling throughout our calculations. Our results show reasonable agreement with the low energy experiment as to the product branching ratios, product energy and angular distributions. Dynamics at hyperthermal energy differs from low energy dynamics due to decreased intersystem crossing and novel reaction pathways that are open at high energy.

To my husband, Long Zhang, and my son, Chuyang Zhang

Acknowledgements

During my five years of graduate study at Northwestern, I have met, worked and had fun together with many people who contributed either directly or indirectly to the completion of this thesis work.

First of all, I would like to express my deep gratitude to my supervisor, Prof. George C. Schatz. Thanks for all the invaluable science discussions, advice and encouragements! Your enthusiasm, creativity and unique insight in pursuing the truth of the objective world will continue to guide me in my future career.

I am very grateful to all my collaborators for their selfless help and diligent work. Prof. Diego Troya led me into the world of theoretical chemical dynamics when I was still an innocent junior student in the group. Dr. György Lendvay has been teaching me hand-by-hand not only the methodologies but also the correct attitudes of doing scientific research throughout my graduate study. Prof. Biswajit Maiti actually initiated the O (^3P) + ethylene project and taught me a lot on the subject of nonadiabatic dynamics. We also had many interesting talks about life and about India and China. I also have had the pleasure of working with experimentalists Dr. Jon Camden and Prof. Richard Zare at Stanford University, and Dr. Donna Minton and Prof. Timothy Minton at Montana State University. They have been kind and helpful in answering and fixing problems together with me. Through many enlightening discussions with them, I got to learn thinking from the perspective of an experimentalist.

I should thank many of the theory group members for making Northwestern a nice place to stay. Dr. Hai Long, Dr. Lipeng Sun, Prof. Christine Aikens, Dr. Neil Snider and Dr. Baudilio Tejerina, thank you all for always having time to help solve my

problems, no matter how small they are. Dr. Linlin Zhao, Jing Zhao and Dr. Shuzhou Li, I will miss our friendship when I am away. And thanks for many other people in the group, Prof. Shengli Zou, Martin McCullagh, Prof. Mark Ratner, Dr. Jeff Paci, Dr. Shahar Keinan, Prof. Hyonseok Hwang, Prof. Yongqiang Xue …

And my committee members, Prof. Tamar Seideman, Prof. Eric Weitz and Prof. Kenneth Spears, many thanks for your kind advice and "criticism" on my research and encouragements about my future development.

I am also appreciative to many people who helped me since I came to the US. Dr. Chang Zhong and Dr. Bin Deng picked me up at the airport and found me a place to live for the first month. My host family, Kim Suez and George Huang, helped me to adjust to the new life in America. Prof. Franz Geiger introduced me into his lab for the summer of 2002. And a lot of other people I have to thank: Hu Kang, Zhongqiang Liu, Dong Lu, Li Zeng, Huihe Zhu, Xiaoyu Zhang …

I am greatly indebted to my parents for their constant love. They are always there for me at every up-and-down moment of my life. And my sister and brother-in-law for sharing my joy and sadness.

Lastly, very special thanks to my husband, Long Zhang, and my son, Chuyang Zhang for supporting me selflessly during these years. They sacrifice a lot to help me overcome many barriers in my life and study, and they have to bear with my bad temper. Many thanks to my mother-in-law and her family for taking care of my son in China after he was one year old.

Thank you all!

Table of Contents

List of Tables

List of Figures

Chapter 1

Introduction

1.1 Overview of the History

Chemists' long sought-after goal of controlling chemical reactions to synthesize new structures and new materials dates back to even thousands of years ago when alchemists in ancient Egypt, Mesopotamia, as well as in China tried to conjure gold out of cheaper elements. Nowadays, the production of salt from the acid-base reaction between HCl (aq) and NaOH (aq) is a routine practice in high school chemistry classes. Chemical reactions may follow more than one reaction pathway, each leading to a different product. Through manipulating the external conditions such as temperature and pressure, or using a catalyst to alter the course of a reaction, chemists can now successfully guide a chemical reaction to yield the desired products and suppress

unwanted side products.[1] But the task of today's Chemistry doesn't stop there! To achieve a fundamental understanding of chemical reactivity and ultimately to accomplish chemical control at will, one needs to delve into the world of atoms and molecules: what are the microscopic forces that are at work for the breaking and making of chemical bonds during a chemical reaction? This is exactly what experimental and theoretical reaction dynamics[2] are seeking to answer.

To put it simply, chemical dynamics attempts to view the very process of chemical change itself at the molecular level.[3] This field of study is essentially the modern-day approach to the macroscopic chemical kinetics. The traditional chemical kinetic study relies heavily on empiricism. A famous example is the Arrhenius law that reveals the temperature dependence of the rate constant:[4]

$$k(T) = A \exp\left(-\frac{E_a}{RT}\right) \tag{1-1}$$

where E_a is the experimental activation energy, A is the pre-exponential factor and R is the molar gas constant. This simple model is remarkably successful at explaining experimental observations of many chemical and physical rate processes. The relationship between the rate constant of a reaction and the temperature led to the conclusion that there is an energy barrier to reaction. It was also recognized that intermolecular collisions serve as the microscopic mechanism "underneath" elementary chemical processes.[5,6] In most cases reaction does not invariably occur when the reactant molecules collide with each other. They must possess a critical amount of energy along their line of centers; the relative orientations should also be suitable.

The first attempt to rationalize the form of the Arrhenius equation was made by Trautz[5] and Lewis,[6] who treated the reactant molecules A and B as structureless hard spheres. By equating the reaction rate with the collision frequency between A and B, Z_{AB}, the resulting expression for the thermal rate constant is simply:

$$k(T) = Z_{AB} = \left(\frac{8k_B T}{\pi \mu} \right)^{1/2} \sigma_R \qquad (1\text{-}2)$$

The first term on the right-hand side is the average relative speed of the reactants, while $\sigma_R = \pi \left(r_A + r_B \right)^2 = \pi d^2$ is the collision cross section in this hard-sphere collision model. Equation (1-2) predicts a temperature dependence of $T^{1/2}$ for $k(T)$. This model is oversimplified in that the reactant molecules do not interact ($P_R = 0$) if the intermolecular distance $r_{AB} > d$, but react otherwise, i.e., $P_R \left(r_{AB} \leq d \right) = 1$. Clearly a more elaborate model should at least account for the energy-dependence of the reaction cross section σ_R. In the reactive hard sphere model, we consider a collision between hard-sphere molecules A and B characterized by a relative kinetic energy ε_r and an impact parameter b, defined as the distance of closest approach between A and B in the absence of inter-particle forces. The reaction occurs only if the energy "directed" along the line of centers $\varepsilon_r \left(1 - \dfrac{b^2}{d^2} \right)$ is larger than a threshold energy ε_a. The reaction cross section is thus given by:

$$\sigma_R = \begin{cases} 0 & \varepsilon_r < \varepsilon_a \\ \pi d^2 \left(1 - \dfrac{\varepsilon_a}{\varepsilon_r}\right) & \varepsilon_r \geq \varepsilon_a \end{cases} \qquad (1\text{-}3)$$

And the rate constant is:

$$k(T) = \pi d^2 \left(\frac{8k_B T}{\pi \mu}\right)^{1/2} \exp\left(-\frac{\varepsilon_a}{k_B T}\right) \qquad (1\text{-}4)$$

which has a corresponding form to the Arrhenius equation.

The limitations of the simple collision models are obvious: molecules are simply not hard spheres. The intermolecular interactions are far more complex than is observed between two ping-pang balls in the macroscopic world (We will later know that the nuclear motion is governed by a potential energy surface). However, these valuable efforts embody the physical essence of an actual chemical reaction and introduce many important concepts of scattering theory.

The transition state theory (TST), which was introduced by Eyring[7] and by Evans and Polanyi[8] in 1935, deals with molecular collisions in a more satisfactory way by taking into account the structures of the reacting molecules. This theory focuses attention on a transition state intermediate corresponding to the saddle point region on the potential energy surface. The transition state separates reactants from products with a "dividing surface" orthogonal to the reaction coordinate. By assuming that the reactants are in thermal equilibrium with the transition state, the resulting expression for the rate constant of a reaction is

$$k(T) = \frac{k_B T}{h} \frac{Q^{\neq}}{Q} e^{-E_0/RT} \qquad\qquad (1\text{-}5)$$

where Q and $Q^{\neq}$ are the partition functions of the reactants and transition state and E_0 is the difference in zero-point energy between the transition state and the reactants.

It has been recognized since the early days of its development that TST is a model essentially based on classical mechanics. The theory is exact if the trajectories that have crossed the dividing surface do not turn back and reform the reactant molecules. This assumption leads to an overestimation of the correct classical mechanical rate constant. Over the years, sustained efforts have been made to improve on the conventional TST. In particular, the variational TST has been developed to optimize the dividing surface in order to minimize the rate constant.[9] There are also advances in incorporating quantum effects in the formulation of TST.[10]

Although TST has been rather successful in describing a wide variety of rate processes in the gas phase, in liquids, at interfaces, and in biological systems,[11] it is basically a statistical theory based on the equilibrium hypothesis (i.e., the transition state is in equilibrium with the reactants), which is questionable in many cases such as in fast reactions. Furthermore, there are many situations where one is interested in understanding the detailed molecular dynamics of a chemical reaction.

Over the past few decades, we have witnessed tremendous progress in the field of chemical reaction dynamics both experimentally and theoretically. On the experimental front, advances in crossed molecular beam and state-resolved spectroscopic techniques

have furnished an unprecedented level of information about the mechanistic details of chemical changes.[12] More recently, femtosecond lasers have emerged as a powerful tool for realizing quantum control of chemical reactions.[12(d)]

The prerequisite for a theoretical treatment of collision dynamics is the potential energy surfaces, which are the "maps" that plot potential energy against the geometry of molecular systems. What is implicit in the concept of PES is the Born-Oppenheimer separation of nuclear and electronic motion. The fast moving electrons adjust instantaneously to changes in nuclei configuration so that the nuclei can be considered to move along a potential surface derived from a single electronic state. The first PES was reported in 1931 by Eyring and Polanyi[13] for the hydrogen exchange reaction $H + H_2$. In their original paper, Eyring and Polanyi did include a dynamical treatment of classical motion over the PES. For many years after that, a number of attempts were made to describe the dynamics for this simplest chemical reaction using either classical trajectory or quantum scattering calculations. There is no difficulty in principle in carrying out such dynamical studies, but as Paul Dirac said, "… and the difficulty lies only in the fact that application of these laws leads to equations that are too complex to be solved". In addition, construction of the PES, especially for a polyatomic system with many degrees of freedom, poses formidable challenges. It was not until the 1970s that realistic applications to $H + H_2$ and other reactions became feasible.[14] The dynamics of simple reactions in the gas phase are now understood at an impressive level of detail, thanks to advances in experimental technology and computer power.

1.2 The Multi-dimensional Challenge

The focal point of earlier dynamics studies has been atom + diatom reactions. This is natural considering that there are only three internal degrees of freedom that need to be explicitly treated. However, even in the gas phase, chemical processes are usually much more complex than the model three atom systems. Challenges associated with studying polyatomic reactions are multiple.[15] First of all, the number of *ab initio* points required to fit a PES to chemical accuracy increases exponentially with the dimension of the molecular system. For a nonlinear N atom system, there are $3N$-6 degrees of freedom in the center-of-mass frame. If we calculate 10 points per dimension, a total of 10^3 points are needed to define the PES for a three-atom system. For an atom plus triatom system, the number of points increases rapidly to 10^6. Secondly, there are many more reaction channels that can happen in a polyatomic system than in a triatomic system. For example, for an atom-diatom system A + BC, the possible reaction channels are:

$$A + BC \rightarrow AB + C \qquad \text{Abstraction I}$$

$$A + BC \rightarrow AC + B \qquad \text{Abstraction II}$$

$$A + BC \rightarrow ABC \qquad \text{Addition}$$

$$A + BC \rightarrow A + B + C \qquad \text{Fragmentation}$$
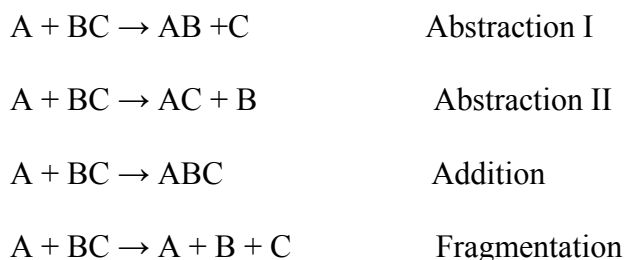
While for a four atom system, there are a total of 17 possible arrangements of the atoms, although the actual outcome depends on aspects such as the initial conditions and the PES. Thirdly, there are many more energetically accessible quantum states in the

polyatomic reactants and products. A diatom can only stretch along the bond axis. How energy is utilized and disposed in the translational and internal modes of an atom + diatom reaction can be described by the Polanyi rules.[16] However, the situation is less clear cut for a polyatomic reaction, owing to the fact that the many degrees of freedom could be strongly coupled during reaction. Additional challenges include that chemical reactions vary widely in their dynamical behaviors. Some reactions are direct, some are multi-step processes involving formation of long-lived intermediate complexes, some in which tunneling and resonance effects play important roles in the dynamics, and others occur on multiple coupled potential surfaces. This complexity is even more pronounced as the dimension of the problem gets expanded.

However difficult the problem might be, theoretical and experimental chemical dynamicists have been consistently making progress in exploring new frontiers of chemistry. These include complex reactions in the gas phase, at surfaces, in solutions, or in biological systems. This process has benefited greatly from the development of novel theoretical and computational tools, as well as the application of these tools to challenging chemical problems. The goal of theoretical dynamics is not merely to reproduce experimental results. Theory helps to uncover the underlying mechanisms that cannot feasibly be studied experimentally and make quantitative predictions to further guide the experimental observations.[17, 18]

1.3 Outline of the Contents

The work presented in this thesis emphasizes the use of "on the fly" quasiclassical trajectories to describe molecular collision processes involving an atom and short chain saturated and unsaturated hydrocarbons. Our focus in the first part (Chapters 3 and 4) is on electronically adiabatic processes, i. e., nuclear motion can be assumed to evolve on a single electronic potential energy surface. The second part (chapter 5) is treatment of nonadiabatic transitions in spin forbidden reactions.

Chapter 2 introduces the basic theory and strategy for solving reactive scattering problems in the gas phase. We also describe in detail the methodologies that we employ to explore adiabatic and nonadiabatic dynamics of atom + polyatom systems: the quasiclassical trajectory and trajectory surface hopping methods.

Chapters 3 and 4 present combined theoretical and experimental investigations of the dynamics associated with the ground state $H + CD_4$ and $O + C_2H_6$ reactions. Specifically, we study the effects of reagent relative translation on chemical reactivity and on the product distributions. We have achieved overall good agreement between experiment and theory for various dynamical properties examined.

Although many chemical reactions can be described adequately within the adiabatic hypothesis, many involve nonadiabatic transitions between neighboring electronic potential energy surfaces. In chapter 5, we show that spin-orbit coupling

induced intersystem crossing effects play a crucial role in determining the product relative yields in the O (^3P) + C_2H_4 reaction.

Chapter 2   Theories of Chemical Reaction Dynamics

2.1 The General Theory

Quantum mechanics is the prevalent theory of the basic constituents of the world and their dynamics. Just as Newton's laws describe the motion of macroscopic objects, the Schrödinger equation[19] predicts the behavior of particles in the microscopic world. In the nonrelativistic picture, the time-dependent Schrödinger equation reads

$$i\hbar \frac{\partial \Psi}{\partial t} = \left(-\frac{\hbar^2}{2m}\nabla^2 + V \right)\Psi = \hat{H}\,\Psi \qquad (2\text{-}1)$$

where Ψ is the time dependent wavefunction, and $\hat{H}$ is the Hamiltonian operator which consists of two parts that describe the particle kinetic energy and potential energy, respectively. The Hamiltonian may be time independent or time dependent. In the case of

chemical reactions, $\hat{H}$ is usually time independent during the collision event. Then a formal solution to Eq. (2-1) is given by

$$\Psi(t) = \Psi(t=0)e^{-i\hat{H}t/\hbar} \qquad (2\text{-}2)$$

The time dependent Schrödinger equation then reduces to the time independent Schrödinger equation, which for a general molecular system consisting of N nuclei and n electrons is

$$\hat{H}\psi(R,r) = E\psi(R,r) \qquad (2\text{-}3)$$

Here ψ is the molecular wavefunction, R and r are collective indexes that denote the nuclear and electron coordinates, respectively, and E is the total energy of the system. In atomic units, the Hamiltonian is written as

$$H(r,R) = T_N(R) + T_e(r) + V_{NN}(R) + V_{eN}(r,R) + V_{ee}(r)$$

$$= -\sum_I^N \frac{1}{2M_I}\nabla_I^2 - \sum_i^n \frac{1}{2}\nabla_i^2 + \sum_I^N\sum_{J<I}^N \frac{Z_I Z_J}{R_{IJ}} - \sum_I^N\sum_i^n \frac{Z_I}{|\mathbf{R}_I - \mathbf{r}_i|} + \sum_i^n\sum_{j<i}^n \frac{1}{r_{ij}} \qquad (2\text{-}4)$$

where T_N and T_e are, respectively, the nuclear and electron kinetic energy operators, V_{NN}, V_{eN} and V_{ee} include all the nuclear-nuclear, electron-nuclear and electron-electron interactions, M_I is the nuclear mass, Z_I is the nuclear charge, R_{IJ} is the distance between nuclei I and J, and r_{ij} is the distance between electrons i and j.

Since the nuclear mass is much larger than the mass of electrons, electrons can adjust instantaneously to the slow motion of nuclei during the course of a reaction. We

then write the total wavefunction as a product of the nuclear function $\chi(R)$ and the electronic function $\phi(r, R)$

$$\psi(R, r) = \chi(R)\phi(r, R) \tag{2-5}$$

and the electronic and nuclear motion are decoupled as

$$\hat{H}_{el}\,\phi(r, R) = \varepsilon_{el}(R)\phi(r, R) \tag{2-6}$$

$$\hat{H}_{el} = T_e(r) + V_{NN}(R) + V_{eN}(r, R) + V_{ee}(r) \tag{2-7}$$

$$\left[\hat{T}_N + \varepsilon_{el}(R)\right]\chi(R) = E\chi(R) \tag{2-8}$$

This adiabatic separation of electronic and nuclear motions is known as Born-Oppenheimer approximation.[20] For each nuclear configuration (R fixed), there exists a set of adiabatic eigenfunctions $\phi_n(r, R)$ and eigenvalues $\varepsilon_n(R)$ that satisfy Eq. (2-6)

$$\hat{H}_{el}\,\phi_n(r, R) = \varepsilon_n(R)\phi_n(r, R) \tag{2-9}$$

Solving the nth electronic Schrödinger equation for an ensemble of nuclear geometries, we obtain the potential energy surface for the nth electronic state.

To describe molecular collisions on the adiabatic potential surfaces, it is desirable to do the calculations quantum mechanically by solving either the time dependent or time independent Schrödinger equation for the nuclear motion. However, exact quantum scattering calculations are still limited to very small chemical systems involving three and even four atoms.[21, 22] As the dimensionality of a system increases, the numerical effort associated with such calculations rapidly outgrows the capacity of current computers. A

variety of approximate quantum mechanical, as well as classical and mixed quantum/classical methods are thus important in extending theory to more complex problems.[23-27] As long as the de Broglie wavelength is short compared to the distances over which atoms move during a collision, which is typical of most chemical processes, classical and semiclassical theories are useful. In the quasiclassical trajectory (QCT) method, quantum conditions are imposed by letting the reactant molecules have quantized internal energies, but the actual motion over the PES is treated classically.[24(a)] This is the basic technique we used in our dynamical studies of atom + polyatom reactions, so we will discuss the method in detail later.

Some chemical systems may be modeled adequately within the framework of the Born-Oppenheimer approximation. However, there are occasions when it is not possible to separate the nuclear and electronic motion. It is true when the nuclear kinetic energy is not very small as compared to the energy gaps between adiabatic electronic states so that the nuclear motion can cause transitions between these states.[28] A proper theoretical treatment of nonadiabatic processes may be developed by expanding the total molecular wavefunction $\psi(R,r)$ in the adiabatic basis $\phi_n(r,R)$ [29]

$$\psi(R,r) = \sum_n \chi_n(R)\phi_n(r,R) \qquad (2\text{-}10)$$

Here the nuclear functions act as the expansion coefficients. Substituting the expansion into Eq. (2-3), we obtain, after integrating over the electronic coordinates, the coupled equations

$$\left[T_N(R)+V_{mm}(R)+T^{"}_{mm}(R)-E\right]\chi_m(R)=-\sum_{n\neq m}\left[T^{'}_{mn}(R)+T^{"}_{mn}(R)+V_{mn}(R)\right]\chi_m(R) \quad (2\text{-}11)$$

where

$$V_{mn}(R)=\langle\phi_m|H_{el}|\phi_n\rangle \qquad (2\text{-}12)$$

$$T^{'}_{mn}=\sum_I-\frac{1}{2M_I}\langle\phi_m|\nabla_I\,\phi_n\rangle\cdot\nabla_I \qquad (2\text{-}13)$$

$$T^{"}_{mn}=\sum_I-\frac{1}{2M_I}\langle\phi_m|\nabla_I^2\,\phi_n\rangle \qquad (2\text{-}14)$$

The diagonal terms V_{mm} are the effective potential energy surfaces that govern nuclear motion. The terms $T^{'}_{mn}$ and $T^{"}_{mn}$ arise from the action of the nuclear momentum and kinetic energy operators on electronic basis functions. The off-diagonal terms $T^{'}_{mn}$, $T^{"}_{mn}$, and V_{mn} are nonadiabatic couplings between different adiabatic states. Note that the diagonal terms $T^{'}_{mm}$ are zero, and $T^{"}_{mn}$, both diagonal and off-diagonal, are very small and generally neglected.

In the adiabatic representation, V_{mn} is diagonal and the nuclear motion is coupled only by $T^{'}_{mn}$. These matrix elements are vectors and are typically small when the adiabatic surfaces are well separated. But they become large when two surfaces come close and are infinitely large when they meet, which means that the Born-Oppenheimer approximation is no longer valid. Although the adiabatic representation is well defined and one can calculate directly the adiabatic wavefunctions by electronic structure theory, it is not particularly convenient to compute the nonadiabatic coupling matrix. Thus in

solving nonadiabatic problems, one can instead adopt the diabatic representation. This is achieved by a unitary transformation of the adiabatic electronic wavefunctions at each point in space

$$\phi_n(r,R) = \sum_n D_{mn}(R)\varphi_m(r,R) \qquad (2\text{-}15)$$

In doing so, one wants to make the vector coupling terms T'_{mn} small enough to be neglected, so that the nuclear motion is only coupled by off-diagonal elements (V_{mn} are scalars) of the electronic Hamiltonian. In the diabatic representation, both the diabatic wavefunctions and nonadiabatic couplings are smooth functions of $\hat{\mathbf{R}}$, so it is easier to develop analytic expressions for the potential surfaces and their couplings. A detailed discussion of the strengths and weakness associated with each representation can be found in reference 30.

So far we have only considered nonadiabatic couplings that can cause transitions between surfaces of different electronic symmetries, but not of different spins. Transitions involving different spin states can be induced by spin-orbit couplings. The effect of spin-orbit interaction can be included by simply replacing $V_{mn}(R)$ in Eq. (2-11) with $W_{mn}(R)$, both diagonal and off-diagonal

$$W_{mn}(R) = \left\langle \phi_m \left| H_{el} + H_{SO} \right| \phi_n \right\rangle \qquad (2\text{-}16)$$

The coupled equation (2-11) involves a complete, infinite set of electronic states. Fortunately, owing to the nature of the nonadiabatic coupling, the electronic basis can be truncated to include only those states that are strongly coupled.

Nonadiabatic dynamics are inherently quantum mechanical due to the coupling between the nuclei and the electrons. However, accurate quantum mechanical calculations of nonadiabatic processes are presently limited to very small systems and involve only two electronic states. For polyatomic systems, one must therefore resort to semiclassical methods where the nuclear motion is treated classically, whereas the transitions between electronic states are treated by quantum mechanics.[31, 32] One of the most common approaches based on classical trajectories is the trajectory surface hopping (TSH) method,[26] in which the nuclear trajectory is propagated on the potential surface that corresponds to the currently occupied state. The propagation is interrupted by instantaneous transitions to other states according to hopping probabilities that are computed along the trajectory. From practical considerations, one may express the electronic states and their couplings in either the adiabatic or diabatic representation. This method has been successfully applied to such diverse systems as gas phase ion-molecule reactions and electronic relaxation on surfaces. In our dynamical simulation of intersystem crossing (ISC) effects in the $O(^3P)$ + ethylene reaction, the calculations were simplified somewhat by considering transition between surfaces only at the crossing points.

Before any dynamics may be carried out, one needs an accurate representation of the potential energy surface, or a set of potential energy surfaces and their couplings for nonadiabatic problems. Conventional strategy is to represent the PESs and couplings using analytical functions fit to high quality *ab initio* calculations and experiments.[33, 34]

But the complete construction of an analytical PES can be lengthy and difficult. For high-dimension systems, this very often involves dealing with only the reactive degrees of freedom and keeping others as spectators. There have been many reviews of the technology developed for surface fitting.[35] Alternatively, one can generate the potential surface from electronic structure calculations carried out "on the fly" (i.e., as the trajectory propagates).[36, 37] This so-called direct dynamics methodology is particularly appealing for studying polyatomic reactions in full dimensionality, where multiple reaction channels are open. However, in order to achieve a compromise between computational accuracy and efficiency, the implementation is presently limited to only relatively low level electronic structure theories such as the Hartree-Fock (HF) method, the density functional theory (DFT) methods, and even semiempirical methods.

2.2 The Quasiclassical Trajectory Method

Quantum mechanics is the ultimate solution to chemical dynamics problems, but its applications are largely limited to relatively small systems due to computational complexity. Frequently classical mechanics is employed as an approximate alternative.[38]

The first classical trajectory study was performed by Hirschfelder, Eyring, and Topley for the H + H_2 reaction in 1936.[39] The QCT treatment today basically follows the original work of Karplus, Porter and Sharma for the same reaction.[24(a)] Despite its widespread use, the QCT method suffers from several shortcomings which can be

problematic. There are two main sources of errors. The first relates to the fact that a classical treatment neglects the quantization at the transition states and at the other points during the trajectory. The zero-point energy (ZPE) can constitute a large part of the total energy, especially for large molecules at thermal energies. The ZPE of the reactant molecules can leak to the reaction coordinate, thus permits the reaction barrier to be surmounted at energies that are lower than the zero-point level. There are several attempts to try to fix the ZPE problem.[40] The second source of error is the omission of quantum mechanical tunneling through the barrier. Note that this problem may be partially compensated for by the absence of ZPE restrictions using classical mechanics. Progress has also been made in incorporating quantum effects in classical dynamics simulations.[41] However, the QCT method is very appealing in that it is simple and straightforward as compared to quantum dynamics. Given enough sampling of initial conditions, QCT results are generally in pretty good agreement with experiment, in particular for averaged quantities such as thermal rate constants.[42,43]

In the standard QCT method,[38] the reagent molecules are given initial coordinates and momenta that mimic whatever quantum states are of interest. One then integrates the classical equations of motion numerically to simulate intermolecular collisions. At the end of each trajectory, the final coordinates and momenta are analyzed to extract scattering information, such as state-resolved product distributions.

2.2.1 Initial Conditions

For a reaction system composed of N atoms, we need to specify a set of N coordinate vectors (q_{ix}, q_{iy}, q_{iz}) and N momentum vectors (p_{ix}, p_{iy}, p_{iz}) in the Cartesian coordinate system, corresponding to separated reagents that are moving towards each other with a specified velocity and impact parameter, and with the reagent molecules in specified quantum states. In quantum mechanics, however, the uncertainty principle states that only one of position and momentum of a microscopic particle can be specified at a time. In order to mimic this quantal aspect in classical mechanics, we need to run many QCT trajectories, each having a definite outcome. The initial conditions of these trajectories are sampled randomly, usually done using the Monte Carlo procedure,[44] and by averaging over the trajectory outcomes, we calculate dynamical observables that can be compared with experiment.

In classical trajectories, vibrational and rotational states of the reactant and product molecules are specified by action variables, which are the classical analogs of quantum numbers. Appropriate determination of these actions is essential in obtaining state-to-state information of the reaction dynamics.[42, 45, 46] The semiclassical eigenstates of a system are well defined only if vibration/rotation is quasiperiodic, which means that the molecular motion is confined to the surface of a torus in phase space. For studies of molecules with relatively low internal excitation, such as in the ground state, a normal-mode sampling procedure will normally suffice.[47]

We begin by considering nonrotating systems in which anharmonicity and the various mode couplings are unimportant. The system Hamiltonian is simply

$$H = \sum_k \frac{P_k^2}{2} + \frac{\omega_k^2 Q_k^2}{2} \qquad (2\text{-}17)$$

where the summation is over the vibrational degrees of freedom, ω_k is the k th normal mode harmonic frequency. P_k and Q_k are the corresponding momenta and coordinates.

Semiclassically, the vibrational action variable $\left(\upsilon_k + \frac{1}{2} \right) h = \oint_{C_k} P_k dQ_k$ is quantized,[48, 49] where υ_k is the vibrational quantum number, and C_k specifies a closed contour in phase space that encircles the state-specified torus. At the end of a QCT trajectory, it is usually needed to round off the continuous υ_k to the nearest integer in order to determine the product quantum state. The normal mode P_k and Q_k can be described in terms of the conjugate phase angle θ_k by

$$P_k = -\sqrt{(2\upsilon_k + 1)\omega_k} \, \sin\theta_k \qquad (2\text{-}18)$$

$$Q_k = \sqrt{\frac{(2\upsilon_k + 1)}{\omega_k}} \cos\theta_k \qquad (2\text{-}19)$$

By randomly selecting the θ_k value between 0 and 2π, Eqs. (2-18) and (2-19) give the normal mode coordinates and momenta that correspond to an initial vibrational quantum state υ_k. For polyatomic reactions, the classical trajectories are most conveniently integrated using space-fixed Cartesian coordinates. There is a canonical transformation that relates the normal mode coordinates Q_k and momenta P_k to the Cartesian coordinates $\left(q_{ix}, q_{iy}, q_{iz} \right)$ and momenta $\left(p_{ix}, p_{iy}, p_{iz} \right)$.[42]

Since our studies of atom + polyatom reactions emphasize dynamical behaviors in the ground state, I briefly describe our special implementation here. The polyatomic reactant molecule is prepared in its ground electronic and rovibrational states by running an intramolecular trajectory (called the "root" trajectory) from its equilibrium geometry with kinetic energy corresponding to the ZPE in each normal mode. The root trajectory is integrated to cover many vibrational periods, and the vibrational phase is sampled uniformly over this time interval. For each selected molecular configuration (represented by Cartesian coordinates and momenta of the atoms), the attacking hydrogen/oxygen is placed around the vibrating molecule with a fixed initial center-of-mass separation and a randomly sampled impact parameter. The intermolecular collision is then started at whatever reagent relative translational energies that are of interest.

However, due to anharmonic and mode coupling terms in the actual molecular Hamiltonian, the harmonic action will vary with time. As long as the molecular motion is still in the quasiperiodic regime, two methods can be used for determining the "good" vibrational actions in QCT calculations. These are the Fourier transform method[50] and the adiabatic switching method.[51] We will not go into details of the procedures as well as the techniques involved in sampling the reagent rotational states, which, although interesting in many applications, is out of the scope of the current study. At higher excitation where the molecular internal motion is chaotic, it is difficult and even impossible to find good classical action variables that correspond to definite quantum states.

2.2.2 Trajectory Propagation

Molecular collisions typically begin and finish at separations large enough so that there is no direct interaction between the reactant or product molecules. Once the initial configuration of the colliding partners is set up, the motion of the system over the PES is simulated by integrating numerically the Hamilton's equations of motion from the reactants to the products[52]

$$
\begin{aligned}
\frac{p_{i\alpha}}{m_i} &= \frac{dq_{i\alpha}}{dt} \\
\frac{\partial V}{\partial q_{i\alpha}} &= -\frac{dp_{i\alpha}}{dt}
\end{aligned}
\qquad i = 1, 2 \cdots N \quad \alpha = x, y, z
\qquad (2\text{-}20)
$$

Here m_i is the mass of the i th atom and V is the potential energy function.

Equation (2-20) thus constitutes a set of $6N$ coupled first-order differential equations that can be integrated using a variety of numerical methods.[53] Generally, they can be classified as either single-step or multi-step method. We have employed the standard fifth-order predictor, sixth-order corrector integration algorithm throughout our calculations.[54] For the dynamical results to have statistical significance, it is necessary to run a large number of trajectories, especially when the interesting dynamics occurs not so frequently. In applications where the PES is available as an analytical expression, it is not very difficult to run, say 10,000 trajectories at a time. In direct dynamics, however, the potential energy and its derivative are computed at each point of the trajectory. It is thus computationally demanding to calculate even several hundred of trajectories at the DFT level. The situation is even worse when long-lived intermediate complexes are involved in the reaction mechanism.

2.2.3 Product Analysis

By periodically examining the interatomic distances during the course of the integration, a trajectory is deemed finished whenever the separation of one particular group of atoms from the other (or others) is larger than a critical value. From the final coordinates and momenta, product channels are assigned and properties of the products are calculated.

2.2.3.1 Relative Translation

To calculate the relative translational energy between products A and B, we first define the relative velocity

$$\mathbf{V}'_{rel} = \mathbf{V}_A - \mathbf{V}_B \qquad (2\text{-}21)$$

Here $\mathbf{V}_A$ and $\mathbf{V}_B$ are the center-of-mass velocities of the respective products. If μ is the reduced mass of the product pair, then

$$E'_{trans} = \frac{1}{2}\mu\left|\mathbf{V}'_{rel}\right|^2 \qquad (2\text{-}22)$$

2.2.3.2 Reaction Cross Section

By definition, the reaction cross section has the following expression

$$\sigma_r = \int_0^\infty 2\pi b P(b)\,db \qquad (2\text{-}23)$$

where $P(b)$ is the probability of reaction at impact parameter b and is known as the opacity function. The "volume element" $2\pi b\,db$ defines the collisional target area between b and $b+db$. In quantum mechanics, the reaction probability is usually

defined in terms of the angular momentum quantum number l. So the reaction cross section is given by the sum

$$\sigma_r = \frac{\pi}{p^2} \sum_{l=0}^{l_{max}} (2l+1)P(l) \tag{2-24}$$

where $P(l)$ is the reaction probability for a given l, and $p = \sqrt{2\mu E_{trans}}$ is the momentum of the reactant system. Note that $bp \approx \left(l+\frac{1}{2}\right)\hbar$ is the semiclassical orbital angular momentum.

2.2.3.3 Scattering Angle

In the center of mass system, the scattering of the product relative to the reactant is defined as

$$\theta = \cos^{-1}\left(\frac{\mathbf{V}_{rel} \cdot \mathbf{V}'_{rel}}{|\mathbf{V}_{rel}||\mathbf{V}'_{rel}|}\right) \tag{2-25}$$

where $\mathbf{V}_{rel}$ and $\mathbf{V}'_{rel}$ are the reactant and product relative velocities, respectively, and θ ranges from 0 to π. To obtain the product angular distribution, we calculate the differential cross section (DCS) in the range θ to $\theta + d\theta$ as

$$\int_0^{2\pi} \int_\theta^{\theta+d\theta} \frac{d\sigma_r}{d\omega} \sin\theta d\theta d\phi = 2\pi \int_\theta^{\theta+d\theta} \frac{d\sigma_r}{d\omega} \sin\theta d\theta \tag{2-26}$$

Here $\sin\theta d\theta d\phi$ defines the solid angle into which the product is scattered. Because the product flux in the center-of-mass frame is azimuthally symmetric, the integration over ϕ can be separated out as 2π. Finally the normalized DCS as reported from our

trajectory calculations are given by $\dfrac{2\pi}{\sigma_r}\displaystyle\int_{\theta}^{\theta+d\theta}\dfrac{d\sigma_r}{d\omega}\sin\theta d\theta$, where σ_r is the integral

cross section.

2.2.3.4 Internal Motion

Because of the complexity associated with polyatomic molecule internal motion (many modes, and vibrational-rotational mode couplings etc), we didn't try to separate vibration and rotation for our polyatomic products. Instead, we calculated the internal energy of polyatomic molecule C as a whole by using

$$E_{\text{int}}'(C) = E_{kin}'(C) + V_{pot}'(C) \qquad (2\text{-}27)$$

Here $E_{kin}'(C)$ and $V_{pot}'(C)$ are the kinetic and potential energies calculated at the end point of the trajectory that produces C. Specifically, $E_{kin}'(C)$ is given by

$$E_{kin}'(C) = \sum_i \frac{1}{2}m_i \left| \mathbf{v}_i' - \mathbf{v}_{com}' \right|^2 \qquad (2\text{-}28)$$

where the sum is over the atoms that comprise molecule C, and $\mathbf{v}_i' - \mathbf{v}_{com}'$ is the velocity of atom i relative to the center-of-mass of C. The potential energy $V_{pot}'(C)$ is with respect to the minimum of the molecular potential well. Then the total available energy for channel C + D is

$$E_{tot}' = E_{trans}' + E_{\text{int}}'(C) + E_{\text{int}}'(D) \qquad (2\text{-}29)$$

For diatomic molecules, we are able to determine their vibrational and rotational quantum states by evaluating[56, 57]

$$\upsilon' = -\frac{1}{2} + \frac{2}{\hbar} \int_{r_<}^{r_>} P_r \, dr \qquad\qquad (2\text{-}30)$$

$$j' = -\frac{1}{2} + \frac{1}{2}\sqrt{1 + 4L^2/\hbar^2} \qquad\qquad (2\text{-}31)$$

where P_r is the momentum along the direction of the bond, r is the bond length, $r_<$ and $r_>$ are the inner and outer turning points as the molecule vibrates, and L is the rotational angular momentum. The values given by Eqs. (2-30) and (2-31) are then rounded off to the nearest integers.

Assuming a Morse oscillator model, the internal energy of the diatomic product is calculated as

$$E'_{int} = \omega_e\left(\upsilon + \frac{1}{2}\right) - \omega_e x_e\left(\upsilon + \frac{1}{2}\right)^2 + b_e j(j+1) - c_e\left[j(j+1)\right]^2 - e_e\left(\upsilon + \frac{1}{2}\right)j(j+1)$$

$$(2\text{-}32)$$

where ω_e, $\omega_e x_e$, b_e, c_e and e_e are some diatomic constants that are calculated from the Morse parameters D_e, r_e and α. There is no unequivocal way of dividing the internal energy into vibrational and rotational energies. We simply define E'_{vib} as the energy of the state $(\upsilon', 0)$, then E'_{rot} is given by $E'_{rot} = E'_{int} - E'_{vib}$.

2.3 The Trajectory Surface Hopping Method

If one wants to extend the classical approach to nonadiabatic processes, one has to introduce quantum mechanical models to account for electronic transitions. The simplest description of electronically nonadiabatic processes is given by the Landau-Zener model,[57-59] in which we assume a one-dimensional system with two states U_1 and U_2. The probability of surface transition at the avoided crossing between two potential curves has the form

$$P_{LZ} = 1 - \exp\left(-\frac{2\pi U_{12}^2}{\hbar v |s_1 - s_2|}\right) \qquad (2\text{-}33)$$

where U_{12} is the off-diagonal coupling terms in the electronic Hamiltonian matrix, $v = dr/dt$ is the velocity at the crossing point; s_1 and s_2 are the slopes dU/dr evaluated also at the crossing point.

Such simple models are still of use today in cases when one wants to simplify calculation of transition probabilities which usually requires integrating the electronic Schrödinger equation along thousands of trajectories. Two very different semiclassical methods based on ensembles of independent trajectories are the trajectory surface hopping approach[60-63] and the time-dependent self-consistent field approach, or Ehrenfest method.[64-70] The second part of this thesis emphasizes the use of the TSH approach, so we briefly describe the methodology here.

The semiclassical methods make a distinction between classical nuclear motion and quantal electron motion. The former is described by classical trajectory $\mathbf{R}(t)$, and the latter is described by the time-dependent Schrödinger equation

$$i\hbar \frac{\partial \Phi(\mathbf{r},t)}{\partial t} = \hat{H}_{el}(\mathbf{r},\mathbf{R})\Phi(\mathbf{r},t) \qquad (2\text{-}34)$$

where $\hat{H}_{el}(\mathbf{r},\mathbf{R})$ and $\Phi(\mathbf{r},t)$ are the electronic Hamiltonian and electronic wavefunction, respectively. We now expand $\Phi(\mathbf{r},t)$ in terms of an orthonormal set of electronic basis functions $\phi_j(\mathbf{r};\mathbf{R}(t))$, which may be adiabatic, diabatic wavefunctions, or any arbitrary set of electronic basis functions

$$\Phi(\mathbf{r},t) = \sum_j c_j(t)\phi_j(\mathbf{r};\mathbf{R}) \qquad (2\text{-}35)$$

Substituting Eq. (2-35) into Eq. (2-34), multiplying from the left by ϕ_k and integrating over $\mathbf{r}$ yields:

$$i\hbar \frac{dc_k}{dt} = \sum_{j\neq k} c_j \left(V_{kj} - i\hbar \left\langle \phi_k \left| \frac{\partial \phi_j}{\partial t} \right. \right\rangle \right) \qquad (2\text{-}36)$$

Here V_{kj} is the off-diagonal terms of the electronic Hamiltonian $\left\langle \phi_k \left| \hat{H}_{el} \right| \phi_j \right\rangle$. Using the chain rule, we may write

$$\left\langle \phi_k \left| \frac{\partial \phi_j}{\partial t} \right. \right\rangle = \frac{d\mathbf{R}}{dt}\cdot\left\langle \phi_k \left| \nabla_{\mathbf{R}}\phi_j \right. \right\rangle = \frac{d\mathbf{R}}{dt}\cdot\mathbf{d}_{kj} \qquad (2\text{-}37)$$

So Eq. (2-36) can be rewritten as

$$i\hbar \frac{dc_k}{dt} = \sum_{j\neq k} c_j \left(V_{kj} - i\hbar \frac{d\mathbf{R}}{dt}\cdot\mathbf{d}_{kj} \right) \qquad (2\text{-}38)$$

This expression shows the two terms that may promote transitions between electronic states: the scalar coupling V_{kj} and the vector coupling $\frac{d\mathbf{R}}{dt} \cdot \mathbf{d}_{kj}$. The V_{kj} will vanish when one uses an adiabatic representation.

A surface-hopping trajectory is usually initiated on one of the electronic states, i.e., $c_j(0) = \delta_{ji}$ with i being the chosen initial state. The trajectory is integrated classical mechanically and simultaneously one solves the coupled equations (2-38) to obtain the amplitude $c_j(t)$ for each electronic state. The propagation is interrupted at small time intervals Δt with hopping decisions. In Tully's fewest switch method,[6] hopping decision is made by computing a switching probability $P_{j \leftarrow i}$ from the current state i to all other states j using

$$P_{j \leftarrow i} = \frac{\dot{a}_{jj} \Delta t}{a_{ii}} \qquad (2\text{-}39)$$

where $a_{ij} = c_i c_j^*$ is the electronic density matrix whose diagonal element a_{jj} is the electronic state probability, and off-diagonal a_{ij} is the electronic state decoherence. The $P_{j \leftarrow i}$ is then compared with a random number between 0 and 1 to determine if a surface hop should occur. When a hop is made, the trajectory propagation is reinitiated on the new surface. Furthermore, if at the hopping location $\mathbf{R}$, $V_{jj} \neq V_{ii}$, the momentum component in the direction perpendicular to the intersection seam must be adjusted in order to conserve total energy. If no hop occurs, the trajectory will continue on the

original surface. Whether or not there is a hop, integration of the electronic Schrödinger equation is continued without modification. By running a swarm of trajectories, each switching states at slightly different locations over regions of strong electronic coupling, which may be narrow or broad, the gradual flow of probability density between states is accurately modeled.

There are cases when it is possible to avoid solving Eq. (2-38) by using an approximate expression such as the Landau-Zener formula described above. Whenever the transition probability can be expressed in such a simplified form, the TSH calculation is greatly facilitated. We will employ this strategy in our direct dynamics TSH studies of intersystem crossing effects in the O (^{3}P) + ethylene reaction.

Chapter 3

The H + CD$_4$ Abstraction Reaction

3.1 Introduction

The reaction

$$H + CH_4 \rightarrow CH_3 + H_2 \qquad \Delta H\,(0K) = -0.02 \text{ kcal mol}^{-1}$$

and its isotopic counterparts attract much experimental and theoretical attention for several reasons: (1) the H + CH$_4$ reaction is important in hydrocarbon combustion;[71] (2) it is the simplest reaction occurring at an sp^3 hybridized carbon center and thus serves as a benchmark for gas-phase polyatomic reaction studies; (3) this reaction is isoelectronic with F + H$_2$ and H + H$_2$O, and is amenable to high level *ab initio* calculations.

There are many experimental studies of both the forward and reverse reactions that have addressed the kinetics.[72-77] The forward reaction was found to have an

appreciable activation energy of ~12 kcal mol^{-1}, and the rate constants at room temperature are very small, ~2—7×10^{-19} cm^{3}molecule^{-1}s^{-1}.[72-74] In 2001, Sutherland *et al.*[76] used the laser photolysis-shock tube technique to measure the forward and reverse reactions. By combining their own data with previous kinetic data, they recommended an empirical expression for the forward rate constant

$$k(T) = 6.78 \times 10^{-21} T^{3.156} e^{-4406 K/T} cm^3 molecule^{-1} s^{-1} \qquad (3\text{-}1)$$

over the temperature range 348—1950 K. Experimental study of the state-to-state dynamics is difficult due to the very small reaction cross section, 0.14 ± 0.03 Å^2 at 1.5 eV reagent collision energy.[78] Before this work, there have been only two[78, 79] experimental dynamics studies.

In the earlier CARS experiment (coherent anti-Stokes Raman spectroscopy), Valentini and coworkers[78] measured the rovibartional state distributions of the HD product from the H + CD$_4$ abstraction reaction at 1.5 eV. The total cross section is only 0.14 ± 0.03 Å^2. More than 95% of the HD product are formed in the $\upsilon' = 0$ and 1 vibrational states; very little of the reagent translational energy is channeled into the HD internal motion, 7% to HD vibration and 9% to HD rotation. Besides, they found an anomalous correlation between the HD vibrational and rotational excitation: HD in the $\upsilon' = 1$ state has on average more rotational energy than does HD in the $\upsilon' = 0$ state.

The more recent *photoloc* experiment (photoinitiated reaction analyzed by the law-of-cosines) by Camden *et al.*[79] studied the nascent CD$_3$ product from H + CD$_4$. At a collision energy of ~1.95 eV, it was found that CD$_3$ is produced in the ground vibrational

state or is one-quantum excited in the umbrella-bending mode. Furthermore, the CD_3 products are mainly scattered in the sideways/backward directions with respect to the incident H atoms. This stands in stark contrast to the predictions of previous trajectory calculations,[80-82] which suggest a rebound reaction mechanism. The authors thus speculated that a stripping mechanism at large impact parameter dominates the reaction mechanism, and the abstraction and exchange channels may compete at small parameters.

The only experimental study of the exchange reaction $H + CD_4 \rightarrow CHD_3 + H$ was performed by Bersohn and coworkers.[83] The reaction cross section was determined to be 0.084 ± 0.014 Å^2 at a collision energy of ~2 eV. They concluded that the exchange reaction takes place via an S_N2 inversion mechanism, and nearly elastic behavior was found during the reaction, with the D atom taking away $86 \pm 7\%$ of the incident kinetic energy.

Much of the theoretical work[80-82, 84-115] on this reaction has been concerned with determination of the stationary point properties, construction of the potential energy surface, and calculation of the thermally averaged rate constants, although occasionally there has been work on the state-resolved dynamics.

Previous high level *ab initio* calculations[84-88] show that the abstraction reaction proceeds through a C_{3v} symmetric transition state. The breaking C-H distance in the TS structure is close to 1.4 Å (the normal C-H single bond length is ~1.09 Å), while the forming H-H bond is slightly stretched (0.89 Å) as compared to the normal H-H bond length 0.74 Å. This structure thus indicates a late transition state (more product-like). For

the exchange reaction, the TS structure belongs to the D_{3h} point group, with the breaking and forming C-H bonds being 1.33 Å. The classical barriers to reaction are around 15 kcal mol^{-1} and 40 kcal mol^{-1} for abstraction and exchange, respectively.

There have been many PESs developed for the H + CH$_4$ reactive system. The first[80] of these simply treated H'–CH$_3$ as a pseudodiatom and obtained an extended London-Eyring-Polanyi-Sato (LEPS) surface for classical trajectory calculations. Then in the early and middle 1970s, full-dimensional surfaces were constructed separately by Bunker and coworkers[82, 89-91] and by Raff.[81] The former is purely an empirical function fit to experiment, while the latter is based on semiempirical INDO results and *ab initio* SCF and CI calculations. These surfaces were later concluded[92] not realistic enough for quantitative dynamical studies, and a new surface was introduced[93] which was derived from the Raff surface but calibrated against kinetic data and previous *ab initio* calculations.[84-86, 116] This surface is not symmetric with respect to the four methane hydrogens and is not suitable for trajectory calculations.[94]

In 1995, Jordan and Gilbert[84] reported a four-fold symmetric PES using the functional forms of the Joseph *et al*. surface (hereafter called the JG surface). This surface was subsequently used by many groups[96-107] to carry out theoretical kinetic and dynamic calculations. These include several quantum reduced dimensionality dynamics calculations by Takayanagi *et al*.[96] (3D), by Yu and Nyman[97] (4D, rotating bond umbrella approximation), by Zhang, Zhang and coworkers[99] (4D, semirigid vibrating rotor target model), and by Bowman and coworkers[100] (6D), as well as full dimensional calculations

by Huarte-Larrañaga and Manthe[103-106] and TST calculations with multidimensional tunneling corrections.[107] The thermal rate constants from the above calculations are generally significantly larger than the experiment, suggesting that the reaction barrier on the JG surface is too low.

It was further pointed out by Espinosa-García *et al.*[109] that the JG surface is not fully invariant to the permutation of the methane hydrogens. In 2002, Espinosa-García[110] recalibrated the JG surface with updated experimental and *ab initio* data and published a new surface (referred to hereafter as the EG surface) which corrects the symmetry problem of the JG surface. A later path integral calculation[114] under the quantum instanton approximation calculated rate constants on the EG surface. The results were in good agreement with experimental measurements. A more recent surface by Manthe and coworkers[115] employed Shepard interpolation[117, 118] of high level *ab initio* calculations centered around the transition state region and yielded rate constants of comparable accuracy to the available experiments. However, this surface is not globally defined and thus cannot be used to describe state resolved dynamics.

In this work, we present a combined experimental and theoretical study of the dynamics of ground state $H + CD_4$ ($\upsilon = 0$) $\rightarrow HD + CD_3$ reaction. The experiments were performed by the Zare lab of Stanford University. Using the well-established *photoloc* technique,[119] they were able to realize laser preparation of the reagent quantum states and state specific detection of the reaction products. Dynamical information such as the excitation function, product speed and angular distributions, and product state

distributions can then be extracted through appropriate measurements of the concerned quantities. Detailed description of the experimental setup can be found in our papers.[120] The theory is based on quasiclassical trajectories that we have integrated using several PESs: the analytical EG surface,[110] semiempirical surfaces derived from the MSINDO semiempirical method,[121] and a DFT surface based on the B3LYP functional.[122] Except for the EG surface, all our calculations emphasize the use of direct dynamics where energy and forces are generated on the fly. With these calculations, we showed that the H + CD_4 reaction exhibits extreme sensitivity to quite modest differences in the PESs. It is clear through our comparison of experiment and theory that, of the surfaces examined, B3LYP provides the best description of the overall dynamics.

3.2 Theoretical Methods

The three electronic structure models that are used to construct the PESs include (1) B3LYP/6-31G (d, p), for which we have used the Q-Chem[123] computer program, (2) the MSINDO semiempirical Hamiltonian, and (3) a reparametrized MSINDO model (hereafter referred to as "reparametrized MSINDO"), in which the values of the C and H empirical parameters in MSINDO have been adjusted for this specific reaction system. In addition, the previously developed analytical surface EG[110] is considered. The self-consistent field (SCF) unrestricted Hartree-Fock (UHF) technique is employed in all direct dynamics and electronic structure calculations.

The DFT approach provides the highest level of theory used in our direct dynamics calculations. The CPU time for calculating energy gradients at each integration step, however, limits the total number of DFT trajectories that can be run. A less rigorous but computationally fast approach is to use semiempirical molecular orbital (MO) methods. Semiempirical methods are quantum mechanical in nature, but use experimentally derived parameters to compensate for errors introduced by neglect of many of the difficult integrals. Although semiempirical methods are able to describe the general shape of the PES, quantitatively accurate results for a given system may require specific adjustment of the values of the parameters. In the present work, we have used MSINDO, which is a similar method to the well-known AM1[124] and PM3[125] methods, but with somewhat more accurate saddle point properties in the present application. The effect of reparametrization of the MSINDO Hamiltonian is also examined.

The reagent collision energies explored in our calculations range from 0.5 eV to 3.0 eV. For the EG and MSINDO dynamical calculations, batches of 10,000 trajectories are run per collision energy. For B3LYP, we have run 10,000 trajectories at 0.75, 1.2, 1.5 and 1.95 eV, respectively, and 1,000 at the other collision energies due to the tremendous computational expense involved when using this method. A standard fifth-order predictor, sixth-order corrector integration algorithm[54] is employed to propagate the equations of motion along the trajectory. The integration step for the analytical PESs and B3LYP is 10.0 au (0.24 fs), and that for the MSINDO calculations is 5.0 au.

When generating initial conditions for the polyatomic reactant, we follow the normal mode sampling procedure as described in Section 2.2.1. Note that this procedure for generating initial conditions forces every trajectory to have the same CD_4 internal energy, however there is no guarantee that the action in each vibrational mode has the correct value for the chosen initial state. This issue was studied for $H + CH_4$ by Huang *et al.*[95] using the adiabatic switching approach to define the initial conditions, and they found that a small number of trajectories could in fact have important deviations from the correct behavior. In the present application it is not possible to use a better method such as adiabatic switching to define initial conditions, so we instead use the calculated reactive threshold energies to determine the significance of the ZPE problem in our results.

At the completion of the trajectory calculation, a final analysis is performed to derive various dynamical properties of the products. In particular, we calculate the total angular momentum $<L^2>$ for the CD_3 radical, from which we define the CD_3 rotational quantum number N by using $<L^2> = N(N+1)\hbar^2$. To determine the decomposition of the CD_3 rotational angular momentum relative to body-fixed directions, we propagate the CD_3 coordinates and momenta for additional 500 (EG, B3LYP) or 1,000 (reparametrized MSINDO) steps. At each step we project the CD_3 angular momentum vector onto the instantaneous principal axes, calculate the rotational energy about each axis, and average the results over this period. In calculating product vibrational energies, we did not discard trajectories violating the ZPE constraint, but we did subtract the ZPEs from the

vibrational energies of the products. Because we use classical mechanics, the products may have smaller energy than the ZPE (ZPE violation). In such cases, we "round up" the energies of the fragments to the ZPE values.

3.3 Results and Discussions

3.3.1 Properties of the Potential Energy Surfaces

Table 3-1 compares properties of the potential surfaces used in the dynamics calculations. Also presented are results from AM1, PM3 (for which we use GAMESS[126]), the earlier JG surface, as well as high level *ab initio* calculations (the internal coordinates are defined in Figure 3-1). [87, 88]

Figure 3-1.   Definition of internal coordinates at the abstraction saddle point.
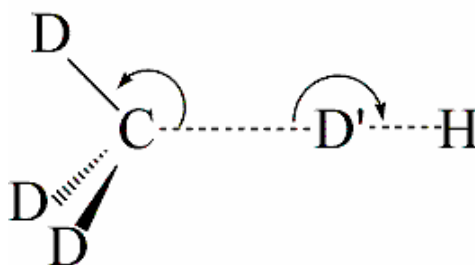
Despite the greatly overestimated reaction barrier, MSINDO predicts a TS geometry and reaction energy noticeably closer to *ab initio* results than does AM1 or PM3.

Reparametrization of MSINDO has been performed by fitting the QCISD(T)/ 6-311G(2d,2p) //UMP2/cc-pVTZ data for stationary points. The new set of parameters is listed in Table 3-2. We see that the reparametrized MSINDO surface improves on the original one in terms of the TS geometry, classical barrier height and reaction endoergicity. Compared to high level *ab initio* results, the classical barrier heights are underestimated by a few kcal mol^{-1} on the JG, EG and B3LYP PESs. [After extrapolation to the basis set and correlation energy limits,[110] a classical barrier height of 13.3 kcal mol^{-1} was obtained for the abstraction reaction, as compared to the 15.3 kcal mol^{-1} by CCSD(T)/cc-pVQZ calculations.[87] Actually the EG surface was fitted to the extrapolated barrier height.] We also note that the B3LYP/6-31G** TS geometry agrees better with the ab initio results, having a longer C-H' (H' is the abstracted hydrogen atom) breaking bond, hence corresponding to a later TS than those on the other surfaces. Based on Polanyi's rule[16] it is expected that, at a given total energy, for PESs with late TSs, CD$_4$ stretch excitation promotes reactivity more than if the energy is placed in reagent translational motion. Indeed, recent experiments indicate that the C-H stretch excitation enhances the analogous H + CH$_4$ ($\upsilon_3 = 1$, antisymmetric stretching) reaction cross section by a factor of 3.0 ± 1.5.[127]

theory levels

SP	Parameters	KGC	DD	QCISD(T)	B3LYP	EG	JG
CH$_4$	R(C-H)	1.086	1.084	1.082	1.092	1.094	1.094
	ZPE		28.6	27.8	28.3	27.3	27.2
CH$_3$	R(C-H)	1.076	1.074	1.071	1.082	1.094	1.094
	ZPE		19.0	19.1	18.5	18.2	24.5
H$_2$	R(H-H)		0.737	0.737	0.743	0.742	0.742
	ZPE		6.5	6.5	6.4	6.3	6.3
TS	R(C-H)	1.082	1.080	1.077	1.087	1.094	1.094
	R(C-H')	1.393	1.405	1.409	1.412	1.331[g]	1.327
	R(H'-H")	0.897	0.872	0.869	0.894	0.931[g]	0.916
	<HCH'	103.7	103.0	102.7	103.4	107.4	107.4
	<CH'H"	180	180	180	180	180	180
	Normal mode frequency	3229		3297	3244	3097	3094
		3229		3297	3243	3097	3094
		3083		3148	3096	2962	2960
		1763		1992	1882	1533	1601
		1458		1468	1445	1439	1438
		1458		1468	1441	1439	1438
		1124		1144	1164	1264	1244
		1124		1144	1163	1264	1244
		1093		1073	1082	1219	1204
		518		554	552	604	587
		518		554	533	604	587
		1500i	1662i	1609i	1119i	1293i	1092i
	ZPE	26.6	27.2	27.4	26.9	26.5	27.3
	ΔE$_{barr}$	15.3	15.1 (13.7)	15.6 (15.2)	9.4 (8.0)	12.9 (12.1)	10.9 (10.9)
	ΔE$_{react}$	2.7	2.8 (-0.3)	3.4 (1.1)	2.5 (-0.6)	2.8 (-0.01)	2.8

Table 3-1.   Continued

SP	Parameters	AM1	PM3	MSINDO[h]	rep MSINDO[h]	Expt[f]
CH$_4$	R(C-H)	1.112	1.087	1.076	1.063	1.091
	ZPE	27.9	28.5	28.7	30.1	
CH$_3$	R(C-H)	1.086	1.072	1.065	1.069	1.079
	ZPE	18.9	18.4	18.6	20.2	
H$_2$	R(H-H)	0.677	0.699	0.746	0.738	0.741
	ZPE	6.2	6.4	5.9	6.3	
TS	R(C-H)	1.110	1.086	1.077	1.078	
	R(C-H')	1.130	1.101	1.272	1.327	
	R(H'-H")	1.285	1.412	0.932	0.834	
	<HCH'	varies	varies	107.1	106.0	
	<CH'H"	162	139	180	180	
	Normal mode frequency	3193	3283	3271	3577	
		3112	3209	3267	3577	
		3110	3196	3082	3208	
		2772	2988	1424	2498	
		1398	1435	1424	1401	
		1397	1429	1411	1400	
		1372	1354	1367	1335	
		1351	1341	1120	1071	
		1345	1321	1115	1043	
		146	233	407	530	
		91	136	407	515	
		567i	618i	2261i	720i	
	ZPE	27.6	28.5	26.2	28.8	
	ΔE_{barr}	-0.2	-6.2	28.6 (26.1)	15.4 (14.1)	11.49
	ΔE_{react}	-18.5	-24.5	-1.1 (-5.3)	2.8 (-0.8)	0.59 [-0.02]

a. Bond lengths are in angstrom, angles in degree, energies in kcal mol^{-1}, and frequencies in cm^{-1}.
b. Values in parentheses are zero-point corrected energies.
c. Reference 87. Geometries and energies are at CCSD(T)/cc-pVQZ level.
d. Reference 88. Energies were calculated using QCISD(T)/CC at the geometries determined at the MP2(FU)/TZ+2P+f level. See the reference for details of the basis sets used.
e. Geometries were calculated using UMP2/cc-pVTZ and energies are at QCISD(T)/6-311G(2d,2p) level.

f. Structural data and the experimental enthalpy of reaction at 0 K in brackets are from JANAF Thermochemical Tables, 3rd ed. edited by Chase, Jr., M.W.; Davies, C.A.; Downey, J.R.; Frurip, D.J.; McDonald, R.A.; Syverud, A.N. National Bureau of Standards, Washington, D.C., 1985, Vol. 14; Activation energy and reaction enthalpy are at 300 K and from Evaluated Kinetic Data on Gas Phase Hydrogen Transfer Reactions of Methyl Radicals. Kerr, J.A.; Parsonage, M.J. Butterworths, London, 1976.
g. The values for R(C-H') and R(H'-H") reported in Ref. 110 mistyped. We thank Prof. J. Espinosa-Garcia for confirming that our values are correct.
h. We report the vibrational frequencies as obtained using the MSINDO program. Note that the frequencies in MSINDO are scaled so that they are significantly smaller than what would correspond to the actual curvature of the potential surface.

Table 3-2. Adjusted values of empirical parameters in MSINDO

		ζ_s^U	ζ_p^U	ζ_s	ζ_p	$-I_s$	$-I_p$	ε_{1s}	τ_{1s}	K_σ	K_π	κ_1	κ_2
Original value	H	1.0060		1.1576		0.5				0.1449		0.3856	0.5038
	C	1.6266	1.5572	1.7874	1.6770	0.8195	0.3824	10.430	5.0830	0.0867	0.0478	0.4936	
Adjusted value	H	0.9683		1.1559		0.6383				0.2151		0.3829	0.4827
	C	2.0258	1.4350	2.0487	1.6900	0.8849	0.4386	12.688	4.6641	0.0752	0.0445	0.5598	

An important property of the direct dynamics calculations is that they contain information about the $H + CD_4 \rightarrow HCD_3 + D$ exchange channel that would be extremely difficult to include in an analytical PES. Accordingly, we observe some trajectories resulting in H/D exchange. The number of exchange trajectories increases with collision energy, but the cross section is too small to provide statistically meaningful results.

3.3.2 Excitation Function

The current experimental technique cannot measure absolute reaction cross sections, but it is possible to determine relative excitation functions.[128] In Figure 3-2, we compare the experimental relative excitation function to theoretical calculations. We have normalized the data such that the cross sections at 1.5 eV are the same value. It is clear

that MSINDO does not capture observed trend while B3LYP, EG and reparametrized

MSINDO are in better agreement with experiment.

Figure 3-2.　Comparison of the experimental and theoretical relative excitation functions for the H + CD$_4$(v=0) → HD + CD$_3$ reaction over the collision energy range 1.48 − 2.36 eV. The cross sections are normalized to 1 at E_{col} = 1.5 eV. The experimental uncertainty is the 95% confidence interval derived from replicate measurements.
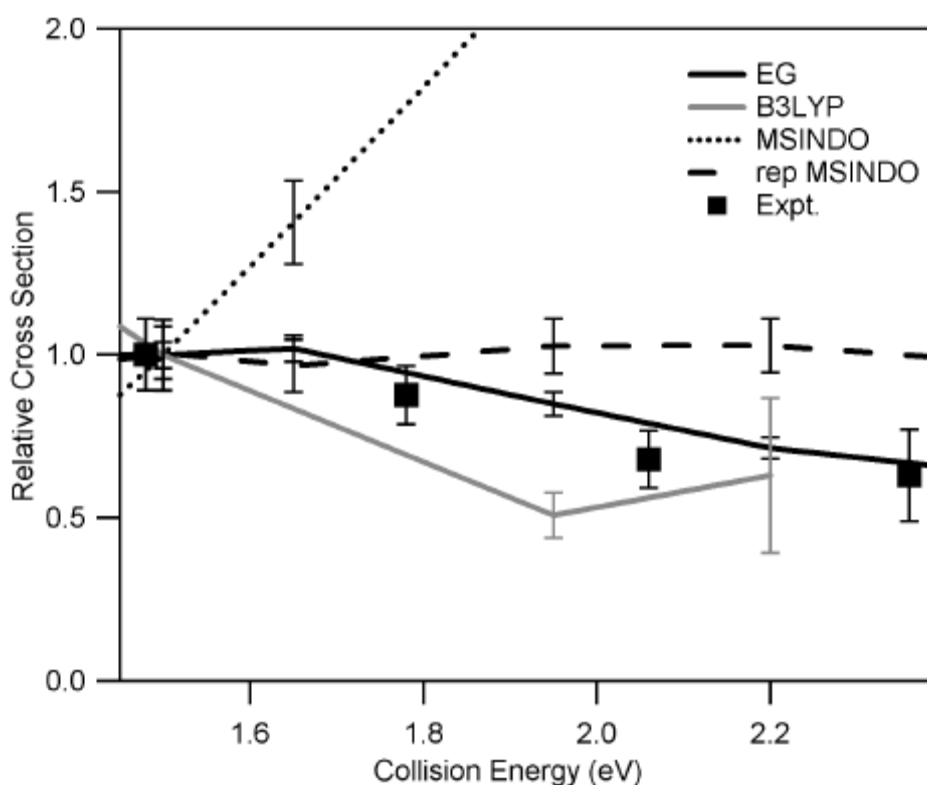
Combining the relative excitation function obtained in our experiments with the

absolute measurement of Germann et al.[78] at 1.5 eV, we derive the absolute cross section

over the 1.48—2.36 eV energy range, which is compared to the theory in Figure 3-3.Over

the considered energy range, the calculated cross sections increase from their respective

thresholds to a maximum, then either gradually decrease (the EG and B3LYP curves), or

become nearly constant (the MSINDO and reparametrized MSINDO curves) at higher

energies.

Figure 3-3.   Comparison of the experimental and theoretical excitation functions
(integral cross section vs. collision energy) for the $H + CD_4$ ($\upsilon=0$) $\rightarrow$ $HD + CD_3$ reaction.
The current experimental points are scaled to the absolute cross section measurement of
Valentini and co-workers[78] obtained at 1.5 eV.
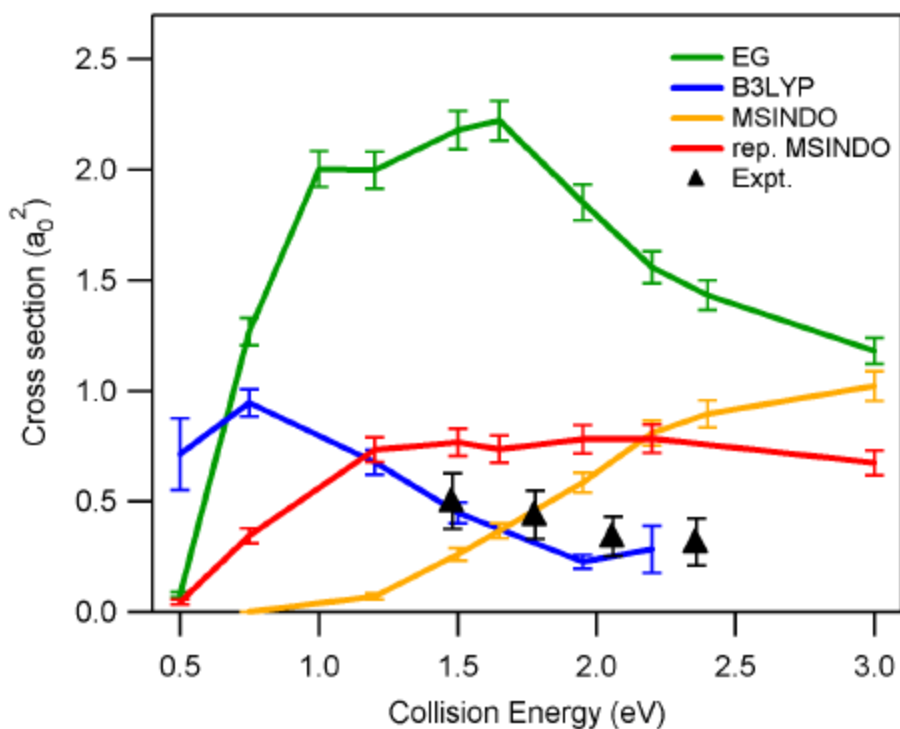
The threshold energies for EG and reparametrized MSINDO are both just under

0.50 eV, which is only a little below the harmonic zero point corrected barriers (0.52 and

0.61 eV, respectively). This provides an indication that ZPE violation must be small in

our simulations, which is similar behavior to what has been noted for the analogous H + H_2O reaction[129] where a more careful specification of the initial conditions can be done. It is not practical to determine the effective threshold on the B3LYP surface, but inspection of Figure 3-3 suggests that it is probably somewhat below the zero-point corrected barrier (0.35 eV), again indicating some, but not serious, ZPE violation.

Overall the best agreement between experiment and theory occurs for the B3LYP results. In particular, the cross section obtained by Valentini and coworkers[78] at 1.5 eV is 0.50 ± 0.11 a_0^2, whereas B3LYP gives 0.45 ± 0.05 a_0^2. The EG curve increases abruptly with increasing collision energy before 1.0 eV, and reaches a peak at ~1.65 eV (~2.22 a_0^2), whereas on the B3LYP and reparametrized MSINDO surfaces the reactivity increases more slowly. The maximum on the B3LYP occurs earlier, and at higher energies the cross section remains well below that on the EG surface. The larger reactivity on the EG surface (except at very low energies) is in agreement with the nature of its TS, which is less product-like than are the B3LYP and reparametrized MSINDO TSs, and therefore more easily accessed. However, at energies close to threshold, e.g.; 0.5 eV, the sequence of reactivity is B3LYP > EG $\approx$ reparametrized MSINDO, which reflects the reversed sequence of barrier heights on the three surfaces. ZPE violation could contribute to this result, but an additional feature favoring reaction on the B3LYP surface at low collision energies is its wide cone of acceptance around the C-D' bond in the TS region (D' is the abstracted deuterium atom). Low-energy collisions are expected to be strongly dependent on the features of the PESs, thus providing a test of the accuracy of

the surfaces. An examination of the H-D'-C bending-energy curves at the abstraction saddle point (shown in Figure 3-4) reveals that the EG curve increases the fastest with the bending angle (highest anisotropy), while the reparametrized MSINDO curve has the lowest anisotropy. The B3LYP curve, which is in good agreement with QCISD(T)/6-311G(2d,2p) calculations, is intermediate between them. The lower anisotropy of a surface in the area near the TS indicates a more flexible transition structure, or a wider cone of acceptance, allowing the H-D'-C angle further from the collinear minimum energy path, thus translating into larger reaction cross sections and higher rotational excitation for the HD product. To estimate the accuracy of our calculations, we note that the B3LYP barrier is lower that that from higher level calculations, e. g. the QCISD(T)/cc-pVTZ barrier. The latter barrier is expected to be within 0.1 eV of reality; thus, B3LYP probably underestimates the threshold to reaction, and in turn overestimates reactivity at low collision energies.

Figure 3-4. The H-D'-C bending-energy curves at the abstraction saddle point. (a) H-D'-C-D dihedral angle = 0 degree and (b) H-D'-C-D dihedral angle = 180 degrees. The curves depict the dependence of the energy on the H-D'-C angle while the remaining coordinates are fixed at their TS values for the different methods.
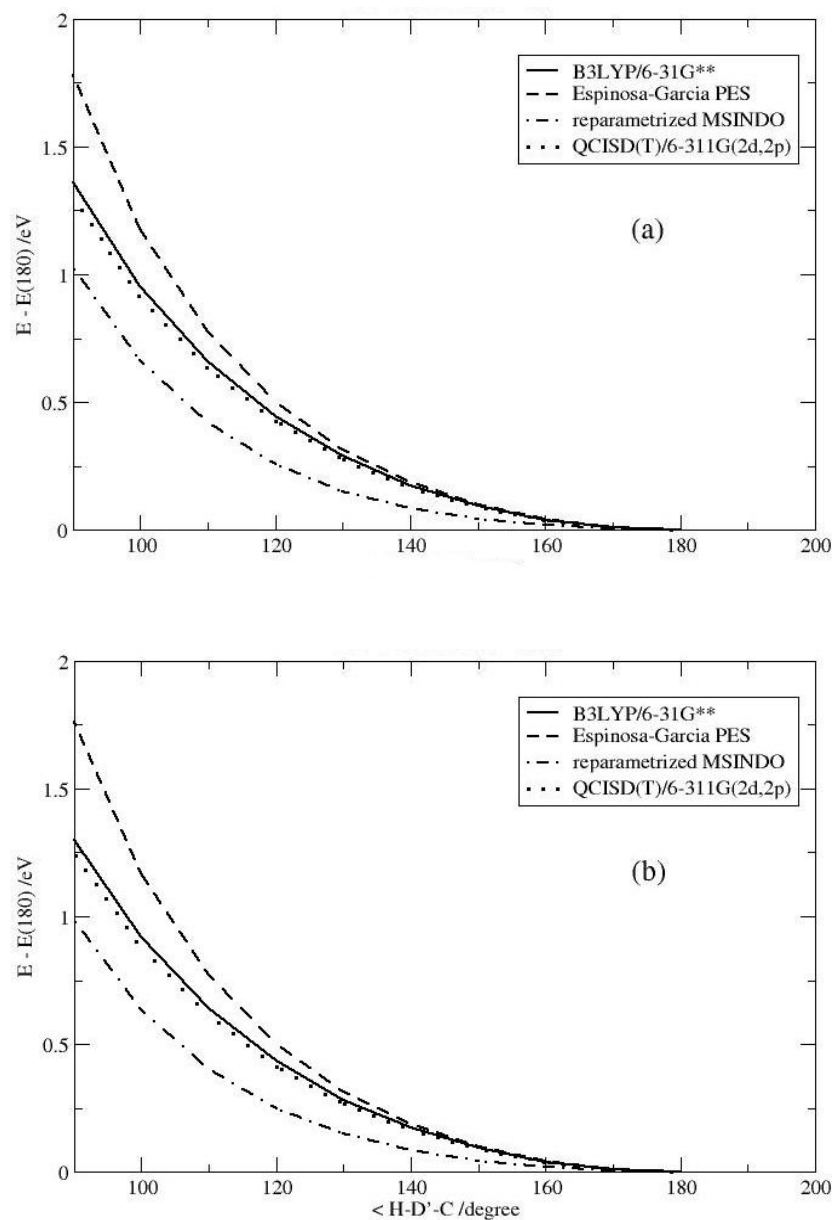
3.3.3 Lab-Frame Speed Distributions

Figure 3-5.   Experimental and theoretical CD$_3$ lab-speed distributions for H + CD$_4$ (υ=0) → HD + CD$_3$ at (a) 1.2 eV and (b) 1.95 eV. The lab-speed distribution is related to the center-of-mass scattering angle as illustrated in Figure 3-18.
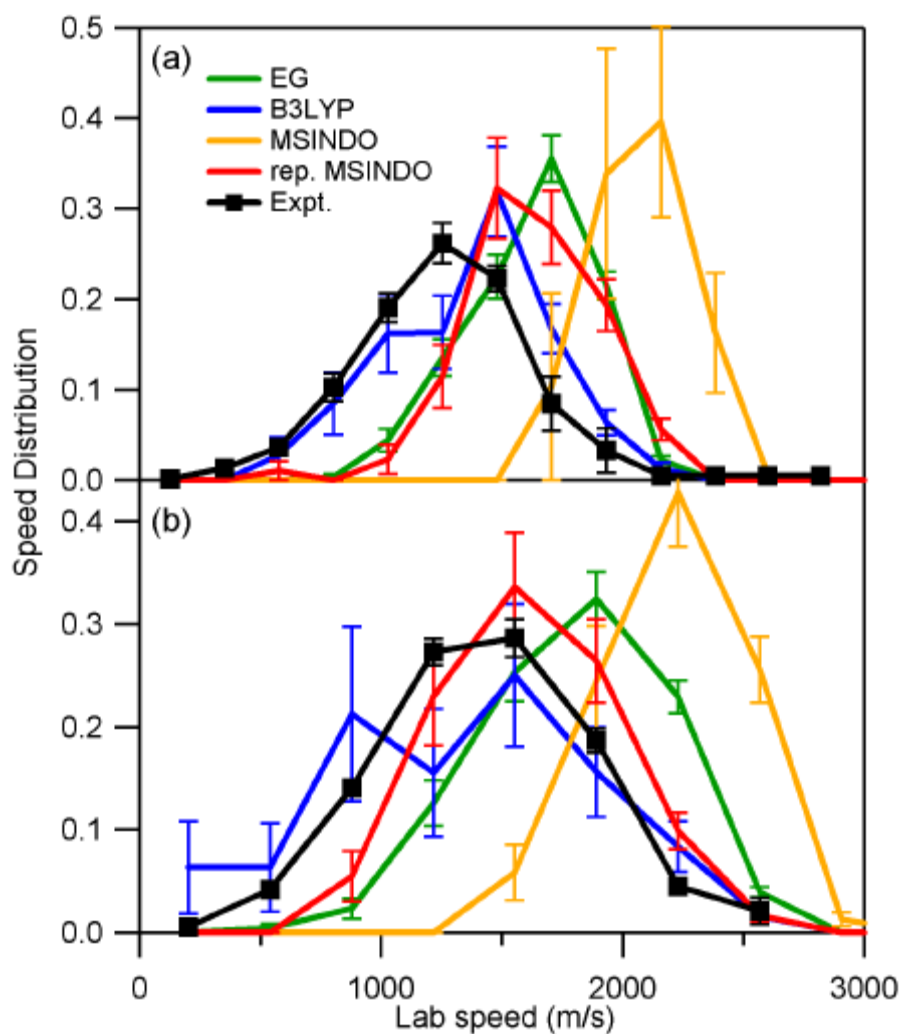
The most rigorous comparison between experiment and theory can be made by using the trajectory data to calculate purely theoretical speed distributions and compare them to the experimental distribution. This approach accounts for both the scattering angle and internal energy of the HD co-product coincident with the observed CD_3. In Figure 3-5 we make such a comparison for the CD_3 lab-speed distributions at 1.2 and 1.95 eV collision energies. The 1.95 eV experiment has a small contribution that originates from the H atoms that coincide with spin-orbit excited Br atoms (quantum yield = 0.15); therefore, the theoretical distributions shown in Figure 3-5b are the weighted sum (according to the Br/Br* quantum yield and the calculated reaction cross sections) of the calculated speed distributions of the slow channel (1.5 eV collision energy) and the fast channel (1.95 eV). The MSINDO distributions compare poorly with the experiment, but after reparametrization we find a qualitative improvement (the reparametrized curves), especially at 1.95 eV. The calculated distributions, however, for the reparametrized MSINDO surface are still shifted to higher speeds by several hundred m s^{-1}, and the analytical surface is also in poor agreement with the experiment. Therefore, even accounting for the large uncertainties in our calculations on the DFT surface, the B3LYP/6-31G** distributions at both energies are in general agreement with the experiment.

3.3.4 Angular Distributions

The speed distribution that results from a typical *photoloc* experiment can be converted into DCS under favorable conditions.[130] Experimental analysis provides a

general trend of the product angular distribution: at 1.2 eV, the CD_3 products are broadly

sideways scattered and at 1.95 eV they are broadly sideways and backwards scattered.

Figure 3-6. Calculated CD_3 angular distributions for $H + CD_4$ ($\upsilon=0$) $\rightarrow$ HD + CD_3 at (a) 1.2 eV and (b) 1.95 eV expressed in terms of normalized differential cross sections [$(2\pi/\sigma)(d\sigma/d\Omega')$].
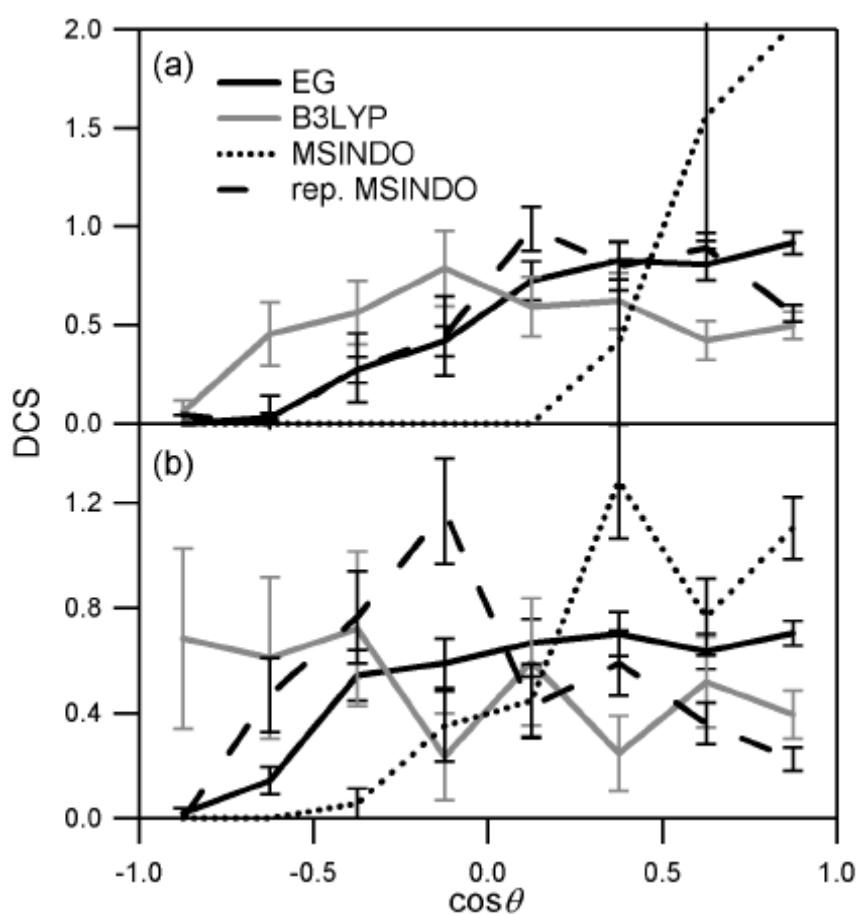
Figure 3-6 compares the calculated product angular distributions for 1.2 and 1.95 eV

collision energies. Table 3-3 summarizes the average values of the cosine of the

scattering angles $<\cos\theta>$ on the surfaces and from experiment. Previous calculated results from refs. 80, 81, and 82 are also listed. For both energies the CD_3 flux is predominantly forward scattered with respect to the incident H atoms on the EG and MSINDO surfaces, contradictory to the present experiment. In fact, a markedly forward biased CD_3 angular distribution is found on the EG surface at all collision energies (Figure 3-7a), implying a direct reaction with a high contribution from a rebound mechanism (H atom is directed along the D-C bond and HD rebounds backwards). Table 3-3 shows that the EG results are similar to the very old results from refs. 80 and 81. The statistics on the B3LYP surface are poor, but the distribution is biased in the sideways direction at 1.2 eV, and the angular distribution switches from forward to backward with increasing collision energy (Figure 3-7b), indicating a change in the dominant mechanism. We can observe the same trend in the reparametrized MSINDO distributions, though they are of more forward and sideways characters at low and high energies, respectively (Figure 3-7c).

Table 3-3.　Calculated and experimental average scattering angles $<\cos\theta>$ for methyl radical.

E_{coll} (eV)	Espinosa-García PES	B3LYP/6-31G**	MSINDO	reparametrized MSINDO	Ref. 80 [a]	Ref. 81[a]	Ref. 82	Expt.[b]
1.08						0.26	0.87	
1.2	0.39 ± 0.02	0.09 ± 0.01	0.71 ± 0.14	0.33 ± 0.03				-0.07 ± 0.10
1.73						0.28	0.57	
1.95	0.25 ± 0.01	-0.11 ± 0.01	0.48 ± 0.04	-0.004 ± 0.0003				-0.20 ± 0.09
2.0					0.39			

a. Refers to the hot atom reaction $T + CH_4$.
b. This work.

To gain more insight into the reaction mechanism, we studied the correlation between the impact parameter b and the angular distribution on the representative EG, B3LYP and reparametried MSINDO surfaces (Figure 3-8). Collisions with $b<1.0$ a_0 show forward scattered CD_3 at all collision energies on the three PESs. This result indicates that head-on collisions lead to backward scattered HD (rebound mechanism), as expected. In collisions with $b>2.0$ a_0, preferred scattering changes markedly as the collision energy increases on the three surfaces. At high collision energies the CD_3 product is scattered into the backward hemisphere, while at energies closer to threshold the CD_3 is centered around the sideways direction. The large b angular distributions agree well with the model discussed by Simpson et al.[131] for the Cl + CH_4 reaction: the backward scattered CD_3 is associated with an HD that maintains the original direction of the H atom, and corresponds to a stripping-type mechanism. As the initial relative translational energy decreases, the H atom does not have the momentum to "run away" with the D atom, and the scattering angle decreases. This type of collision also plays a special role in product energy deposition as will be discussed later.

Figure 3-7. The CD_3 angular distributions at different collision energies for the H + CD_4 (υ=0) → HD + CD_3 reaction on (a) the Espinosa-García surface; (b) the B3LYP/6-31G** surface; (c) the reparametrized MSINDO surface.
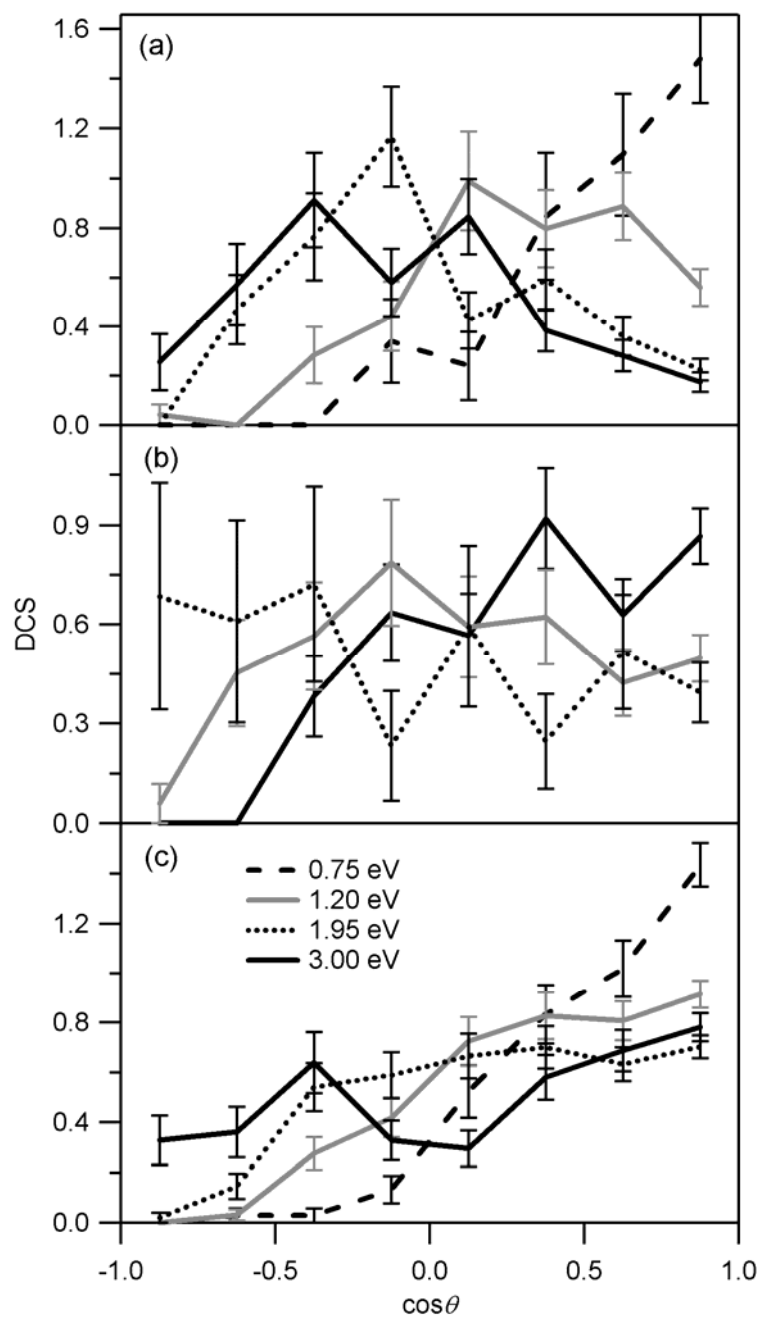
Figure 3-8. Dependence of the CD_3 angular distribution on the impact parameter for the H + CD_4 (υ=0) → HD + CD_3 reaction. Angular distributions are given for (a) the Espinosa-García surface with b<1.0 a_0; (b) the Espinosa-García surface with b>2.0 a_0; (c) the B3LYP/6-31G** surface with b<1.0 a_0; (d) the B3LYP/6-31G** surface with b>2.0 a_0; (e) the reparametrized MSINDO surface with b<1.0 a_0; and (f) the reparametrized MSINDO surface with b>2.0 a_0.
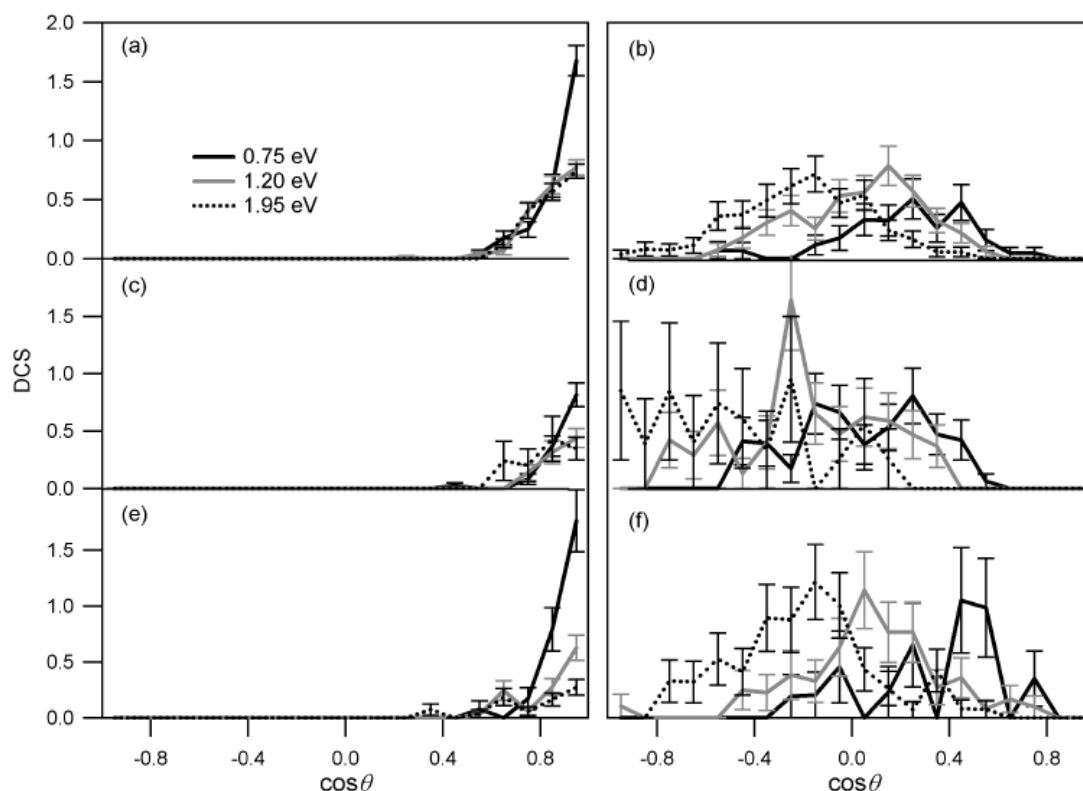
In trying to estimate the relative contributions to the total angular distribution of small and large b collisions, we also use the calculated opacity functions to plot $bP(b)$ vs. b for the three different surfaces (Figure 3-9). It is observed that, at a collision energy of 1.95 eV, on the EG surface the weight of small b collisions (the integration area for b<1.0 a_0) is about one half of the weight of large b collisions (b>2.0 a_0). At the same time, the

Figure 3-9.   Opacity functions expressed as $bP(b)$ vs b for the H + CD_4 (υ=0) → HD + CD_3 reaction at 1.95 eV collision energy.
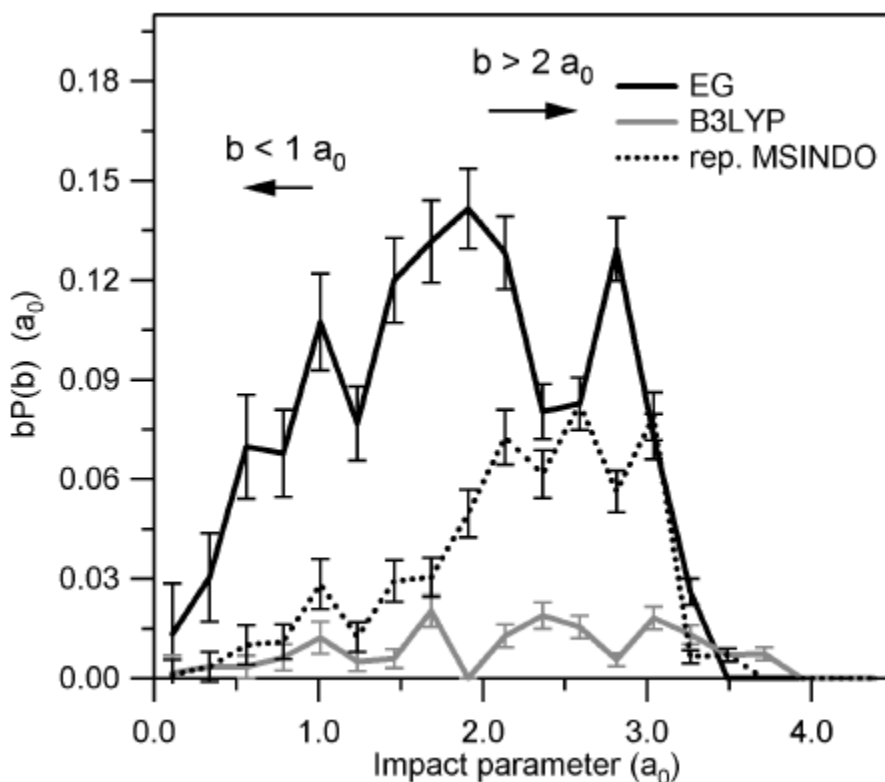
magnitude of the DCS in the forward peak of the small b angular distribution is about the

same as the maximum of the backward/sideways peak on the large b angular distribution

(the 1.95 eV curves of Figures 3-8a and 3-8b). As a result, the two impact parameter

regions contribute significantly to the total angular distribution, leading to a rather broad

CD_3 distribution with the valley between the forward peak arising from small b collisions

and the backward/sideways peak arising from large b collisions filled up by collisions

with b in the intermediate range (the 1.95 eV curve in Figure 3-7a). In contrast, on the

B3LYP surface, the weight of small b collisions is only one fourth of that of large b collisions (Figure 3-9). In addition, the magnitude of the DCSs in the backward region of the large b angular distribution is also much larger than that of the forward scattered small b angular distribution (the 1.95 eV curves of Figures 3-8c and 3-8d). Therefore forward scattering is negligible as compared to the contribution of large b collisions on the B3LYP surface, resulting in an angular distribution that emphasizes scattering into the backward hemisphere (the 1.95 eV curve in Figure 3-7b), in close agreement with experiment. On the reparametrized MSINDO surface, the contribution of small b collisions is even smaller (Figures 3-9, 3-8e and 3-8f). The contribution of large b reactive collisions, which from Figure 3-8f we know preferentially lead to sideways scattered CD_3 at 1.95 eV, is completely dominant and biases the total angular distributions in the sideways region (the 1.95 eV curve in Figure 3-7c).

Clearly, the observed angular distributions can be attributed to the difference in opacity functions on the three PESs, and the opacity functions are closely related to the cones of acceptance in the saddle point region of the surfaces. On the B3LYP and reparametrized MSINDO surfaces that have wider cones of acceptance, the contribution from sideways/peripheral reactive collisions at large impact parameters is greatly enhanced. In addition, small impact parameter nearly collinear collisions are less probable, as the flexible transition structure is less effective in "steering" the trajectory to a linear configuration as the barrier is surmounted. As a result, the wider cone of

acceptance, while leading to more reactive collisions at larger impact parameters, actually

results in a lower reaction probability at smaller impact parameters.

Figure 3-10.   Product energy disposal as a function of center-of-mass collision energy from trajectory calculations. Values are given in terms of the average fractions of the available energy appearing in (a) product relative translation; (b) HD vibration; (c) HD rotation and (d) CD_3 internal motion for the $H + CD_4$ ($\upsilon=0$) $\rightarrow HD + CD_3$ reaction.
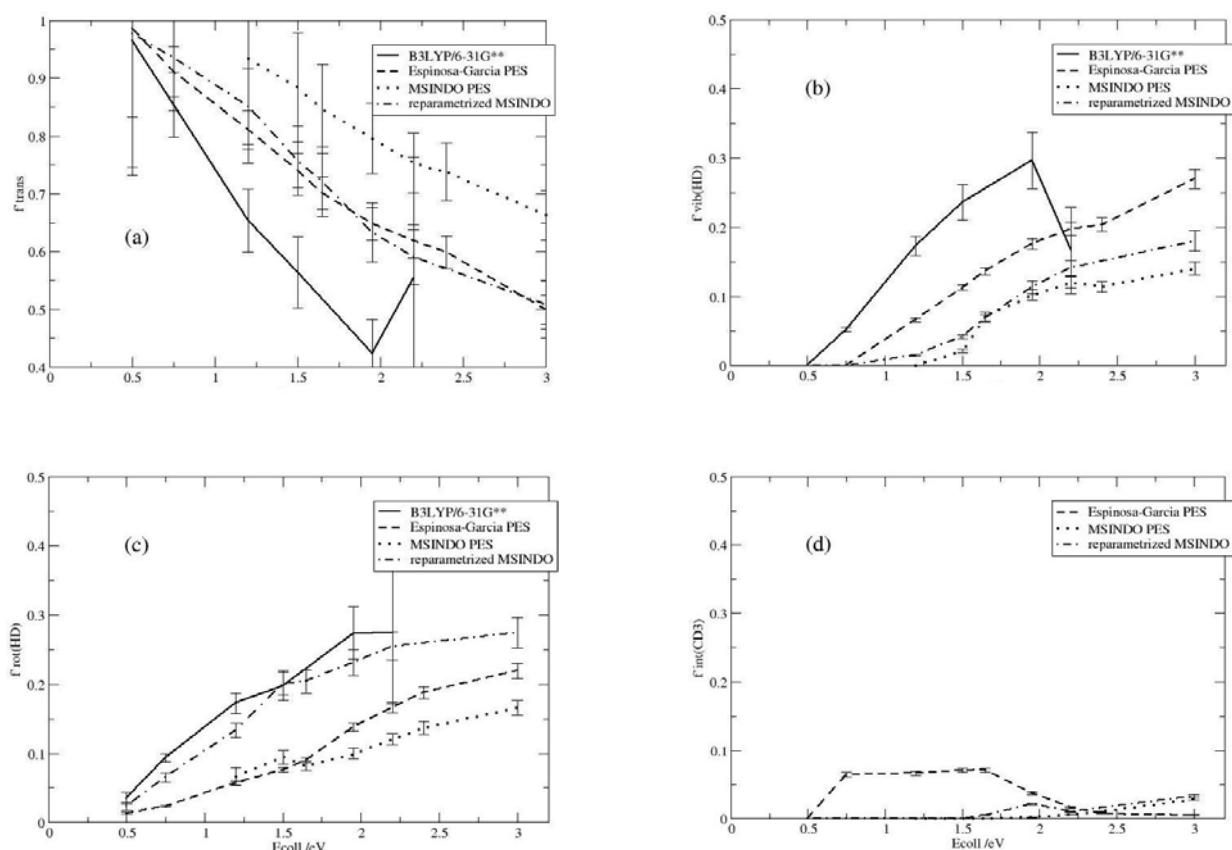
Table 3-4. Product energy partitioning for the H + CD$_4$ abstraction reaction

E$_{coll}$		Espinosa-García PES	B3LYP/6-31G**	reparametrized MSINDO	MSINDO	expt.[78]
0.75 eV	f$_T$[a]	91±4% (96±5%)	85±6% (91±6%)	93±9% (100±11%)		
	f$_{vib(HD)}$[b]	0% (4.0±0.2*)	5±0.3% (6.5±0.4)	0% (3.3±0.3*)		
	f$_{rot(HD)}$[b]	2±0.1% (0.4±0.02)	9±1% (1.7±0.1)	6±1% (1.4±0.1)		
	f$_{int(CD3)}$[b]	6±0.3% (14.5±0.7*)	0% (12.5±0.8*)	0% (15.2±1.5*)		
	%$_{HD(v'=0,1)}$[c]	100±6%	100±9%	100±11%		
1.5 eV	f$_T$	74±3% (73±3%)	56±6% (61±7%)	76±6% (75±6%)	88±9% (100±11%)	?% (84%)
	f$_{vib(HD)}$	11±0.5% (9.3±0.4)	24±3% (14.3±1.6)	4±0.3% (7.9±0.6)	2±0.2% (6.9±0.7)	7% (?)
	f$_{rot(HD)}$	8±0.3% (2.6±0.1)	20±2% (7.3±0.8)	20±2% (6.8±0.5)	9±1% (3.7±0.4)	9% (?)
	f$_{int(CD3)}$	7 ±0.3% (15.8±0.6)	0% (10.9±1.2*)	0% (16.6±1.3*)	0% (15.5±1.7*)	
	%$_{HD(v'=0,1)}$	95±6%	78±13%	99±11%	100±14%	> 95%
1.95 eV	f$_T$	65±3% (64±3%)	42±6% (45±6%)	63±5% (62±5%)	80±6% (86±7%)	
	f$_{vib(HD)}$	18±1% (13.3±0.6)	30±4% (19.7±2.7)	11±1% (11.4±0.9)	10±1% (11.1±0.8)	
	f$_{rot(HD)}$	14±1% (6.1±0.3)	27±4% (13.0±1.8)	23±2% (10.1±0.8)	10±1% (4.9±0.4)	
	f$_{int(CD3)}$	4±0.2% (15.0±0.6)	0% (10.9±1.5*)	2±0.2% (18.2±1.5)	0.2±0.02% (16.4±1.3)	
	%$_{HD(v'=0,1)}$	84±6%	53±13%	98±12%	95±11%	

* The value of the average HD vibrational energy or CD$_3$ internal energy is below HD or CD$_3$ zero-point energy.
a. Fraction of the product translational energy in the available energy. Values in parentheses are the percentages of the reagent translational energy channeled into translation of the products.
b. Fraction of HD vibrational energy/HD rotational energy/CD$_3$ internal energy in the available energy. Values in parentheses are the average HD vibrational energies/HD rotational energies/CD$_3$ internal energies in kcal mol^{-1}.
c. Percentage of the HD products formed in υ'=0, 1 vibrational states.

3.3.5 Product Energy Partitioning

There are several experimental observations concerning the CD_3 product state distributions: (1) the reaction does not significantly populate the energetically allowed symmetric stretch of CD_3 (v_1=1), (2) the major product channels are the ground state and umbrella-bending mode CD_3 (v_2=0, 1), (3) the reaction does not populate rotational levels with N>9, which indicates that only a small fraction of the total available energy goes into rotational energy of CD_3, (4) CD_3 rotates preferentially around one of the C_2 axes (tumbling motion), which are directed along a C-D bond, as opposed to the higher symmetry C_3 axis, which is perpendicular to the plane of the molecule (cartwheel-type rotation), and (5) the CD_3 internal state distribution is largely independent of the collision energy.

Figure 3-10 presents the primary results of our calculations where we display the fractions of energy in translation, f'$_{trans}$, in HD vibration, f'$_{vib}$(HD), in HD rotation, f'$_{rot}$(HD) and in CD_3 internal motion, f'$_{int}$(CD_3) as a function of the reagent translational energy for the four surfaces that we have considered. In calculating the fractions of the available energy released to HD vibration, and CD_3 internal motion, we subtract the ZPE from the energy of each fragment. [The available energy is calculated as E_{coll} +ΔH + ZPE(CD_4) − ZPE(CD_3) − ZPE(HD). In cases of ZPE violation, the fractions of the available energy released to the modes that violate the ZPE are set to zero. The available energy is renormalized so that the remaining fractions of energy add to 1.] Table 3-4

summarizes selected results from these calculations, including average product internal energies.

Figure 3-10 shows that the average fraction of energy going to product relative translation decreases with collision energy, while the fractions in HD vibration and rotation increase, and CD_3 internal motion receives relatively little of the available energy. At energies barely above threshold, product translation receives more than 90% of the available energy. This behavior is consistent with what is expected for a reaction with a late barrier where preferential translational excitation of the products is known to occur. Figure 3-10a also reveals that the slope of the B3LYP f_{trans} curve is larger in magnitude than for the rest of the surfaces, which indicates a higher preference for product internal excitation on this surface with increasing translational energy. Also note that the shift of the MSINDO curve toward higher energies reflects the higher barrier on this surface.

Figure 3-10b shows that the B3LYP $f_{vib}(HD)$ curve rises from zero at the threshold energy. This curve is shifted downward in energy by ~0.25 eV with respect to the EG and reparametrized MSINDO curves. Therefore, HD is vibrationally more excited on B3LYP than on EG, and even more excited than on the MSINDO surfaces. The TSs on the B3LYP and reparametrized MSINDO surfaces are both later than that on the EG surface (Table 3-1), but the product energy disposals found on the two surfaces are in sharp contrast to each other, with reparametrized MSINDO predicting less and B3LYP predicting more of the available energy released to HD vibration than does EG,

respectively. The reparametrized MSINDO result is in agreement with what is commonly assumed in the Polanyi rule,[16] which states that for surfaces with later barriers product vibrational excitation is suppressed, whereas the B3LYP result is not.

Figure 3-11.   Sections of the B3LYP/6-31G** potential energy surfaces for fixed H-D'-C angles of (a) 180 degrees and (b) 90 degrees. The remaining coordinates are taken to be their TS values. The energy levels are in kcal mol^{-1}.
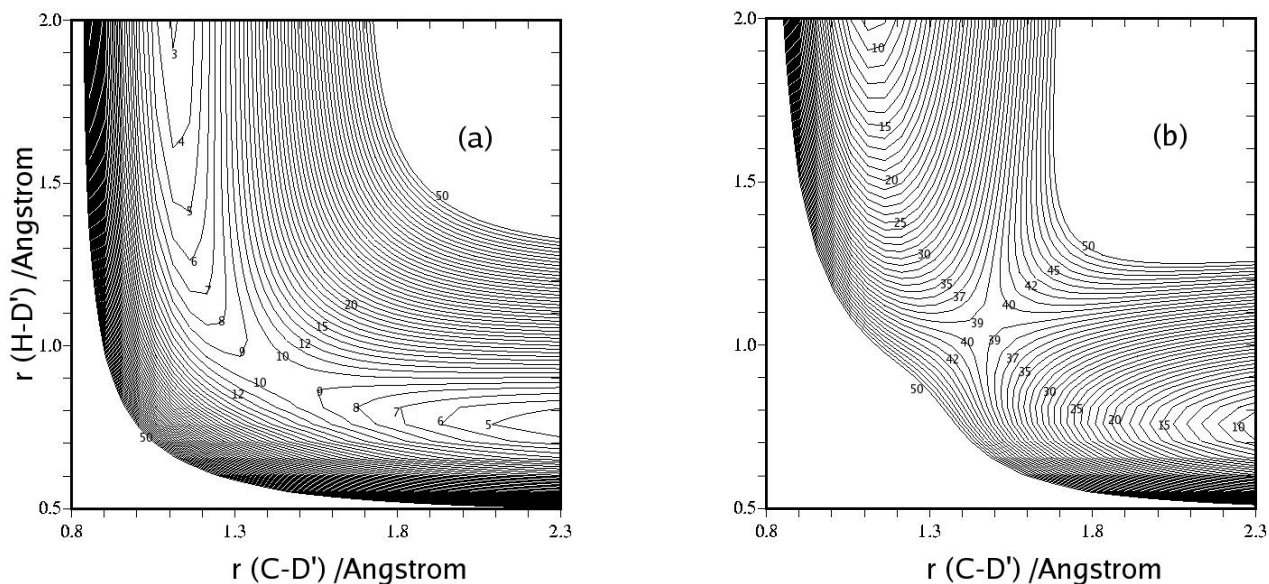
To shed light on this behavior, we have examined representative reactive trajectories on the EG, B3LYP and reparametrized MSINDO surfaces. Here we summarize the results and describe the correlation between trajectory motion and properties of the surfaces.

First let us examine contours of the PESs as a function of the H-D' and C-D' distances. In order to understand the detailed mechanism, it is necessary to keep in mind

that the reaction does not take place on the collinear potential surface, i. e., the H-D'-C angle changes during the course of the collision. Figure 3-11 presents sections of the B3LYP potential surfaces for H-D'-C bending angles of 180° and 90°. These results show that the saddle point on the bent potential surface is at larger C-D' and H-D' separations than on the collinear PES. The EG surface shows somewhat similar contours, as indicated in Figure 3-12 for a bending angle of 140°, but an important difference between EG and B3LYP is that the repulsive wall is steeper on EG in the corner region where the inner turning points occur. This is apparent from the energies that are given along a specific cut that is plotted in Figure 3-12, where we see that the difference in energy between EG and B3LYP increases from 3 kcal mol^{-1} to over 10 kcal mol^{-1} in going from the MEP to the inner corner region at a point that is roughly 60 kcal mol^{-1} above the MEP. A consequence of this is that the inner repulsive wall on EG constrains the trajectory to be closer to the MEP, and guides trajectories more efficiently toward products. On the B3LYP PES trajectories can wander more easily off the MEP, and often get reflected back to the reactants before reaching the barrier, which is later than on EG, leading to small reaction cross sections on this surface, especially at higher energies.

Another property of the potential surfaces that plays an important role in the dynamics is the anisotropy of the surfaces in the saddle point region with respect to the H-D'-C bending angle, shown as the H-D'-C bending-energy curves in Figure 3-4. We see that the EG surface is much more repulsive (i.e., the energy increases the fastest with bending the H-D'-C angle) than the B3LYP and reparametrized MSINDO surfaces. This

result means that the cone of acceptance is wider on B3LYP than on EG. Consequently,

the contribution of large impact parameter reactive collisions, in which H attacks in the

sideways direction, can be greatly enhanced on B3LYP. Figure 3-4 also shows that the

B3LYP result is the closest to the higher quality QCISD(T) curve, so B3LYP is likelier to

provide a more nearly correct description of the dynamics.

Figure 3-12.   Sections of the (a) EG and (b) B3LYP potential surfaces for a fixed
H-D'-C angle of 140 degrees. Energies at the points (D'-C, H-D')= (1.0, 0.667), (1.1,
0.75), (1.2, 0.833), (1.3, 0.917), (1.4, 1.0), (1.5, 1.083), (1.6, 1.167), (1.7, 1.25), (1.8,
1.333), (1.9, 1.417) are marked in kcal mol^{-1}.
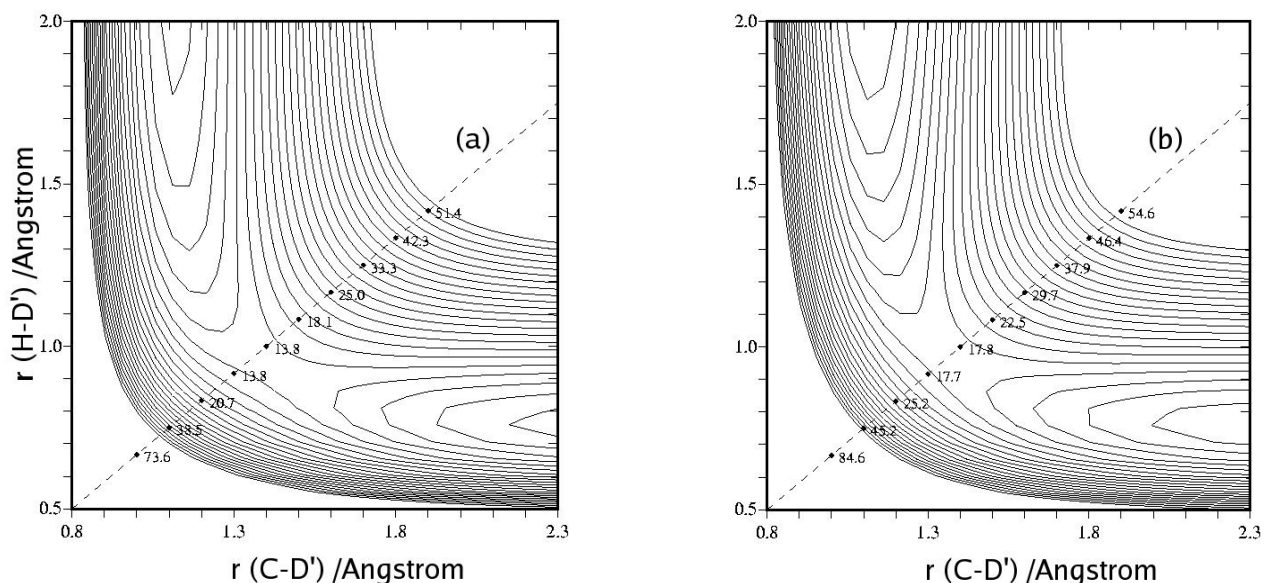
We examine how these potential surface properties correlate with results from

trajectory calculations. In Figure 3-13 we plot the H-D'-C bending angle versus step

number (the time steps here are 0.48 fs, which is twice the trajectory time step) for

reactive trajectories with large impact parameters ($b>2.0$ a_0) at 1.95 eV on B3LYP and EG. The first inner turning points occur at steps 54–70, so the approach region corresponds to roughly the first 50 steps. In this region we see quite different values for the H-D'-C angles, with average values at $t=0$ of 124° on EG and 109° on B3LYP. This result clearly demonstrates a wider cone of acceptance on B3LYP. A consequence of this wider cone of acceptance is obvious by examining the opacity function in Figure 3-14. It is shown that although the overall reaction probability is larger on EG than on B3LYP (due to the earlier barrier location on EG), the reactive region on B3LYP extends to larger impact parameters ($b>4.0$ a_0). Large impact parameter reactive collisions also contribute more significantly to overall reactivity on B3LYP than on EG. We already showed that the large impact parameter collisions led to angular distributions that were more influenced by stripping dynamics than rebound dynamics. Here we will see that they also play an important role in the product energy partitioning.

Figure 3-13. H-D'-C angle versus time for a random selection of large-impact-parameter ($b > 1.06$ Å) reactive trajectories at 1.95 eV with (a) showing results for B3LYP surface and (b) results for EG.
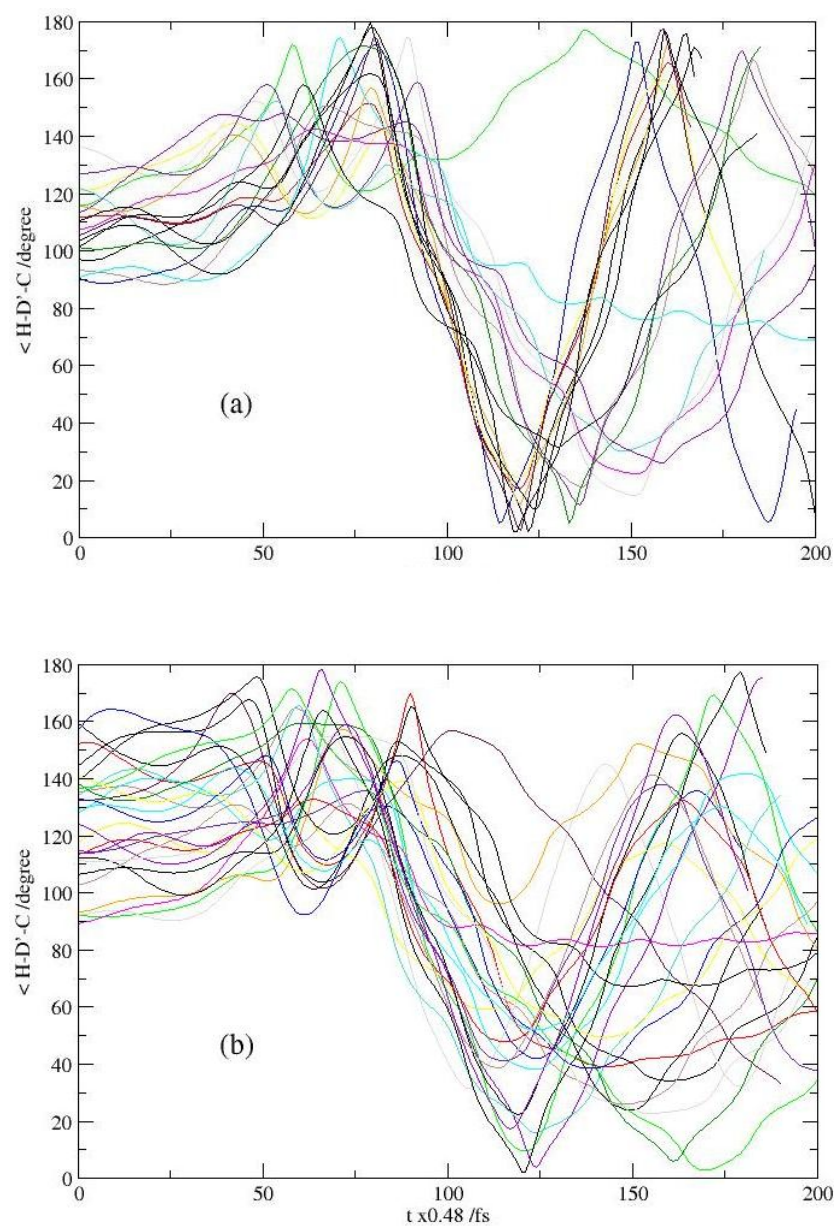
Figure 3-14. Opacity functions expressed as *bP(b)* vs. *b* for the B3LYP and EG surfaces at 1.95 eV.
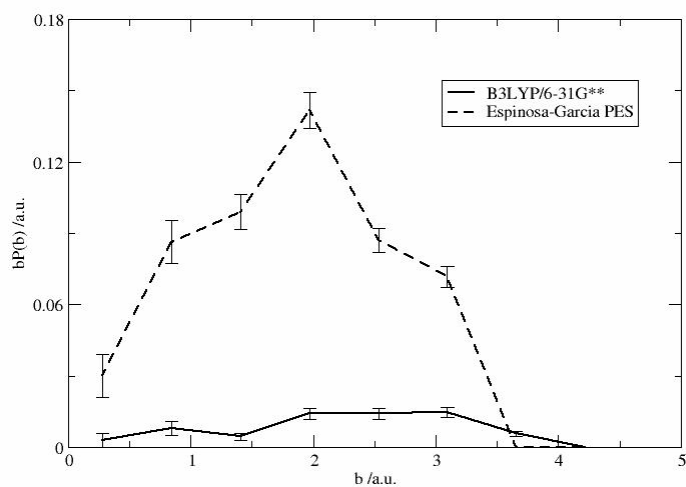
Figure 3-15.   Average HD vibrational energy as a function of impact parameter for the EG and B3LYP potential surfaces.
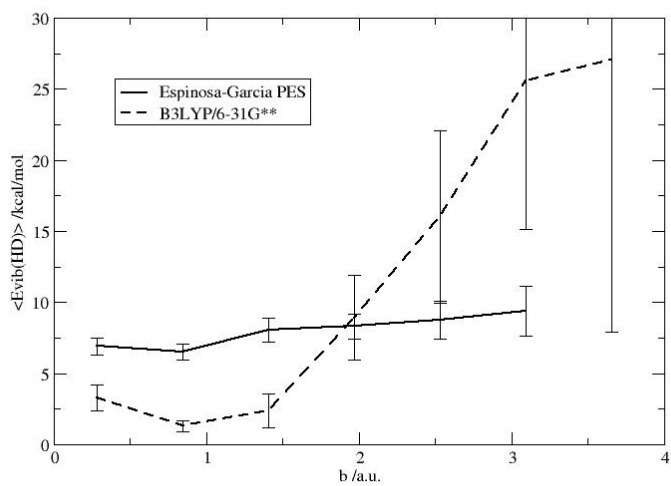
Figures 3-15 and 3-16 present average energies deposited in HD vibration and rotation as a function of impact parameter for the B3LYP and EG surfaces. They show that the EG energies are not strongly dependent on impact parameter (increasing or decreasing slowly). However on B3LYP, the HD vibrational energy increases very rapidly from a value that is below EG at small b to a value that is well above EG at large b. Because the contribution of large b collisions is dominant on B3LYP, HD is vibrationally more excited on B3LYP than on EG. As for HD rotation, although the B3LYP energies decrease rapidly with increasing impact parameter for $b > 1.5$ a_0, they largely stay well above the EG result, leading to an average HD rotational energy that is higher than on EG.

Figure 3-16.   Average HD rotational energy as a function of impact parameter for the EG and B3LYP potential surfaces.
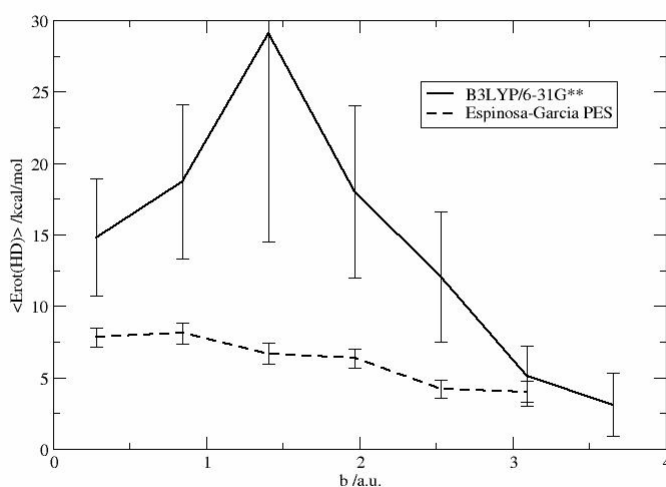
The limiting case of large impact parameter collisions should give stripping behavior at high energies, so it is useful to calculate the average energy transfer into internal motions (vibration plus rotation) of HD using a simple kinematic model, in which we assume the CD_3 radical acts as a spectator. An elementary calculation estimates that at 1.95 eV, the average HD internal energy from stripping dynamics should be ~30 kcal mol^{-1} (~1.3 eV). This is actually what is obtained when adding the average B3LYP vibrational and rotational energies in Figures 3-15 and 3-16 in the large b limit. (In fact for a few large b trajectories on B3LYP, the HD vibrational energy alone exceeds this limit). Thus we see that the trajectories on B3LYP are very effective in converting reagent translational excitation into product internal excitation. One factor that contributes to this result is the softer inner repulsive wall on the B3LYP surface (noted earlier in the discussion of Figure 3-12.) In our examination of the B3LYP trajectories we find that reactive trajectories at large b climb up the inner repulsive wall while rounding the corner between reactant and product regions. This motion leads to a bobsled effect that very efficiently converts reagent translational energy to product vibrational excitation. On EG the majority of the large b trajectories more closely follow the MEP because of the steeper inner repulsive wall on this surface. The reparametrized MSINDO surface has much narrower wells in both the reactant and product regions than EG or B3LYP. This makes the inner repulsive wall even steeper than on EG, so the comparison between reparametrized MSINDO and EG is more typical of behaviors predicted by the Polanyi rules.

3.3.6 CD$_3$ Rotational Distributions and Comparisons with REMPI Results

Let us also consider the CD$_3$ internal energy disposal. We see in Figure 3-10d that although all of the calculations indicate that less than 10% of the available energy goes to CD$_3$ internal motion, the different surfaces do not agree. Particularly on the EG surface, f'$_{int}$(CD$_3$) increases rapidly until reaching a plateau at 0.75 eV, then gradually decreases at energies above 1.65 eV. The other surfaces show essentially zero values of f'$_{int}$(CD$_3$) for energies below 1.5 eV, meaning that the CD$_3$ energies are below the zero point energy. As a result, CD$_3$ is more excited on EG than on the other surfaces at low and intermediate energies. ZPE violation is a well-known flaw associated with QCT calculations, but the fact that the calculated CD$_3$ internal energy is so small at least points to the fact that the average energy available to the CD$_3$ product is very limited. For the most part, this result is what we find in our experimental measurements of the product state, where vibrationally and rotationally cold CD$_3$ is produced. There are, however, trajectories on the EG, B3LYP, and reparametrized MSINDO surfaces in which the CD$_3$ internal energy well exceeds the ZPE. By animating such trajectories, we find that the umbrella bending motion has large amplitude. This behavior is to be expected, of course, as the D$_3$C-D'-H transition state is pyramidal but the equilibrium geometry of CD$_3$ is planar. Indeed, umbrella bend excitation is seen in the measurements. Our trajectory analysis also shows little possibility of CD$_3$ stretch excitation on these surfaces, which is again in agreement with experiment.

To analyze more deeply the CD_3 internal distribution, we calculate the CD_3 rotational state distributions and compare them with the qualitative picture drawn from experiment. Results for the EG, B3LYP and reparametrized MSINDO surfaces are displayed in Figure 3-17. It is immediately observed that CD_3 is rotationally the coldest on B3LYP, and hottest on reparametrized MSINDO. On EG and B3LYP, the CD_3 rotational distributions are relatively narrow and peak at $N = 8$, 9, 10 and $N = 5$, 6, respectively. Although the EG and B3LYP distributions are largely independent of the collision energy, the reparametrized MSINDO distribution broadens and gradually shifts to higher rotational levels as collision energy increases. Irrespective of the higher rotational level tail, the B3LYP results are in best agreement with the experiment, in which it is observed that at 1.78 eV collision energy the methyl radical does not populate states with $N > 9$.

Both experiment and theory also agree that the CD_3 rotates preferentially around the C_2 axes, instead of the higher symmetry C_3 axis. For example, at 1.95 eV (45 kcal mol^{-1}) the CD_3 rotational energies associated with the two C_2 axes and the C_3 axis (averaged over all reactive trajectories) are 0.46, 0.46, 0.065 kcal mol^{-1} on B3LYP, 0.50, 0.45, 0.25 kcal mol^{-1} on EG, and 1.32, 1.36, 0.57 kcal mol^{-1} on reparametrized MSINDO. This intuitive result appears to be general for H-abstractions from methane as a similar preference for alignment of the methyl rotational angular momentum about the C_2 axes has been observed in both the Cl + CH_4[132] and F + CH_4[133] reactions.

Figure 3-17.   CD$_3$ rotational states distribution at different collision energies on the (a) EG, (b) B3LYP, and (c) reparametried MSINDO potential surfaces.
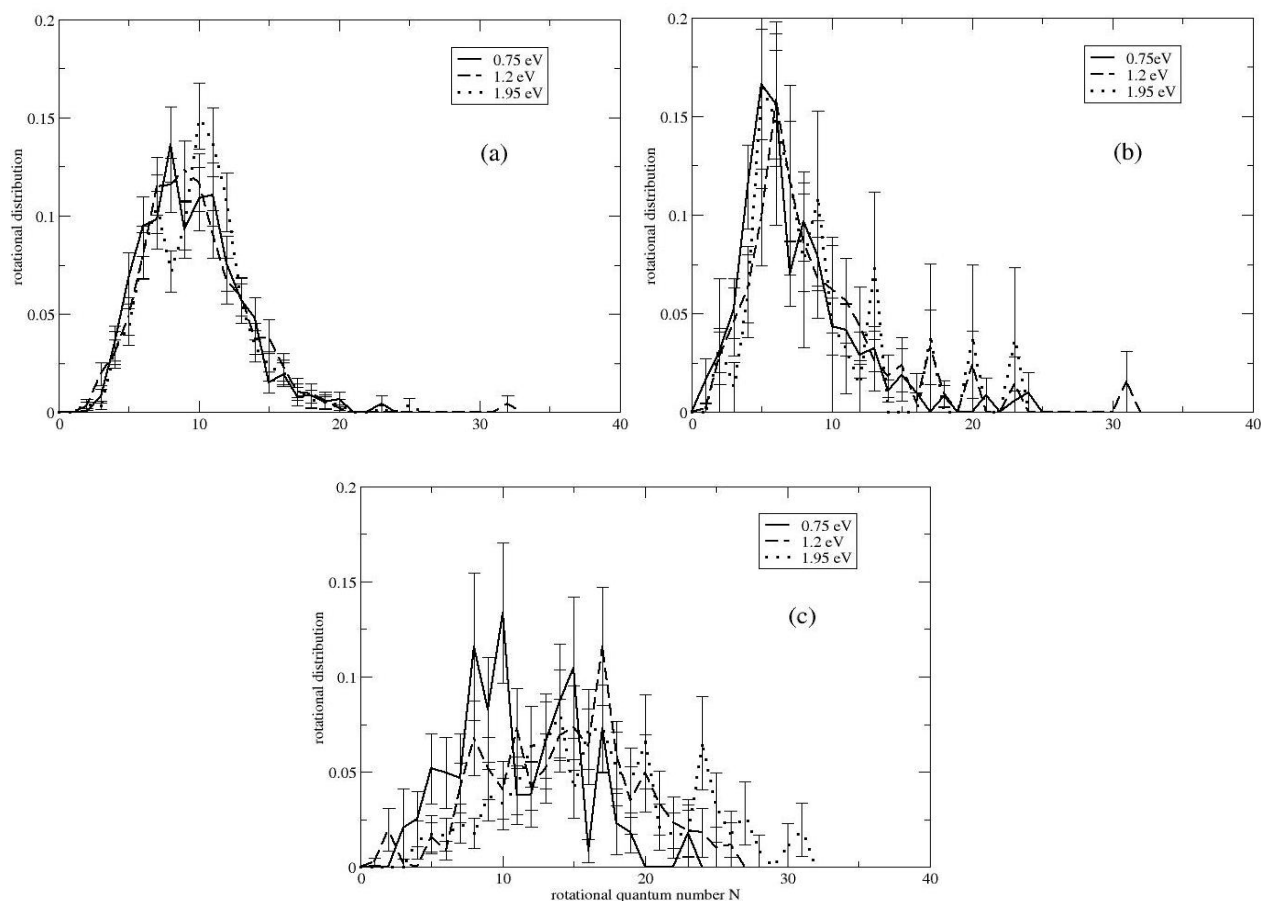
3.3.7 Comparison with CARS Experiments

Valentini and coworkers[78] measured the HD product quantum state distributions at 1.5 eV using coherent anti-Stokes Raman spectroscopy. The HD product was found to be vibrationally cold (more than 95% formed in υ'=0 and 1). Only 7% of the available energy went to HD vibration and 9% to HD rotation.

Our calculations on B3LYP, however, predict a vibrationally (24%) and rotationally (20%) much hotter HD product. This large discrepancy between the CARS experiment and the B3LYP results is quite unexpected considering the good agreement of B3LYP with the current experiment for other dynamical properties. Actually the B3LYP results are to a certain extent similar to what was found in studies of the isoelectronic H + H_2O(000) reaction. QCT calculations for that reaction on an accurate PES,[129] which is characterized by a saddle point that is similarly late (O-H' and H-H' distances are 1.36 Å and 0.84 Å, respectively) but much higher in energy (21.7 kcal mol^{-1}), gave 13% of the available energy going to H_2 vibration, 18% to H_2 rotation and 64% to product translation at a collision energy of 2.2 eV. Experiments done at this energy[134] only determined the sum of H_2 vibration and rotation, but this result, 31%, and the fraction of energy going to translation, 65%, were in excellent agreement with the calculations.

Inspection of the CARS experiment reveals that Valentini and coworkers generated H atoms by photolysis of HI at 266 nm. The H atoms have laboratory translational energies of 1.62 eV (quantum yield = 0.66) and 0.68 eV (quantum yield = 0.34), corresponding to the respective 1.53 ± 0.15 eV and 0.65 ± 0.10 eV H + CD_4 collision energies. Based on trajectory calculations using an early semiempirical PES,[89] they assumed that the reactive cross section at 0.68 eV is negligible compared to that at the higher collision energy. In contrast, our calculations on B3LYP indicate that the reaction cross section is 0.76 a_0^2 at 0.65 eV, while it is only 0.45 a_0^2 at 1.5 eV. Therefore,

we suggest that the contribution of the slow channel is not negligible compared to that of the fast channel and the conclusions of the CARS study might need to be reinterpreted.

Because the B3LYP barrier is too low, a possible concern is that our calculation overestimates the role of the reaction of slow H atoms. However, we note that the classical barrier from very high level *ab initio* calculations, extrapolated to the basis set and correlation energy limits,[110] is 0.58 eV. The zero-point corrected barrier based on this value is 0.52 eV, which is close to the experimental enthalpy of activation at 300 K, 0.50 eV,[135] and about 0.13 eV below the center-of-mass collision energy of the slow channel. Besides, the experimental reaction cross section was found to decrease with increasing translational energies in the 1.48–2.36 eV range, meaning that the peak reactive cross section must occur at an energy below 1.48 eV. Combining these results and the small absolute cross section at 1.5 eV (only 0.50 ± 0.11 a_0^2) given by the measurements of Valentini and coworkers, we estimate that the cross section of the slow channel should not be smaller than one fourth of that of the fast channel.

Although the present REMPI experiments do not directly measure the HD product state distributions, we can determine the average HD internal energy by measuring the lab frame anisotropy β_{lab} of the CD_3 co-product and comparing it to what we calculate on the surfaces. The spatial anisotropy of the product is given by:

$$\beta_{lab} = \beta_{phot} P_2(\cos\alpha) \qquad (3\text{-}2)$$

where β_{phot} is the photolysis anisotropy parameter, which describes the photofragment angular distribution resulting from photolysis of the precursor HBr or HI molecule with

linearly polarized light and takes on values from −1 to +2, $P_2(\cos \alpha)$ is the second-order

Legendre polynomial, and α is the angle between $\hat{v}_{CD_3}$, the CD$_3$ lab frame velocity, and

$\hat{u}$, the HCD$_4$ center-of-mass velocity, as described by the vector relationship shown in

Figure 3-18.

Figure 3-18. Newton circle for a typical *photoloc* experiment. u_{COM} is the velocity of the HCD$_4$ center of mass, u_{CD_3} is the velocity of the CD$_3$ product in the center-of-mass frame, and v_{CD_3} is the CD$_3$ lab-frame speed, and θ is the center-of-mass scattering angle measured with respect to the direction of the incident H atom.
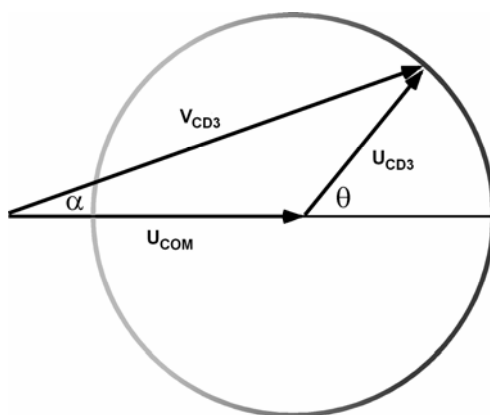
It is clear that for a specific lab frame speed v_{CD_3}, the CD$_3$ velocity in the center

of mass frame, u_{CD_3}, is determined by α, while u_{CD_3} relates to the state-to-state

energetics ΔE of the reaction through:

$$u_{CD_3} = \frac{m_{HD}}{M} \left[\frac{2(E_{coll} - \Delta E)}{\mu'} \right]^{1/2} \qquad (3\text{-}3)$$

Here $M = m_{HD} + m_{CD3}$, and μ' is the reduced mass of the products. Therefore, measurements of the CD_3 lab frame speed and anisotropy for a given CD_3 product state, will allow a unique determination of the HD internal energy. However, in practice we can only measure the average anisotropy for a specific lab frame speed, $\beta_{lab}(v_{CD_3})$.

Figure 3-19 compares the CD_3 lab frame speed distribution and anisotropy as a function of speed from experiment and theory at 1.95 eV. Note that the 1.95 eV experiment has a small contribution from the H atoms that coincide with spin-orbit excited Br (the slow channel); therefore, the theoretical curves are the weighted sum of the slow channel (E_{coll} =1.5 eV) and the fast channel (E_{coll} =1.95 eV). Because we state-selectively detect CD_3 ($v = 0$) the speed-dependent anisotropy can be used to estimate the average internal energy deposited in HD for given values of v_{CD_3}.

Figure 3-19 shows that the B3LYP calculations agree very well with experiment for both the speed distribution and the speed-dependent anisotropy, which suggests to us that the overall energy partitioning scheme predicted by B3LYP should be reliable at least for this collision energy. On EG, the average CD_3 anisotropy is higher, or the average α and, in turn, the average u_{CD_3}, is larger than the experimental measurement in a given speed bin, which translates to smaller HD internal energy. This, when combined with the fact that the EG speed distribution is shifted to higher speeds by several hundred of m s^{-1} with respect to the experimental curve, implies that the HD internal energy predicted by EG is too small compared to the current experimental measurements. We also did measurements at 1.2 eV, and the results show that the B3LYP lab frame

anisotropy and speed distribution also agree with experiment within the experimental uncertainty. Thus, we suggest that the estimation of the amount of internal excitation in the HD product determined by Valentini and coworkers is likely to be too low.

Figure 3-19.   Experimental and calculated (a) CD$_3$ lab frame anisotropy β_{lab} as a function of speed and (b) CD$_3$ lab frame speed v_{CD_3} distribution at 1.95 eV.
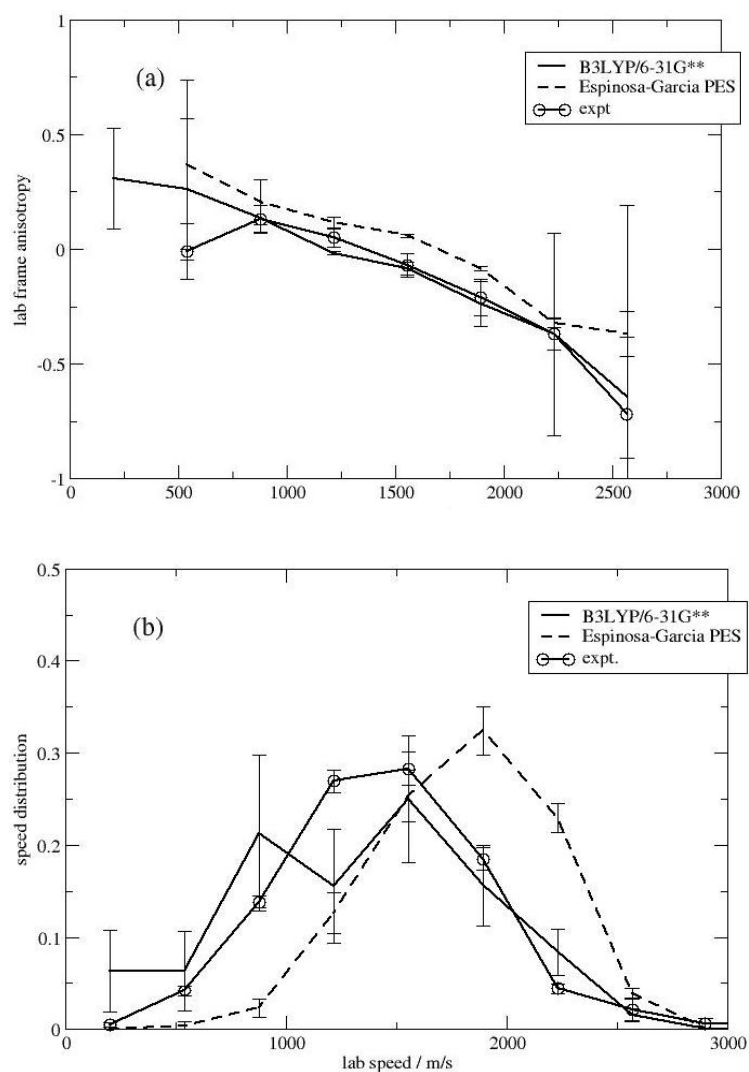
3.4 Summary

In this chapter, we extensively compare full-dimensional QCT calculations with *photoloc* experiments for the excitation function, product speed and angular distributions, as well as product energy partitionings in the H + CD_4(v=0) → CD_3 + HD reaction at collision energies ranging from 0.5 to 3.0 eV. In contrast to early theoretical calculations, the angular distributions in the present study show behaviors associated with a stripping-type mechanism, leading to mainly sideways and backward scattered CD_3 at intermediate and high collision energies.

We find the best agreement between current experiments and B3LYP/6-31G(d, p) direct dynamics calculations in almost every aspect of the scattering dynamics that we have examined. This result might at first be surprising because the barrier height is ~0.2 eV too low on B3LYP. In particular, the saddle point on B3LYP is more product-like than the other surfaces that we have examined, including the analytical EG surface and surfaces based on the MSINDO semiempirical Hamiltonian, but leads to higher HD vibrational excitation, which is contradictory to the Polanyi rules. The different dynamical behaviors found on these surfaces are interpreted using an analysis of the opacity functions, where we find close correlations between the cone of acceptance in the saddle point region of the PESs and the reactive cross sections, product angular distributions and HD rovibrational excitations. We believe that the B3LYP surface provides overall a

better description of the surface for regions well away from the minimum energy path, and it is such regions which dominate in the high energy reaction dynamics.

Our study demonstrates that comparisons of full-dimensional theoretical calculations to state-resolved scattering experiments are now feasible for this simplest six-atom system, but a proper description of the detailed reaction mechanism is highly dependent on the quality of the PES.

Chapter 4   O (^3P) Collisions with Ethane at Hyperthermal Energies

4.1 Introduction

The electronically ground-state oxygen atom O (^3P) reactions with hydrocarbons have been the subject of intensive studies in areas ranging from combustion and atmospheric chemistry[136-138] to chemical processing of hydrocarbon surfaces.[139] Among these, the reactions of O (^3P) with alkanes (C_nH_{2n+2}) at low collision energies, where the only reactive channel is H abstraction

$$O\ (^3P) + C_nH_{2n+2} \rightarrow OH\ (^2\Pi) + C_nH_{2n+1} \qquad (4\text{-}1)$$
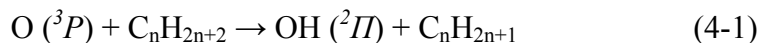
have been extensively studied to determine thermal rate constants[140-142] and product internal state distributions.[136, 137] Such as the recommended rate constant expression for the O (^3P) + C_2H_6 abstraction reaction in the temperature range of 300–1200 K is

$1.66 \times 10^{-15} T^{1.5} e^{-2920 K/T} cm^3 molecule^{-1} s^{-1}$.[143] The reaction exothermicity and activation barrier of Eq. (4-1) will vary depending on the type of the abstracted hydrogen atom.[140, 141] In particular, the activation energies were found to be 29, 19, and 14 kJ mol^{-1} for abstraction of a primary, secondary, and tertiary hydrogen atom, respectively. Furthermore, the tertiary and secondary alkyl radicals coming from abstraction of hydrogen atoms initially bound to the central carbon are more stable than the primary alkyl radicals. There is also a correlation between the OH product rovibrational excitations and the involved hydrogen atom type.[136]

In addition to OH formation, there are two other primary reactive pathways that might exist for O (^3P) collisions with alkanes at higher relative translational energies:

$$O\ (^3P) + C_nH_{2n+2} \rightarrow H\ (^2S) + C_nH_{2n+1}O \qquad (4\text{-}2)$$

$$O\ (^3P) + C_nH_{2n+2} \rightarrow C_mH_{2m+1}O + C_{(n-m)}H_{2(n-m)+1} \qquad (4\text{-}3)$$
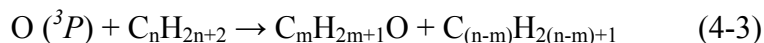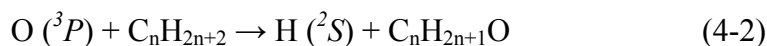
During the H elimination process of Eq. (4-2), the oxygen atom exchanges with a hydrogen atom to produce an alkoxy radical. While Eq. (4-3) involves a C–C bond breakage mechanism as O adds onto the hydrocarbon chain to generate an alkyl radical and an alkoxy radical. These higher-barrier reactions are particularly relevant to problems related to degradation of the hydrocarbon polymer surface of a spacecraft orbiting in low Earth orbit (LEO).[144]

At LEO altitudes (~200 to 700 km), atomic oxygen O (^3P) is the dominant species due to solar VUV photodissociation of O_2.[145] Spacecraft travels in LEO at a velocity of ~7.8 km s^{-1}, resulting in collisions with ambient oxygen atoms at relative translational

energies of ~5 eV (115 kcal mol^{-1}). Under such harsh conditions, both inelastic scattering in which the O atoms simply transfer some of their incident translational energy to the surface and chemical reactions by surmounting the potential barriers along the reaction coordinates, leading to various molecular and radical products, are possible. The important role that atomic oxygen plays in materials erosion in LEO environment was first recognized by after-flight analysis revealing loss of surface gloss and concomitant weight loss, as well as premature aging of the paint surface.[146, 147] Since then vigorous experimental efforts have been devoted to investigating the mechanism and possible mitigation of surface degradation due to atomic oxygen in LEO.[144]

In collaboration with the Minton group of Montana State University, our group has recently been involved in modeling the O (^3P) atom reactions with short-chain saturated hydrocarbons, including methane, ethane, and propane, under hyperthermal conditions.[148] These simple gas phase reactions serve as model systems for understanding the more complicated gas-surface interactions involved in LEO erosion. These studies demonstrate that other than the well-studied lowest-barrier H abstraction channel, triplet oxygen can also add onto the hydrocarbon chain at hyperthermal energies. One study[149] that used a quantum mechanics/molecular mechanics (QM/MM) interaction potential to simulate hyperthermal collisions of O (^3P) with alkane thiol self-assembled monolayers (SAMs) on Au (111) surfaces showed similar reaction mechanisms to those in O + alkane gas phase collisions, i. e., H abstraction to generate OH, O addition to the SAM followed by elimination of an H atom or an alkyl radical.

In this chapter, we present the results of combined crossed-molecular beams and QCT studies of the O (^3P) + C_2H_6 reaction at collision energies in the ~30 to 100 kcal mol^{-1} range. The C-C bond breakage mechanism is supposed to be responsible for significant surface mass loss caused by single O (^3P) attacks in LEO, while O + ethane is the simplest atomic oxygen and saturated hydrocarbon reaction where C-C breakage can occur. Previous experimental and theoretical studies concentrate on the lower-energy abstraction reaction O (^3P) + C_2H_6 → OH + C_2H_5. Although kinetic data for this reaction has been known for a long time,[140, 150, 151] there are very few work contributed to understanding the dynamics of the reaction. By photolysing NO_2 at short wavelengths (~250–350 nm), McKendrick and coworkers[137] were able to detect the nascent OH product from O (^3P) reactions with methane and ethane. They found very low fractions of OH rotational energy release, consistent with earlier observations for larger saturated hydrocarbons.[136(a)]

There are a wealth of theoretical calculations of the energetics associated with the O (^3P) + CH_4, O (^3P) + C_2H_6 abstraction reactions and related secondary steps. The readers are referred to Ref. 152 for a detailed discussion. For the higher barrier reactive pathways, Massa and coworkers[153] performed *ab initio* calculations of the C-C bond breakage transition state for O + ethane, and the barrier was determined to be 41.1 kcal mol^{-1} at the complete basis set extrapolation CBS-QB3 level. Further studies by Schatz and coworkers[148(b)] identified three main reactive pathways under hyperthermal conditions, i. e.,

$$O\ (^3P) + C_2H_6 \rightarrow OH + C_2H_5 \qquad\qquad (4\text{-}4)$$

$$O\ (^3P) + C_2H_6 \rightarrow H + CH_3CH_2O \qquad\qquad (4\text{-}5)$$

$$O\ (^3P) + C_2H_6 \rightarrow CH_3 + CH_3O \qquad\qquad (4\text{-}6)$$
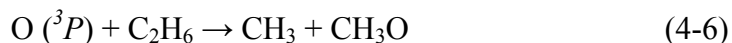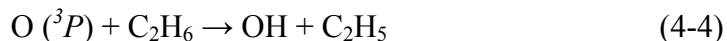
For Eqs. (4-5) and (4-6), respectively, two different configurations of the transition state were located. At the highest level of theory calculated, CCSD(T)/cc-pVTZ energies at the UMP2/cc-pVTZ optimized geometries, the barrier heights range from 9.6 kcal mol^{-1} for H abstraction, 50.5/56.7 kcal mol^{-1} for H elimination, to 47.6/60.5 kcal mol^{-1} for C-C breakage. They further carried out direct dynamics calculations with the MSINDO semiempirical Hamiltonian at collision energies from just above the abstraction barrier to relevant to LEO environment. A limited number of B3LYP/6-31G* trajectories were also computed at a hyperthermal energy of 71.5 kcal mol^{-1}. The most rigorous quantum chemistry calculations were performed by Hase and coworkers[152] for Eqs. (4-4) and (4-6) using multireference configuration interaction theory with single and double excitations corrected for quadruple excitations through the Davidson correction (MRCI+Q) with complete basis set extrapolation (CBL). The geometries were optimized using CASSCF and CASSPT2 wavefunctions with cc-pVTZ basis sets. We will compare the results by different authors in later discussions.

The present work emphasizes the dynamical behaviors at energies well above the abstraction threshold, including extensive comparisons of the MSINDO and B3LYP direct dynamics calculations with crossed-beams experiment carried out by the Minton group.

4.2 Experiment Brief

The experiments employed a crossed-molecular-beams apparatus[154, 155] coupled to a laser-detonation source.[156] Pulsed beams of pure C_2H_6 traveling at ~800 m s^{-1} were created by a supersonic expansion through a piezoelectric pulsed valve. The ethane beam was crossed at right angles by a pulsed hyperthermal beam containing ~70% ground electronic state oxygen atoms O (^3P) (with the balance being ~30% O_2) produced by the laser detonation source. Before reaching the main scattering chamber, the oxygen-atom beam was velocity selected using a synchronized chopper wheel rotating at 300 or 400 Hz. Three different average O-atom beam velocities were used to obtain dynamical information on the title reaction, 8.40 km s^{-1}, 8.44 km s^{-1} and 8.5 km s^{-1}, each corresponding to roughly 90 kcal mol^{-1} center-of-mass collision energy. Velocity spreads (FWHM) of the beams ranged from 530 m s^{-1} when the 300 Hz chopper wheel was used to 440 m s^{-1} with the 400 Hz chopper wheel. The fraction of O_2 in the beams ranged from 20 to 40 percent, depending on the beam conditions, with higher velocity beams generally containing less O_2.

Reaction products and elastically (or inelastically) scattered products from the crossing point of the two beams traveled 33.7 cm where they entered the Brink-type ionizer (held at ~10^{-12} torr). Species entering the detector were ionized, mass selected with a quadruple mass filter, and counted using a Daly-type ion counter. Number density

distributions, *N(t)*, of mass-selected species (according to the mass-to-charge ratio *m/z*) were collected as a function of their arrival time in the ionizer, which are often referred to as time-of-flight (TOF) distributions. The entire detector rotates around the crossing point of the two beams, allowing acquisition of product angular scattering information. The range of detector angles used for data collection in this study was 7.5°to 50°and is shown as the gray shaded region in the Newton diagram of Figure 4-1. [The O-atom beam direction is taken to be a laboratory angle of zero, and the positive angular direction is defined by a rotation from the O-atom beam toward the ethane beam.]

Figure 4-1.   A Newton diagram for the $O(^3P)$ + C_2H_6 reaction at E_{coll} = 90 kcal mol^{-1}. The laboratory angular range accessible in the experiment is shown as the shaded region. The blue circles represent the maximum possible velocities for the inelastically scattered products. The scattered ethane (inner blue line) and scattered oxygen atoms (outer blue line) are shown. The red circles represent the maximum possible velocities for the H-atom abstraction products, in which the products formed are C_2H_5 (inner line) and OH (outer line). The purple circle represents the maximum possible velocity for the ethoxy (OC_2H_5) product. The green circle represents the maximum possible velocity for the OCH_3 product in the C–C bond breakage channel.
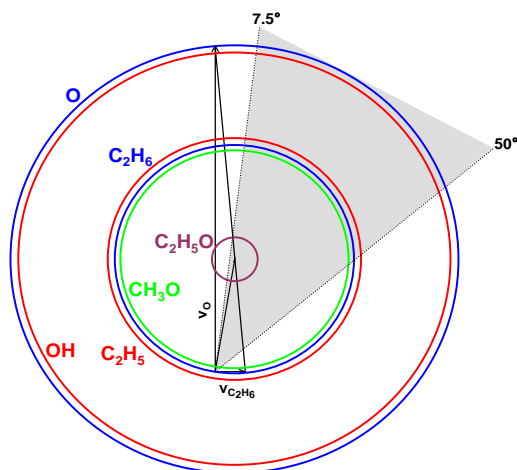
All data are collected in the laboratory frame of reference. In order to derive center-of-mass quantities, such as product translational energy distributions, *P(E)*, and angular distributions, *T(θ)*, a forward convolution approach[157, 158] was carried out for the laboratory TOF and angular distributions data.

The experiments also examined the ethoxy channel as a function of collision energy. TOF distributions were collected at lab angles of 9.5°to 11.5°for *m/z* = 43, which was found to be one of the strongest ionizer fragments of the ethoxy product. The five collision energies that have been examined are 69 kcal mol^{-1}, 72 kcal mol^{-1}, 80.4 kcal mol^{-1}, 89 kcal mol^{-1}, and 97 kcal mol^{-1}, corresponding to average O-atom beam velocities of 7.41 km s^{-1}, 7.54 km s^{-1}, 7.99 km s^{-1}, 8.40 km s^{-1}, and 8.79 km s^{-1}, respectively.

4.3 Theoretical Details

4.3.1 Quantum Chemistry Calculations

Prior to calculations of the quasiclassical trajectories, stationary points along the three major reactive pathways that may take place under the hyperthermal conditions, i.e., H-atom abstraction, H-atom elimination and C-C bond breakage, are characterized by electronic structure calculations utilizing the MSINDO semiempirical Hamiltonian[121] and the higher quality DFT method B3LYP[122] with a 6-31G** basis set. These methods will later be applied in our direct dynamics calculations. The DFT calculations have been performed with the Q-Chem package of programs.[123]

Figure 4-2. Transition state structures for the O (^3P) + C$_2$H$_6$ reaction as calculated by MSINDO, B3LYP/6-31G** (values in parentheses) and UMP2/cc-pVTZ (values in brackets) from reference 148(b). Bond lengths are in Angstroms, bond angles and dihedral angles are in degrees.

H abstraction   TS1

O
1.200
(1.208)
[1.239]
(175.1)
[177.9] H1   177.3
108.9
(106.8)
1.232
(1.311)
[1.232]
C2 —1.504— C1
(1.507)
[1.501]
H

<OH1C1C2 = 178.9 (-0.03) [-7.6]

H elimination   TS2

H2
106.5
(104.9)
[93.8]
O
1.524 (1.672) [1.651]
C2 —1.524— C
(1.529)
[1.530]
H
100.5
(92.7)
1.312 (1.468) [1.350]
H1
<OC1H1 = 152.9 (162.4) [174.6]
<OC1C2H2 = -2.56 (-6.7) [-0.7]

H elimination   TS3

H4
1.502
(1.588)
[1.582]
O
H2
H1
C2 —1.523— C1
(1.544)
[1.523]
1.133 (1.116) [1.110]
H3
rC1H1 = 1.207 (1.210) [1.179]
rC1H2 = 1.207 (1.210) [1.179]
<OC1C2 = 119.4 (121.8) [119.6]
<OC1H1 = 73.9 (78.2) [77.3]
<OC1H2 = 73.9 (78.2) [77.3]
<OC1H3 = 128.0 (124.4) [127.3]
<OC1C2H4 = 0.6 (0.04) [0.1]

C-C breakage   TS4

H   H   H1
1.781   1.597
(2.002)   (1.774)
[1.889]   [1.705]
C2 —— C1 —— O
H2   H
<H1C1O = 92.3 (94.4) [94.7]
<OC1C2 = 174.6 (176.5) [176.4]
<OC1C2H2 = 22.0 (-3.5) [0.0]

C-C breakage   TS5

H
84.1
(80.4)
[85.2]
O
1.567 (1.521) [1.673]
H1
C2 —1.594— C1
(1.812)
[1.664]
H4   H2   H3
rC1H1 = 1.236 (1.146) [1.178]
rC1H2 = 1.111 (1.104) [1.083]
rC1H3 = 1.139 (1.099) [1.131]
<OC1H1 = 71.2 (77.1) [79.6]
<OC1H2 = 110.0 (126.7) [112.3]
<OC1H3 = 138.3 (121.7) [138.9]
<OC1C2H4 = -162.8 (177.4) [-165.3]

Figure 4-2 compares the transition state structures of our calculations with those from UMP2/cc-pVTZ *ab initio* calculations by Troya *et al.*[148(b)] The abstraction TS exhibits the typical near collinear O-H1-C1 arrangement (Please see the figure for notation), which is also found for many H atom abstraction reactions such as O(^3P) with hydrogen, methane and propane. Both the H elimination and C-C bond breakage reactions occur through two saddle point geometries. In one of them, the incoming oxygen atom is largely in a line with the carbon atom and the departing group, the H atom or the methyl radical, which can be described as an S_N2 mechanism. In the other, O adds onto carbon at a much more bent angle with the departing H or CH_3 group. As will be discussed later, the difference in the arrangement of the reactive groups affects mostly the angular distributions of the products in the scattering dynamics.

We also tabulate in Table 4-1 the reaction energies and energy barriers involved in the three reaction channels at different theory levels and compare them with the available experiments. Although the MSINDO reaction energies deviate greatly from what were obtained by the other methods, being much too exothermic, the barriers to reaction generally agree among all these methods, with abstraction being the lowest energy process and H elimination and C-C breakage having dissociation energies close to each other. B3LYP underestimates the abstraction barrier by ~5.5 kcal mol^{-1} as compared to an estimate based on experimental data,[148(b)] while the higher level *ab initio* calculations are very likely to overestimate the barrier heights for these processes. Both the H abstraction and C-C breakage channels have energy barriers of the magnitude of ~2

eV, thus eluding previous low energy experimental observations. Under LEO conditions,

these channels may compete with the low barrier H abstraction reaction, opening up new

mechanisms for material damage in LEO.

Table 4-1.   Energies of the stationary points associated with the O + C_2H_6 reactions[a,b]

Species	MSINDO[c]	B3LYP/6-31G**	CCSD(T)/cc-pVTZ[d]	MRCI+Q	expt
O(^3P)+C_2H_6	0	0	0	0	0
OH+C_2H_5	-18.9 (-13.6)	-0.3 (4.1)	0.97 (5.14)	-1.4 (2.7)[e]	-1.84[g]
H+C_2H_5O	-8.3 (-1.56)	7.7 (14.2)	14.0 (19.1)		8.3[g]
CH_3+CH_3O	-17.9 (-11.8)	-2.5 (1.74)	3.04 (7.9)	1.1 (6.3)[f]	-0.69[g]
TS1 (abstraction)	7.1 (11.8)	1.14 (5.5)	9.6 (13.2)	9.0 (13.0)[e]	6.6[h]
TS2(H elimination)	38.5 (43.3)	42.8 (46.4)	50.5 (53.7)		
TS3(H elimination)	37.1 (41.3)	47.7 (52.0)	56.66 (60.2)		
TS4(C-C breakage)	37.3 (39.0)	38.4 (40.9)	47.55 (49.26)	46.9 (50.2)[f]	
TS5(C-C breakage)	45.7 (49.4)	51.4 (53.0)	60.5 (63.5)		

[a] Energies are in kcal mol^{-1}

[b] Values in parentheses are classical energies. Energies obtained after correction for the Zero-point energies (plain values) can be compared with experiment.

[c] Note that the Zero-point energies reported in the MSINDO outputs are scaled so that they are significantly smaller than what would correspond to the actual curvature of the potential surface. We have used the actual values of the Zero-point energies as obtained from the MSINDO Hessian matrices.

[d] Values taken from ref. 148(b).

[e] MRCI+Q(8,8) calculations with complete basis set extrapolation using geometries obtained with CASPT2(10,10)/cc-pVTZ calculations.[152]

[f] MRCI+Q(4,4) calculations with complete basis set extrapolation using geometries obtained with CASPT2(8,8)/cc-pVTZ calculations.[152]

[g] ΔH_{298K} as obtained from the experimental heats of formation.[159]

[h] From the evaluation by Troya *et al*. in ref .148(b).

4.3.2 Reaction Dynamics Calculations

The electronic ground state reaction $O(^3P) + C_2H_6$ has been investigated with the QCT method in the scheme of direct dynamics electronic structure calculations where energy and forces are computed as the trajectory evolves on the MSINDO or B3LYP/6-31G** surface. All our calculations are based on the unrestricted wavefunctions. We employed the direct dynamics algorithm because this is the only realistic method currently available for exploring multiple-channel reactive systems at hyperthermal energies.[160]

Batches of 10,000 MSINDO trajectories were run at E_{coll} = 34.6, 60.0, 74.9 and 90.0 kcal mol^{-1}. For B3LYP, only 1,000 trajectories were calculated at E_{coll} = 60.0 and 90.0 kcal mol^{-1}, respectively, in consideration of the much higher computational cost. The fifth-order predictor, sixth-order corrector integration algorithm[54] was employed to propagate the equations of motion along the trajectory. Due to their poorer energy conservation property, the MSINDO trajectories were started at an initial center-of-mass separation of 12 a_0 and were stopped at approximately the same distance for the product pair. While for the initialization and completion of the B3LYP trajectories we used a value of 15 a_0. The integration time step was 5 a.u. (~0.12 fs) in the MSINDO calculations and 10.0 a.u. for B3LYP. The impact parameter was sampled between 0 and 7.5 a_0 for both surfaces. In analysis of the trajectory output, we discarded those trajectories whose initial and final total energy difference exceeded 2 kcal mol^{-1}, which amounted to 43 out of the total 10,000 trajectories run at E_{coll} = 90 kcal mol^{-1} on the

MSINDO surface. While there are no B3LYP trajectories violating this conservation criterion. The QCT trajectories were started with the C_2H_6 molecule in its ground vibrational and rotational states. Since we used classical mechanics, the products might have smaller energies than their Zero-point energies. In such cases, we "rounded up" the fragment's energy to the ZPE.

4.4 Results and Discussions

4.4.1 Inelastic Scattering

Figure 4-3. Center-of-mass translational energy distributions for the inelastic scattering of oxygen atoms from ethane. The dark blue line shows the "best fit" distribution derived through fitting the TOF and laboratory angular distributions via the forward convolution method. The green circles connected with the green line is the distribution obtained from MSINDO calculations at E_{coll} = 90 kcal mol^{-1}. The purple circles connected with the purple line is the distribution obtained from B3LYP calculations at E_{coll} = 90 kcal mol^{-1}.

Figure 4-4. Center-of-mass angular distributions for the inelastic scattering of oxygen atoms from ethane. The dark blue line shows the "best fit" distribution derived through fitting the TOF and laboratory angular distributions via the forward convolution method. The green circles connected with the green line is the distribution obtained from MSINDO calculations at E_{coll} = 90 kcal mol^{-1}. The purple circles connected with the purple line is the distribution obtained from B3LYP calculations at E_{coll} = 90 kcal mol^{-1}.
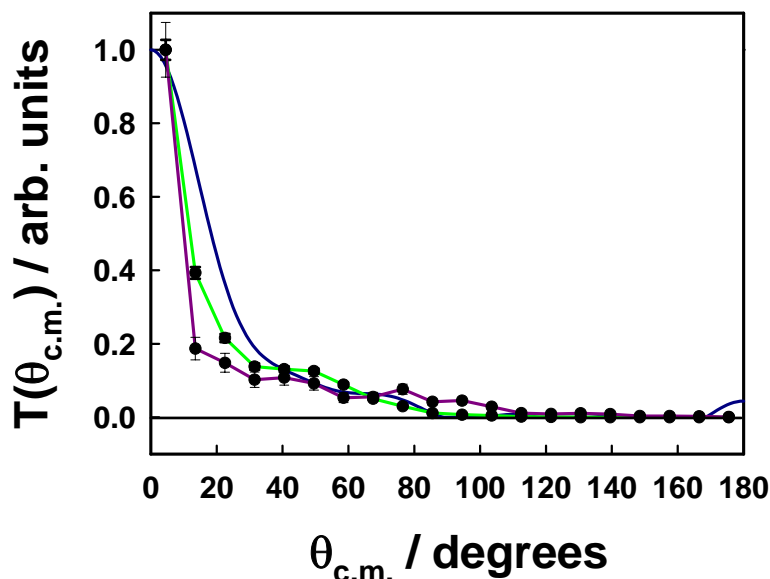
We begin by considering the inelastic scattering channel where no reactions have actually occurred. Shown in Figures 4-3 and 4-4 are the product translational energy distributions and angular distributions of oxygen atoms scattered from ethane at E_{coll} = 90 kcal mol^{-1}. The experimental translational energy distribution is very similar to results from direct dynamics calculations on the B3LYP/6-31G** and MSINDO potential surfaces, but the calculations have wider tails to lower energy than the experiment. [We should point out that in order to provide a better fit to the experiment, we discarded trajectories that had produced the C_2H_6 molecules with energies less than the ZPE in obtaining the theoretical translational energy as well as the center-of-mass angular

distributions.] Likewise, although the experimental and theoretical O atom angular distributions are very similar, the B3LYP distribution required a tail extending to more sideways angles than were seen in the experiment. [Note: the small bump rising at 170°in the experimental angular distribution is an artifact from forward convolution fitting process.] The general results of both experimental and theoretical translational energy and angular distributions are comparable, showing strong forward scattering of the oxygen atoms with very little energy transferred to the ethane collision partner. This observation is consistent with large impact parameter interactions.

At sideways and backward angles, however, a slowing of the signal was observed in both the experimental TOF distribution and the theoretical calculations (shown in Figure 4-5 are results calculated from the B3LYP trajectories), and was attributed to less probable, more severe, small impact parameter collisions between the O atoms and ethane. Such collisions can cause greater energy transfer between the two collision partners. Ethane molecules scattering from O atoms after small impact parameter collisions are much more internally excited and the system would thus have lower translational energy than what would be in the large impact parameter, O forward scattering collisions. Thus it seems that the majority of the oxygen atoms and ethane pass by each other at large impact parameters with little loss in translational energy; however, some collisions occur at smaller impact parameters in which no reaction occurs and the O atom rebounds from ethane in a sideways or backwards direction and experience a significant amount (>20%) of loss in translational energy. The energy not going into

translation following the small impact parameter collisions mostly goes towards excitation of the internal modes in the ethane molecule.

Figure 4-5. Center-of-mass translational energy distributions for oxygen atoms inelastically scattered from ethane into forward, sideways and backward ranges of angles as obtained from B3LYP calculations at E_{coll} = 90 kcal mol^{-1}. It is shown that as oxygen atoms are scattered into more backward directions, the translational energy distribution becomes broader and shifts towards smaller energies.
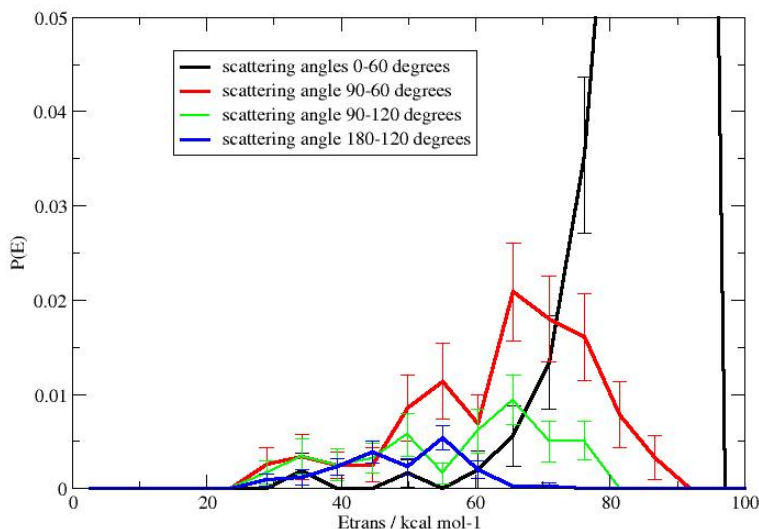
4.4.2 H-Atom Abstraction

The dynamical behaviors of this channel are in many respects similar to the inelastic scattering discussed above. The experimental translational energy distribution (Figure 4-6) seems to agree better with the B3LYP results, but the latter is much broader in the slower translation range. The MSINDO results predict a peak in the translational energy distribution which is ~10 kcal mol^{-1} lower than the experimental results, and is also much broader than what was observed for the simulated experimental fit. Figure 4-7

shows the experimental and calculated center-of-mass angular distributions for the

abstraction channel. The experimental and B3LYP distributions all peak at around 23˚,

but the B3LYP curve also shows strong intensities in the sideways angles. The MSINDO

distribution, though predominantly forward scattered, peaks at 40˚ and diminishes more

rapidly at sideways/backward angles than either the experimental or the B3LYP result.

Figure 4-6.   Center-of-mass translational energy distributions for OH following reaction of O(^3P) with ethane. The dark blue line shows the "best fit" distribution derived through fitting the TOF and laboratory angular distributions via the forward convolution method. The green circles connected with the green line is the distribution obtained from the MSINDO calculations at E_{coll} = 90 kcal mol^{-1}. The purple circles connected with the purple line is the distribution obtained from the B3LYP calculations at E_{coll} = 90 kcal mol^{-1}.
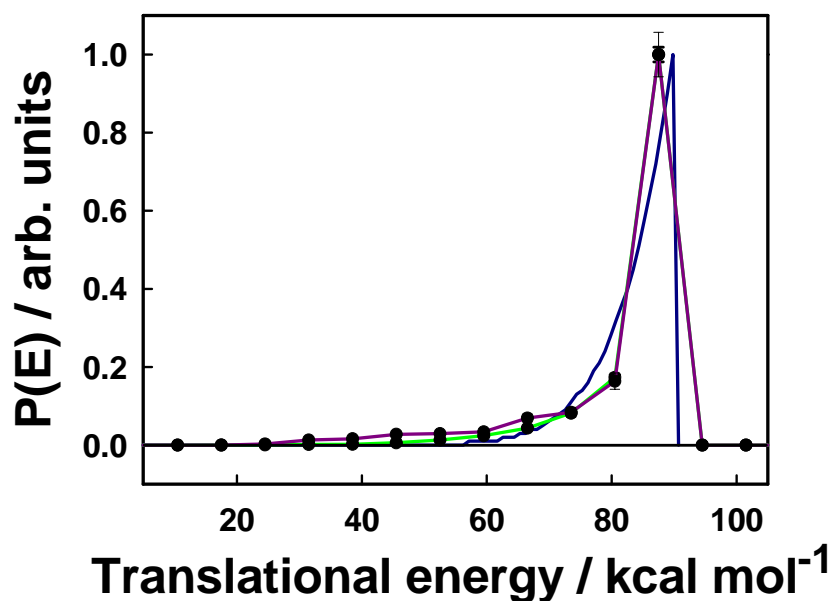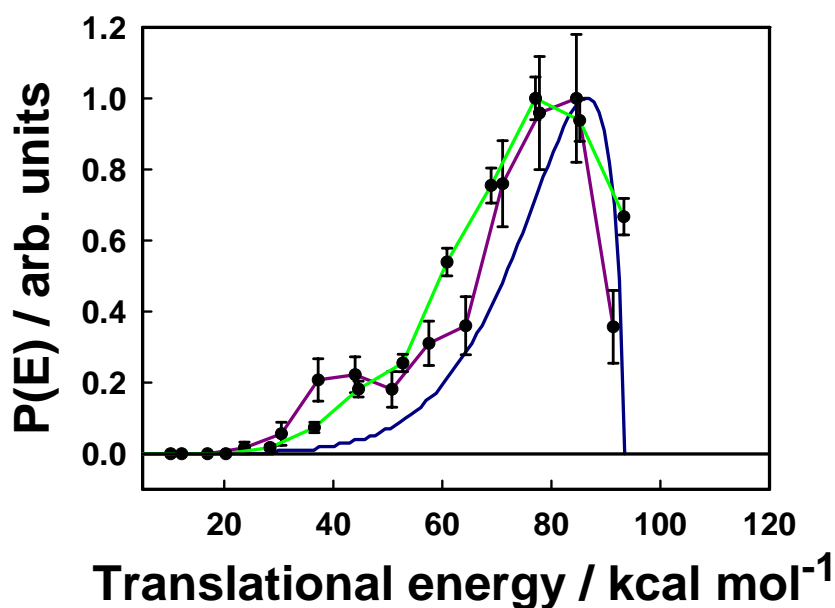
Figure 4-7. Center-of-mass angular distributions for OH following reaction of O(^3P) with ethane. The dark blue line shows the "best fit" distribution derived through fitting the TOF and laboratory angular distributions via the forward convolution method. The green circles connected with the green line is the distribution obtained from the MSINDO calculations at E_{coll} = 90 kcal mol^{-1}. The purple circles connected with the purple line is the distribution obtained from the B3LYP calculations at E_{coll} = 90 kcal mol^{-1}.
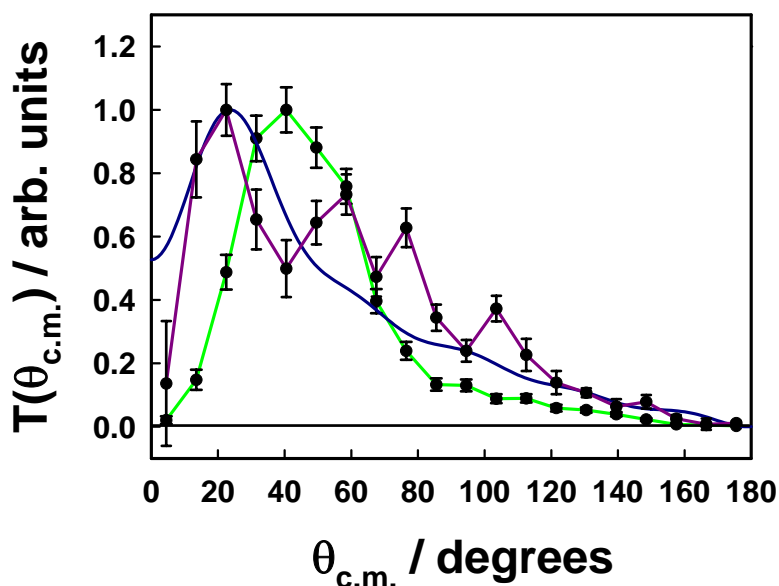
The general agreement between experiment and theory reveals the overall picture of the scattering dynamics for the abstraction reaction: The OH scattering is largely forward with some intensity extending out into sideways scattered angles. Very little translational energy is lost in the collisions (about 20% according to the B3LYP calculations), although there is more energy transferred than was observed for the inelastic scattering channel. The mass combination of the O (^3P) + C_2H_6 → OH + C_2H_5 reaction satisfies a heavy-light-heavy model, where the transferred atom is a light atom,

and there is a propensity for the system to conserve orbital angular momentum during reaction. It is thus expected that most of the translational energy stay intact after the collision, which is especially true for reactions occurring at large impact parameters. Examination of the impact parameter dependence of the energy partitioning mode reveals that, for large impact parameter reactive collisions (the average impact parameter = 4.2 a_0), about 92% of the available energy is channeled into translation, 1.6% to OH vibration, 5.9% to OH rotation, and 5.3% to C_2H_5 internal motion. While at small impact parameters (the average impact parameter = 1.8 a_0), the product pair appears with 61.6% of the available energy to translation, 4.6% to OH vibration, 8.6% to OH rotation, and 25.2% to C_2H_5 internal. [The above values are from the B3LYP trajectories calculated at E_{coll} = 90 kcal mol^{-1}.] It is noted that a significant amount of energy is deposited in the ethyl radical in those "head on" collisions (largely along the line of O-H1-C1). As was found for many other H-atom abstraction reactions, the OH scattering is narrowly forward peaked in collisions occurring at large impact parameters, indicative of a stripping mechanism, while broadens and moves to sideways/backward directions at smaller impact parameters, typical of a rebound mechanism.

The MSINDO rotational distributions for the diatomic molecule OH are significantly hotter than were predicted by the B3LYP trajectories. Such as at E_{coll} = 90 kcal mol^{-1}, the MSINDO OH rotational distribution for OH (v' = 0) peaks at j' = 20, while the corresponding B3LYP distribution peaks only at j' = 10. The fraction of the total

Figure 4-8.   Energy partitioning in product relative translation and product internal modes as a function of collision energy for the O (^3P) + C_2H_6 → OH + C_2H_5 reaction.
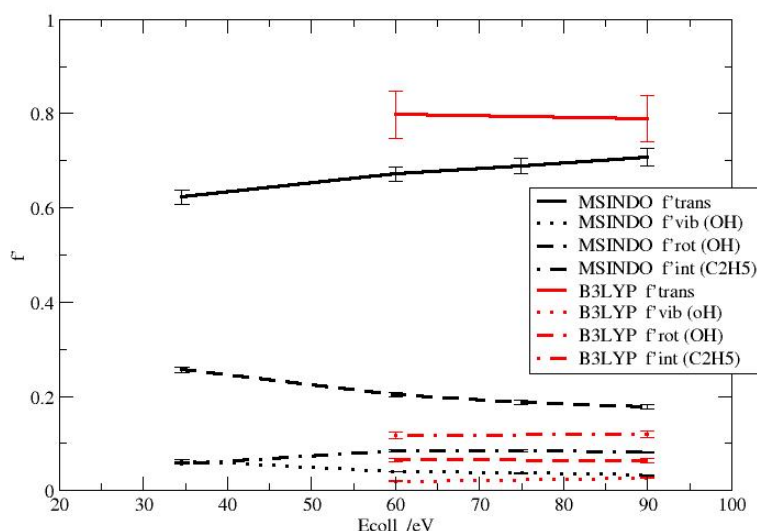
available energy into OH rotation by MSINDO is also much larger (18%) than by B3LYP calculations (6%). As for the energy disposal into product relative translation, OH vibration and ethyl radical internal motion, they are 71%, 3%, and 8%, respectively on the MSINDO surface, and 79%, 3% and 12%, respectively on B3LYP. As collision energy decreases from 90 kcal mol^{-1} to 34.6 kcal mol^{-1}, there are slight decreases of product translational energy fraction and C_2H_5 internal energy fraction and slight increases of OH rotational and vibrational energy fractions (Figure 4-8). So it is very likely that at energies close to abstraction barrier, MSINDO greatly overestimates both OH rotational and vibrational excitations as compared to previous low energy

experiment.[137] Whereas the B3LYP calculations, in which the OH rotational excitation is significantly colder and the ethyl radical internal excitation is hotter than by MSINDO calculations, seem to agree better with the experiment of ref. 137. The larger amount of OH rotational excitation on the MSINDO surface is due to a looser dependence of the MSINDO energy on the O-H1-C1 bending angle than was found in *ab initio* calculations such that the abstraction reaction is allowed to occur at configurations with more bent O-H1-C1 angles, leading to higher rotational excitation in OH. While the excess OH vibrational excitation, very likely by both MSINDO and B3LYP calculations, is the result of a deficiency associated with the QCT method, wherein the coupling between motion along and perpendicular to the reaction coordinate leads part of the reagent ZPE to end up as OH vibrational energy.[161]

We further examined the opacity functions for this channel at the four collision energies in our calculations, as shown for MSINDO in Figure 4-9. There is a clear trend of dropping-off of reactivity at smaller values of the impact parameter and enhancement of reactivity at large impact parameters as the collision energy increases. It is thus expected that the stripping mechanism dominated over the rebound mechanism in the hyperthermal O (^3P) collisions with ethane carried out in the current experiment. The gradual diminish of reactive events in the small impact parameter range is largely due to competition from the secondary channel H-atom elimination, the probability of which increases as soon as the system has enough energy to surmount the barrier (Figure 4-9b).

Figure 4-9. Opacity functions for (a) the O (^3P) + C_2H_6 → OH + C_2H_5 reaction and (b) the O (^3P) + C_2H_6 → H + C_2H_5O reaction at various collision energies.
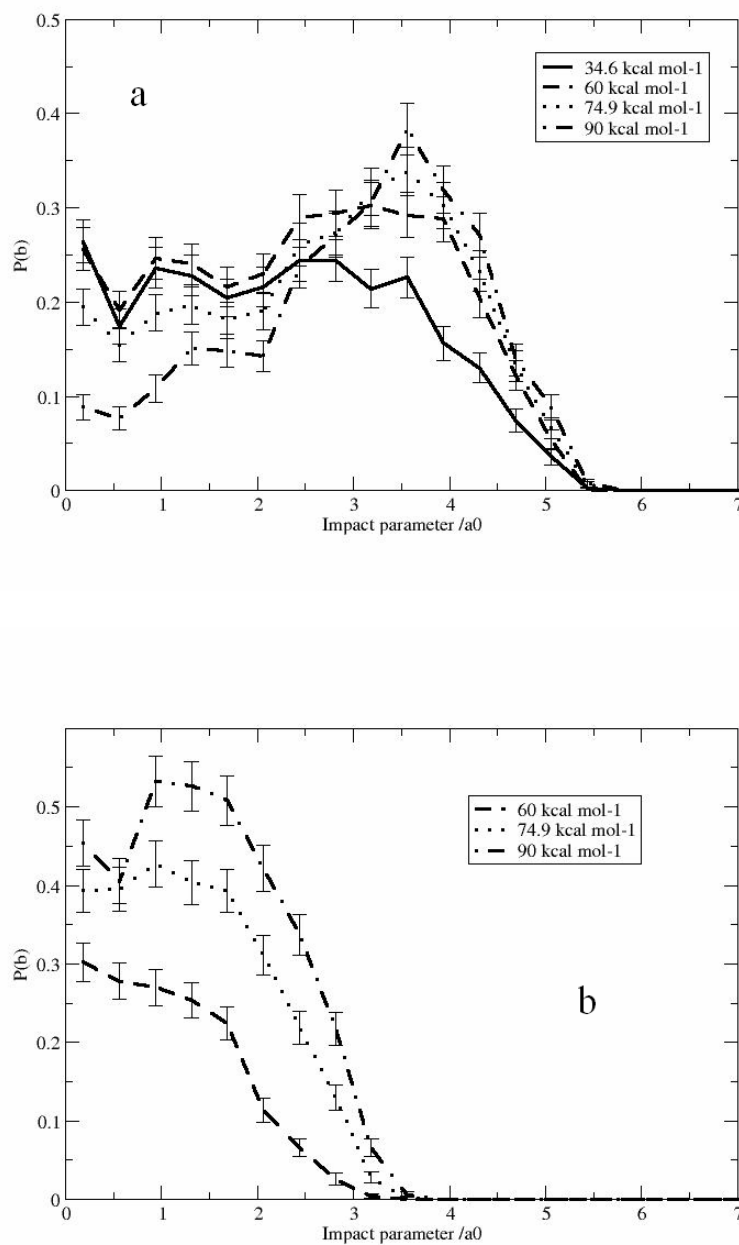
4.4.3 H-Atom Elimination

Experimentally, it is very difficult to obtain dynamical information for the H elimination channel because of the small center-of-mass recoil velocities of C_2H_5O; however, results that are qualitatively similar to MSINDO and B3LYP calculations have been achieved.

Figure 4-10. Center-of-mass translational energy distribution for C_2H_5O following reaction of $O(^3P)$ with ethane. The dark blue line shows the "best fit" distribution derived through fitting the TOF and laboratory angular distributions via the forward convolution method. The green circles connected with the green line is the distribution obtained from the MSINDO calculations at E_{coll} = 90 kcal mol^{-1}. The purple circles connected with the purple line is the distribution obtained from the B3LYP calculations at E_{coll} = 90 kcal mol^{-1}.
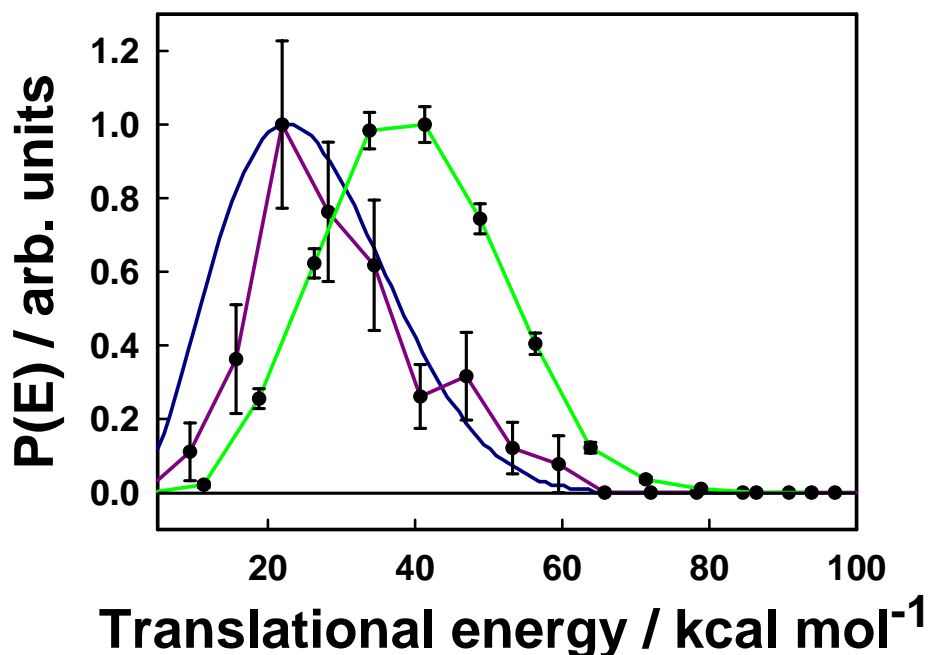
Figure 4-11.   Center-of-mass angular distribution for C_2H_5O following reaction of O (^3P) with ethane. The dark blue line shows the "best fit" distribution derived through fitting the TOF and laboratory angular distributions via the forward convolution method. The green circles connected with the green line is the distribution obtained from the MSINDO calculations at E_{coll} = 90 kcal mol^{-1}. The purple circles connected with the purple line is the distribution obtained from the B3LYP calculations at E_{coll} = 90 kcal mol^{-1}.
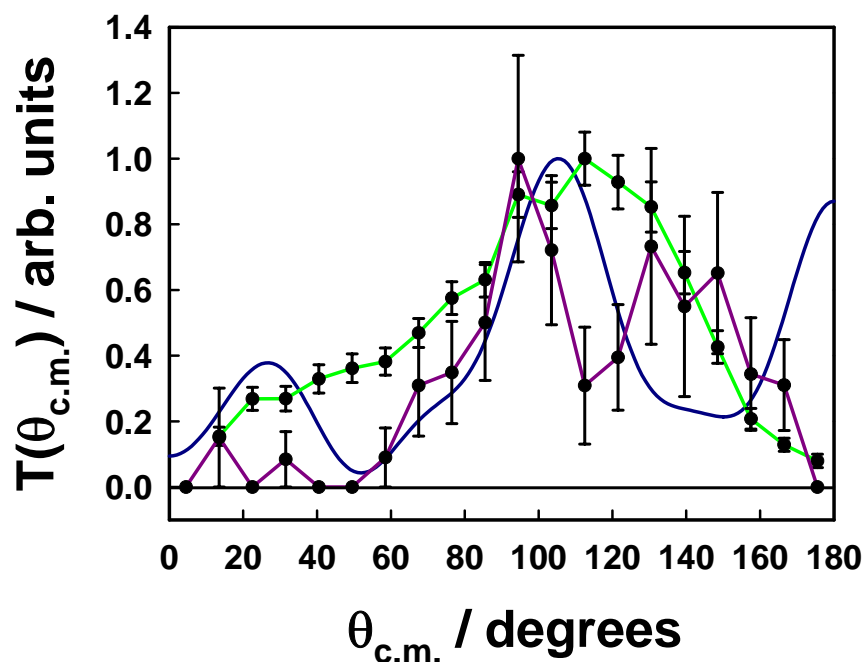
Shown in Figures 4-10 and 4-11 are the center-of-mass translational energy and angular distributions from experimental measurements and theoretical calculations. Though the experimental and B3LYP translational energy distributions agree reasonably, all peaking at around 22 kcal mol^{-1}, the MSINDO distribution shifts to higher energies. All distributions, however, show a large amount of energy transfer from translation to the internal modes of the ethoxy radical. The C_2H_5O angular distributions (Figure 4-11),

while sharing some similarities, seem to have quite different shapes. There are three distinct peaks, in the backward most, sideways and forward angles, respectively, in the experiment simulated distribution. The B3LYP distribution to some extent reproduces the three bumps in the backward, sideways and forward (the forward peak is much lower in intensity) directions, but does not coincide precisely with the experimental peak positions. Particularly, the backward peak by B3LYP appears around $130°$—$150°$ where the experimental signal is actually rather weak, instead of $180°$ as seen in experiment. The MSINDO distribution exhibits only one peak centered around $110°$ and is broad in both the forward and backward directions. Between theoretical and experimental results, a general picture of scattering for the O (^3P) + C_2H_6 → H + C_2H_5O reaction emerges wherein the ethoxy product is largely sideways- and backwards-scattered, with a relatively small amount of energy released in relative translation following the reactive collision.

The ethoxy channel is the major competing reaction pathway for H-atom abstraction in small impact parameter hyperthermal collisions. In sharp contrast to the energy disposal scheme found for the abstraction reaction, the majority of the initial relative translational energy is lost as internal energy of C_2H_5O, which amounts to 64% of the available energy based on the B3LYP calculations at 90 kcal mol^{-1} collision energy. The result is not surprising since the O (^3P) + C_2H_6 → H + C_2H_5O reaction can be categorized as a heavy-heavy-light class of kinematics where the departing atom is a light atom. The tendency, instead, is to convert the initial orbital angular momentum into

the angular momentum of the product molecule. The H-atom elimination reaction is found to proceed through two TS structures, TS2 and TS3 as shown in Figure 4-2. Although TS2 is energetically more favorable, a large majority of the trajectories react via the TS3 mechanism, as the bent O-C-H arrangement is sterically much more probable. We tried to differentiate between trajectories occurring through the two mechanisms, and found that the center-of-mass angular distributions demonstrated the expected trends: the TS2 trajectories led to more backward-scattered ethoxy product, with the H atom departing in the same direction as the incident O atom. The TS3 trajectories, on the other hand, resulted in more isotropic scattering with a strong favoring of the sideways direction (The average ethoxy scattering angles are 140° and 102° for the TS2 and TS3 trajectories, respectively, on the B3LYP surface at E_{coll} = 90 kcal mol^{-1}). The energy partitioning in the products, however, didn't seem to differ noticeably for the two mechanisms, with about 37% of the available energy ending up in translation, 63% in ethoxy internal modes, according to both the MSINDO and B3LYP calculations at 90 kcal mol^{-1}. Note that the fraction of the C_2H_5O internal energy becomes smaller at lower collision energies, but still is about half of the total energy at E_{coll} = 60 kcal mol^{-1}. Finally Figure 4-12 depicts the energy evolution of the angular distribution from the MSINDO trajectories. The two peaks in the backward and sideways angles are clear at relatively low collision energies, but merge to form a single peak as energy increases.

Figure 4-12. Angular distributions expressed as normalized differential cross sections for the O (^3P) + $C_2H_6 \rightarrow$ H + C_2H_5O reaction at various collision energies. Results are from the MSINDO QCT trajectories.
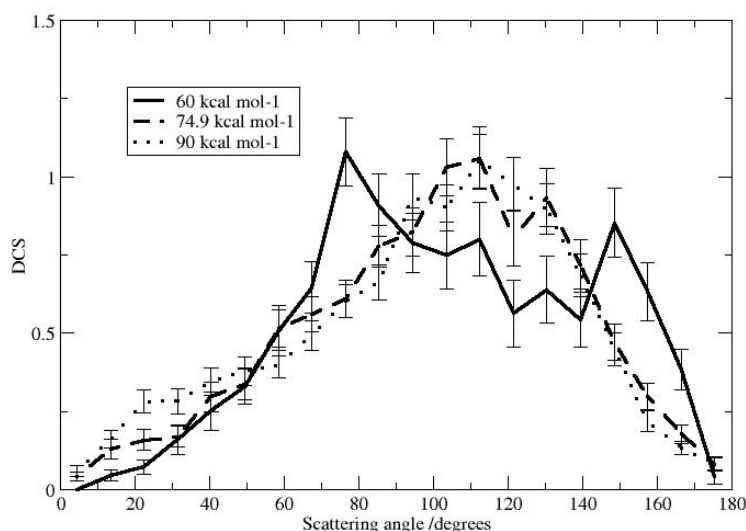
4.4.4 C-C Bond Breakage

This is the most elusive channel in the experimental study of the O (^3P) + ethane reaction, since there is no mass-to-charge ratio at which evidence for this channel appears without interference from other ionizer fragments. However, detailed analysis at one of the products ionizer fragments, m/z = 29 (HCO^+), reveals the existence and some dynamical information associated with the never-before-seen C–C bond breakage channel. The experiment simulated translational energy distribution for this channel is very slow, peaking around 30 kcal mol^{-1}, and the center-of-mass angular distribution is largely forward scattered with some intensity in the sideways direction. Current theoretical results, however, predict a dramatically different picture of the scattering

dynamics for this channel. Similar to the H elimination reaction, C-C bond breakage may occur through two different TS structures, corresponding to the S_N2 (TS4) and a much more bent O-C-CH_3 arrangement (TS5). Trajectory animation showed that the TS4 mechanism led to the methyl radical scattered largely along the incident O direction, while in the TS5 process, the methyl angular distribution was much broader and centered in the sideways directions. Shown in Figure 4-13 is the angular distribution for the co-product, CH_3O. The 60 kcal mol^{-1} distribution clearly shows the contributions from the two mechanisms, with TS4 responsible for scatterings in the more backward angles and TS5 for the broad, sideways scatterings. As energy increases, this difference is largely wiped off and the total distribution moves to sideways directions. Further inspection of the energy disposal in the products showed a trend similar to that of H abstraction: about 80% of the available energy goes to translation, 15% to CH_3O internal modes, and only a small amount to the CH_3 radical in the considered energy rang. Thus the theoretical translational energy distribution is much hotter than was obtained from experiment. There is thus a poor match between experiment and theory at this point.

Figure 4-13. Angular distributions expressed as normalized differential cross sections for the O (^3P) + $C_2H_6 \rightarrow CH_3$ + CH_3O reaction at various collision energies. Results are from the MSINDO QCT trajectories.
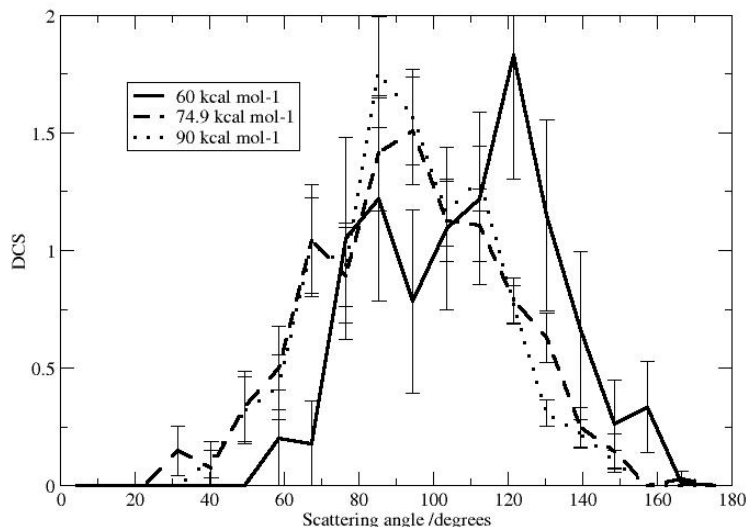
4.4.5 Excitation Functions

The most important reaction paths at the collision energies considered in the current experiment lead to the dissociation products OH + C_2H_5, H + C_2H_5O, and CH_3 + CH_3O, respectively. Figure 4-14 plots the reaction cross sections as a function of collision energy (known as the excitation function) for the three channels from the MSINDO and B3LYP/6-31G** trajectories. It is shown that the cross sections for the three channels all increase in the calculated energy range. The abstraction reaction, being the lowest barrier process, dominates over all other channels throughout the entire energy interval, but the increase of its cross section slows down at higher energies. On the other

hand, the H elimination cross section steadily increases from the threshold and becomes comparable in magnitude to the abstraction cross section at higher energies, according to the MSINDO calculations. This fast increase was predicted to continue up to 132.6 kcal mol^{-1} but the reactivity of H elimination is still secondary to the abstraction reaction.[148(b)] Although the activation barrier to C-C bond breakage is rather close to that of the H elimination channel, as shown in Table 4-1, the C-C breakage reaction cross section increases noticeably slower with collision energy. This discrepancy is expected since statistically the possibility of the methyl group being replaced (i.e., C-C breakage) is three times less than for the H atoms (i.e., H elimination) when O collides with one of the carbon atom in ethane.

Figure 4-14.   Excitation functions for the three major reaction pathways of O (^3P) + C_2H_6 under the experimental conditions. Results are given from both the MSINDO (plain curves) and the B3LYP/6-31G** (curves with filled circles) calculations.
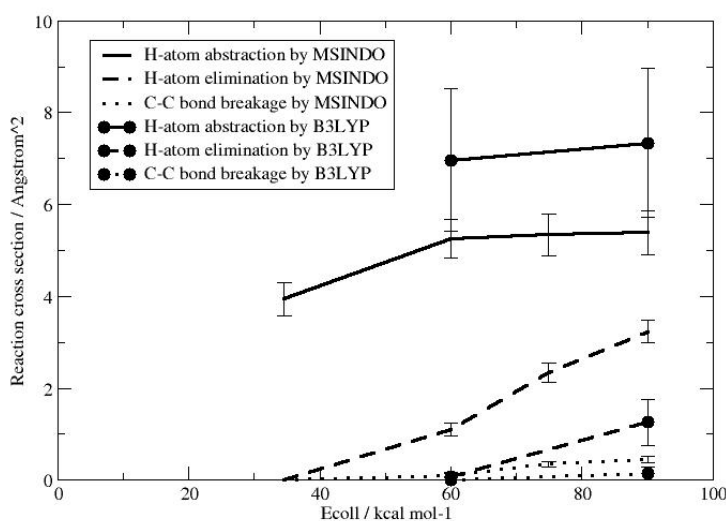
Comparing the MSINDO and B3LYP results, we note that there is a much larger cross section gap between the abstraction reaction and the other channels on the B3LYP than on the MSINDO surface. The very low energy barrier to abstraction predicted by B3LYP suggests an overestimation of reactivity for this channel on the B3LYP surface. This is evident in Table 4-2 where the experimental product yield for abstraction at 90 kcal mol^{-1} collision energy is not as high as was calculated from the B3LYP trajectories. On the other hand, the MSINDO cross sections for both H elimination and C-C bond breakage seem a little too high and the MSINDO excitation function for H atom elimination has to be shifted to higher energy in order to provide a fit to the experiment (see discussions below).

The experiment also measured the excitation function for the H elimination reaction by exploring five center-of-mass collision energies, E_{coll} = 69, 72, 80.4, 89, and 97 kcal mol^{-1}. Figure 4-15 compares the experimental and calculated excitation functions for the H elimination channel. The MSINDO results required a shift to higher energy of 25 kcal mol^{-1} to provide a fit to the B3LYP calculations and the experimental flux of the product in the considered collision energy range. This shift is not unreasonable because MSINDO was shown to underestimate the barriers for both H elimination and C–C bond breakage in O (^3P) + ethane (Table 4-1). Even though the current experiment was unable to reach collision energies lower than 69 kcal mol^{-1}, the measured excitation function as well as the B3LYP curve suggest that the threshold for H elimination appears around 60 kcal mol^{-1}, higher than the calculated activation barrier of about 50 kcal mol^{-1}.

Figure 4-15. Experimental and calculated excitation functions (cross section vs. collision energy) for the O (^3P) + C_2H_6 → C_2H_5O + H reaction. Experimental data collected at m/z = 43 ($C_2H_3O^+$) are shown as dark blue squares connected with a dark blue line. The green circles connected with a green line are the MSINDO calculated cross sections shifted to higher energy by 25 kcal mol^{-1}. The B3LYP calculated cross sections are shown as the purple hexagons connected with the purple line.
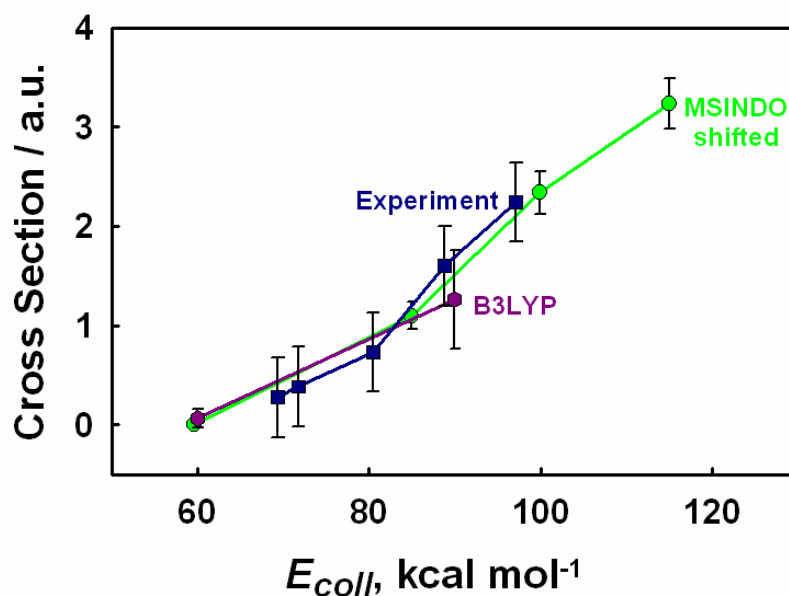
4.4.6 Relative Product Yields

We summarize in Table 4-2 the relative product yields for some prominent reaction pathways of the O (^3P) + C_2H_6 reaction that have been identified by our QCT calculations on the MSINDO and B3LYP surfaces and compare them with the experimental measurements at E_{coll} = 90 kcal mol^{-1}. Note that some minority products, such as $^2CH_3CH$ + H_2O and $^3CH_2CH_2$ + H_2O, CH_3CHO + 2H, CH_3 + CH_2O + H can also be produced as secondary reaction products of the primary reaction channels H-atom abstraction, H-atom elimination and C-C bond breakage.

Table 4-2. Theoretical relative cross sections (branching fractions) based on the MSINDO (plain values) and the B3LYP/6-31G** (values in parentheses) calculations for the major reaction pathways at various collision energies. Current experimental measurements are presented in brackets at 90 kcal mol^{-1} collision energies.

E_{coll}	34.6 kcal mol^{-1}	60 kcal mol^{-1}	74.9 kcal mol^{-1}	90 kcal mol^{-1}
Inelastic Scattering	92%	86.8% (85.2%)	83.3%	80.7% (81.6%) [85%]
OH+C_2H_5	7.9%	10.6% (13.9%)	10.7%	10.8% (14.7%) [10%]
H+C_2H_5O	0%	2.2% (0.13%)	4.7%	6.5% (2.5%) [4%]
CH_3+CH_3O	0%	0.2% (0.03%)	0.69%	0.9% (0.28%) [1%]
CH_3CHO+2H	0%	0.1% (0%)	0.3%	0.57% (0.08%)
CH_3+CH_2O+H	0%	0.01% (0%)	0.03%	0.1% (0.07%)
$^3CH_3CH$+H_2O	0.03%	0.1% (0.33%)	0.18%	0.27% (0.59%)
$^3CH_2CH_2$+H_2O	0%	0% (0.4%)	0%	0% (0.2%)
CH_3CHOH+H	0%	0.02% (0%)	0.07%	0.13% (0.01%)

4.5 Summary

This chapter presents experimental and theoretical studies of O (^3P) collisions with ground state ethane in the energy range of 30—100 kcal mol^{-1}. *Ab initio* calculations

of the primary reaction pathways of O (^3P) + C_2H_6 reveal that, in addition to the low barrier well studied H-atom abstraction, the higher energy reaction channels, H-atom elimination and C-C bond breakage, can also occur under hyperthermal collisions, thus providing important mechanisms for materials erosion of aircrafts in low Earth orbit. At a reagent collision energy of 90 kcal mol^{-1}, both theory and experiment find that H-atom abstraction accounts for over 10% of the overall product yields, followed by H-atom elimination (~4%) and C-C bond breakage (~1%). The remaining part is mostly O atom inelastic scattering, which is about 85%. Further examinations of the product translational energy and angular distributions in the center-of-mass frame for the inelastic scattering, H abstraction and H elimination channels provide clear pictures of the scattering dynamics associated with these channels. For the more elusive C-C bond breakage reaction, there is currently a poor match between theory and experiment as to energy and angular distributions of the products and future work is absolutely needed in this respect.

Chapter 5   Intersystem Crossing Effects in the O (^3P) + C$_2$H$_4$ Reaction

5.1 Introduction

In chapters 3 and 4, we studied the ground state reactions between an H or O atom and the simplest alkanes, CD$_4$ and C$_2$H$_6$, where dynamics on a single Born-Oppenheimer surface suffices to reproduce the essential experimental observations. In this chapter, by detailed examination of the dynamical properties associated with the triplet O and the shortest-chain unsaturated hydrocarbon, C$_2$H$_4$, reaction, we will see that the first singlet state contributes substantially to the product distributions, so that the singlet products account for over 50% of the total product yields at energies barely above the abstraction reaction activation barrier.

The reaction of triplet oxygen with ethylene has attracted much experimental and theoretical attention because it is one of the basic oxidative reactions in the combustion of many different hydrocarbon fuels.[162] This simplest O (^3P) + alkene reaction, however, demonstrates rather complex reaction mechanisms. The following reactions are the possible primary product channels:

$$O(^3P) + CH_2=CH_2 \rightarrow {}^2OH + {}^2CH_2CH \qquad \text{(R1)}$$

$$O(^3P) + CH_2=CH_2 \rightarrow \bullet CH_2CH_2O\bullet \rightarrow {}^2H + {}^2CH_2CHO \qquad \text{(R2)}$$

$$\rightarrow {}^3CH_2 + CH_2O \qquad \text{(R3)}$$

$$\rightarrow {}^2CH_3 + {}^2CHO \qquad \text{(R4)}$$

$$\rightarrow {}^2H + {}^2CH_3CO \qquad \text{(R5)}$$

$$\rightarrow H_2 + CH_2CO \qquad \text{(R6)}$$

$$\rightarrow CO + CH_4 \qquad \text{(R7)}$$
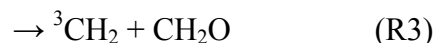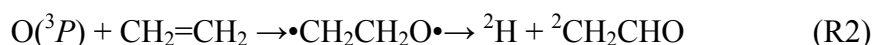
Past work has proposed[163] that the electrophilic oxygen atom attacks the C=C bond and forms an energetic triplet biradical $\bullet CH_2CH_2O\bullet$. The triplet biradical then undergoes

fragmentation and rearrangement, which competes with intersystem crossing (ISC) to give the corresponding singlet biradical. Product branching in the thermal O + ethylene reaction has been a much disputed topic in the experimental chemical dynamics community,[164] but the general agreement is that the hydrogen—vinoxy (H + CH$_2$CHO) and the methyl—formyl (CH$_3$ + CHO) channels account for up to 90% of the products. While the first of these products can be produced via dissociation of the triplet biradical,

the second is usually thought of as being the result of ISC followed by 1, 2-hydrogen migration to give a singlet acetaldehyde (CH_3CHO) intermediate which subsequently dissociates. The observation that the rate of the two major channels is similar suggests that dissociation of the biradical and ISC are of comparable importance. Note that there is no evidence for the occurrence of reaction channel R7 in any of the experimental measurements, even though this is the most exothermic product.

Theoretical studies of the reaction $O(^3P) + C_2H_4$ have largely been confined to quantum chemical calculations of the stationary points and energetics along the reaction pathways. Earlier work was concentrated on the characterization of the initial oxygen atom addition step.[165-167] It was shown that the reaction path corresponds to an asymmetric approach of O towards one of the carbon atoms of the olefin double bond. Nondynamical correlation effects had to be included to properly describe the electronic structure of the system and a barrier height of 4.7 kcal mol^{-1} was found at the multireference configuration interaction (MRD-CI) level,[167] higher than the experimental activation energy of about 2 kcal mol^{-1}.[168] Several groups calculated various triplet and singlet states of the CH_2CH_2O biradical[166, 169, 170] using either spin-restricted or spin-unrestricted Hartree-Fock formalism. The relative stability of the different biradical states varies in these calculations, but the small energy splitting of the triplet and singlet states supports the assumption that ISC is an important mechanism behind the title reaction.

There have been a number of theoretical efforts aimed at elucidating the reaction mechanisms on the triplet surface.[170-172] According to the generally accepted picture the O (^3P) + C$_2$H$_4$ → ^{3}CH$_2$CH$_2$O → H + CH$_2$CHO /CH$_2$ + CH$_2$O reactions (R2 and R3) are the energetically most accessible, with the direct H abstraction (R1) and the adduct ^{3}CH$_2$CH$_2$O isomerization pathways involving higher activation barriers. Reactions on the singlet surface involve facile rearrangement of the singlet biradical ^{1}CH$_2$CH$_2$O to several low-lying intermediate complexes including acetaldehyde, oxirane (*c*-C$_2$H$_4$O, ethylene oxide) and vinyl alcohol (CH$_2$CHOH), followed by interchange among these isomers and decomposition reactions to give CH$_3$ + CHO, H$_2$ + CH$_2$CO, CH$_4$ + CO, etc.[170, 173, 174] Although CH$_3$ + CHO products can come from both singlet and triplet pathways, the ISC pathway has generally been assumed to be dominant.

A more comprehensive investigation of both the triplet and singlet potential surfaces was recently carried out by Nguyen et al.[175] at relatively high levels of theory including G3, CBS-QB3, G2M, and MR-CI. Using a ratio of 45:55 for total triplet to total singlet product formation rate that was inferred from the experimental kinetics and crossed beam data, they computed product distributions and thermal rate constants for the title reaction and achieved overall good agreement with the experimental product branching ratios.

Wherever possible, a dynamics description is desirable for providing a quantitative determination of the reaction mechanism, the product branching, and for visualization of chemical processes, in particular, when multiple electronic states are

involved. However, dynamical simulations of nonadiabatic processes face severe obstacles, including the determination of multiple surfaces and their couplings, and describing the nuclear motion subject to these surfaces. For a multidimensional system with many degrees of freedom like O + ethylene, the traditional strategy of first generating analytical potential energy surfaces (PES) and coupling surfaces[176] is very difficult and has not, so far, been done. As an alternative to this, in the present study we have used direct dynamics quasiclassical trajectory calculations with trajectory surface hopping (TSH) to describe ISC. We used a simplified version of the TSH method wherein only gradients for the currently occupied surface are computed as the trajectory evolves, and hops are only allowed when crossings between the singlet and triplet surfaces are encountered. Both singlet and triplet energies are determined using the unrestricted B3LYP/6-31G(d,p) electronic structure method. Whenever a triplet─singlet (T─S) surface crossing is detected during the trajectory propagation, a decision to hop is made based on the Landau-Zener transition probability formula. Comparison with the recent crossed molecular beam experiment of Casavecchia et al.[164] shows reasonable agreement as to the product distributions. Our calculations also provide a prediction of the dynamical behavior at hyperthermal energies well above the reaction barriers.

The present TSH method is most similar to one described long ago by Stine and Muckerman.[177] Neglect of hops away from crossings is physically justified because of the smallness of the spin-orbit coupling matrix elements (typically <100 cm^{-1}) compared to the singlet/triplet energy differences (typically >1000 cm^{-1}). In contrast to some of the

more recent methods, such as the Tully's Fewest Switches method,[62] where the electronic Schrödinger equation is integrated on the fly while the trajectory evolves, the present method avoids the extra machinery and smaller time steps to do this, a simplification that is absolutely necessary to make the calculations feasible given the computational effort associated with the direct dynamics calculations. Other methods, such as the Ehrenfest method,[64-70] provide another alternative for describing nonadiabatic dynamics in which the dynamics is evolved on an effective average electronic state. This would not be useful here as there are many possible products, and the time scales for reaction vary from <1ps to >1μs.

Most of our calculations have considered an initial kinetic energy of 0.56 eV so as to match the conditions used in the Casavecchia experiments. We have also examined the O (^3P) + C_2H_4 reaction dynamics at a hyperthermal collision energy of 3.0 eV. Collisions in the hyperthermal regime are of interest for understanding material erosion of space vehicles traveling in low-Earth orbit (LEO), where the ambient oxygen atoms, and other reactive species, can collide with the vehicle surface at relative translational energies on the order of several eV. Often the vehicle surfaces include polymeric components (as in thermal blankets) so the present work provides a model system for studying the importance of both singlet and triplet reaction mechanisms in degrading unsaturated hydrocarbon polymers. In addition, O + C_2H_4 is relevant to reactions of atomic oxygen with outgassed unsaturated hydrocarbons in LEO.

5.2 Computational Details

5.2.1 Electronic Structure Calculations

The direct dynamics calculations were made by interfacing the Q-Chem computer program[123] with a molecular dynamics code so that at each point of the trajectory, the potential energy and/or gradients of the triplet and singlet ground electronic states were evaluated using the B3LYP[122] density functional theory method with a 6-31G(d, p) basis set. For calculations on both surfaces, we used spin unrestricted wave functions.

In order to assess the quality of the UB3LYP/6-31G(d,p) surfaces, we carried out geometry optimizations for the stationary points along major reaction pathways. Harmonic vibration frequencies and ZPEs were computed at the same theory level. The optimized structures are characterized as transition states if only one imaginary frequency exists, or as minima if all nonzero frequencies are real. Intrinsic reaction coordinate (IRC) calculations were performed to make sure the TSs connect the expected minima on the potential surfaces. For a proper description of the biradical nature of $\cdot CH_2CH_2O\cdot$ in the singlet state, where the unpaired alpha and beta electrons are separated on the terminal carbon and oxygen atoms, a multiconfiguration wave function, such as the CASSCF method, should be used. However, by forcing an unrestricted SCF procedure on the open-shell singlet biradical and the transition states that connect to it, we obtain reasonable results with single configuration calculations. To enforce spin polarization we

added 20% of the alpha LUMO to the alpha HOMO to break the alpha-beta symmetry in the initial guess of MOs.

The magnitude of the spin-orbit coupling (SOC) is small compared to the energy difference between the surfaces for most geometries. Thus the only significant T—S transitions occur when the surfaces are very close to a crossing. To simplify our dynamical simulations, surface hops are allowed only at points where the triplet and singlet surfaces cross. Furthermore, we did not actually calculate the spin-orbit matrix elements at each crossing point of each trajectory; instead, we used a constant value for the SOC throughout our calculations. This approximation is crude but justified if the large majority of T—S crossings occur in the vicinity of the CH_2CH_2O biradical (as is the case at low energies) where the SOC matrix elements do not vary much with geometry.[178] To verify this, we calculated the spin-orbit matrix elements at selected crossing point geometries detected in sample trajectories using the Breit-Pauli method as implemented by Fedorov and Gordon[179] in GAMESS.[126] The orbitals were generated from a twelve-state state averaged CASSCF calculation using an aug-cc-pVDZ one electron basis set.[180] Eight electrons in eight active orbitals were included in the CASSCF. We found that the states that are close in energy and thus are actively involved in ISC processes are the first 6 triplet states 1^3A ($M_s = 0, \pm1$), 2^3A ($M_s = 0, \pm1$), and the first 2 singlet states 1^1A ($M_s = 0$), 2^1A ($M_s = 0$). The spin-orbit matrix elements between the singlet and the triplet states are complex numbers. Following a procedure proposed by

Hoffmann and Schatz,[176(a)] we combine the three components of a triplet to form symmetry-adapted triplet wavefunctions, i.e.,

$$^3\Psi_z = i\ ^3\Psi\left(M_s = 0\right) \tag{5-1}$$

$$^3\Psi_x = \frac{1}{\sqrt{2}}\left[^3\Psi\left(M_s = 1\right) + ^3\Psi\left(M_s = -1\right)\right] \tag{5-2}$$

$$^3\Psi_y = \frac{i}{\sqrt{2}}\left[^3\Psi\left(M_s = 1\right) - ^3\Psi\left(M_s = -1\right)\right] \tag{5-3}$$

In this new representation, the matrix elements $<^1\Psi|H_{SO}|^3\Psi>$ are all real, ranging from 0 to 70 cm^{-1}. Through close inspection of the SOC matrix, we found that the triplet wavefunctions can further be linearly combined so that the first singlet state 1^1A only strongly couples to three of the six triplet states, while the second singlet 2^1A couples to the other three triplets. From this observation, we decided to calculate an average SOC between the singlet and triplet states by summing up the squares of the 12 singlet—triplet coupling elements and dividing the sum by 6 (where 6 is the number of nonzero matrix elements after the decoupling):

$$V_{13} = \sqrt{\left[\sum_{i=1}^{2}\sum_{j=x,y,z}\left|\left\langle 1^1\Psi\left|H_{SO}\right|i^3\Psi_j\right\rangle\right|^2 + \sum_{i=1}^{2}\sum_{j=x,y,z}\left|\left\langle 2^1\Psi\left|H_{SO}\right|i^3\Psi_j\right\rangle\right|^2\right]\Big/6} \tag{5-4}$$

Calculations at six different crossing point geometries give an average SOC around 35 cm^{-1}. Rather than use this value, we decided to generate results for several different choices of the SOC. In the first set of results to be presented, we used a high value of 70 cm^{-1}, and not surprisingly this leads to excess singlet formation. In later results we considered 50 and 30 cm^{-1} for the SOC to assess sensitivity of the results to the

value of the coupling parameter, and to determine if errors in the TSH method lead to deviations between the SOC that produces the best match with experiment and the SOC that is obtained from the CASSCF calculations.

5.2.2 Direct Dynamics Calculations

To study ISC effects in the O (^3P) + C_2H_4 reaction, we have used the direct dynamics quasiclassical variant of the TSH method where the potential is calculated on the fly with density functional theory. The trajectories are initiated on the ground triplet electronic state at a reagent collision energy of 0.56 eV, in order to match the conditions of the crossed molecular beam (CMB) study of Casavecchia and coworkers,[164] or of 3 eV, to simulate LEO collisions. Initially the classical mechanical equations of motion use energy and gradients from the triplet surface, but the singlet surface energy is also calculated and the singlet-triplet gap is evaluated to identify crossings. When the singlet surface intersects the triplet surface, we compute a transition probability using the Landau-Zener (LZ) formula:

$$P_{LZ} = 1 - \exp\left[-\frac{2\pi V_{13}^2}{\hbar \dot{Z} \left| \dfrac{dE_1}{dR} - \dfrac{dE_3}{dR} \right|} \right] \qquad (5\text{-}5)$$

where V_{13} is the SOC between the two surfaces, $\dot{Z}$ is the nuclear coordinate velocity perpendicular to the crossing seam, and $\left| \dfrac{dE_1}{dR} - \dfrac{dE_3}{dR} \right|$ is the magnitude of the difference between the singlet and triplet energy slopes at the crossing point. These slopes are determined by interpolating the gradients of the singlet and triplet surfaces, respectively,

to the crossing location, using values obtained from time steps just before and just after the crossing. Thus it is only at crossing points that gradient information is required on both surfaces. We could have used the Zhu-Nakamura (ZN) expression[181] instead of Eq. (5-5), however for the present application, the available energy is well above the crossing seam so the LZ and ZN probabilities are essentially the same.

Once the LZ probability is calculated, it is then compared with a random number ζ between 0 and 1 to decide if a surface hop should occur. If $P_{LZ} > \zeta$, the electronic state is switched from triplet to singlet and the trajectory is reinitiated on the singlet surface. No momentum adjustment has to be made on the new surface since hopping only occurs at the point of intersection where $E_1 = E_3$. If $P_{LZ} < \zeta$, the trajectory continues on the triplet surface. The treatment of a switch from the singlet to the triplet state follows exactly the steps described above. No attempt is made to restrict the frequency of successive hops.

One additional aspect in our treatment of nonadiabatic transitions concerns hops in the product asymptotic region. For the products H (^{2}S) + CH$_2$CHO (^{2}A″), H (^{2}S) + CH$_3$CO (^{2}A′), CH$_3$ (^{2}A$_2$″) + CHO (^{2}A′), the triplet and singlet surfaces are coincident with each other asymptotically. Hops in these regions occur, but are of no consequence since the two surfaces are identical. To remove this unnecessary hopping, we set P_{LZ} equal to zero at crossing points where the products are well separated. More precisely, for a C-H separation of about $3.5\,a_0$ or a C-C separation of about $4.8\,a_0$ the two surfaces are

nearly degenerate for these dissociation channels, so we cut off asymptotic hopping beyond these values.

Other features of the direct dynamics algorithm using TSH follow our previous work.[120] The polyatomic reactant C_2H_4 is prepared in its ground electronic and rovibrational state by running an intramolecular trajectory starting from the equilibrium geometry of C_2H_4 with kinetic energy of each normal mode made equal to the corresponding ZPE. This trajectory is integrated for many vibrational periods. The phase of the vibration motion is then sampled from this trajectory and the attacking oxygen atom is randomly placed around the vibrating C_2H_4 molecule with an initial center-of-mass distance of $14\,a_0$, a maximum sampled impact parameter of $10\,a_0$, and a reagent relative translational energy of 0.56 eV. The standard fifth-order predictor, sixth-order corrector integration algorithm is employed to propagate Hamilton's equations of motion along the trajectory with an integration time step of 10 a.u. (0.24 fs). The trajectory is terminated if the product pair is sufficiently separated (15-$17\,a_0$) or a maximum integration step is reached. Upon completion of the trajectory propagation, a final analysis is performed to derive various dynamical properties of the products. Specifically the reactive cross section for channel i is computed as

$$\sigma_i = \frac{2\pi b_{max}^2}{N} \sum_{k=1}^{N} x_k P_{ik} \tag{5-6}$$

in which $x_k = b_k/b_{max}$ with b_k being the impact parameter of trajectory k and b_{max} being the maximum sampled impact parameter, N is the total number of trajectories

and P_{ik} is the reaction probability of trajectory k. P_{ik} is 1 if the trajectory yields channel i and 0 otherwise.

5.3 Results and Discussions

5.3.1 Potential Energy Surfaces

Shown in Figure 5-1 are the computed triplet and singlet energies for the important stationary points, relative to the energy of $O(^3P) + C_2H_4$, inclusive of zero-point energies. The B3LYP/6-31G** values are compared with the values reported by Nguyen et al.,[175] for which they averaged the results of their G2M, CBS-QB3 and G3 calculations. While the energies of the dissociation products and of the low-lying intermediates on the singlet surface agree well between the two calculations, the B3LYP values at the other stationary points are generally lower by up to 8 kcal mol^{-1} than the higher level results. This discrepancy is especially prominent for the saddle points and reaction intermediates on the triplet surface. For example, for the CH_2CH_2O biradical, the triplet and singlet state relative energies are -30.4 and -33.7 kcal mol^{-1}, respectively on the B3LYP surface, but -24.0 and -25.9 kcal mol^{-1}, respectively, according to the CASSCF(8,8) + MR-CISD+Q method.[175] However, the relative significance of the primary reaction pathways is largely preserved on the B3LYP surfaces so that isomerization of triplet CH_2CH_2O is still unfavorable compared to decomposition.

Figure 5-1.   Potential energy profiles on (a) the triplet surface and (b) the singlet surface calculated using UB3LYP/6-31G (d, p). The values in brackets are higher quality theory calculations (the average of the values computed at the G3, CBS-QB3, and G2M levels) taken from figures 1 and 3 in reference 175.
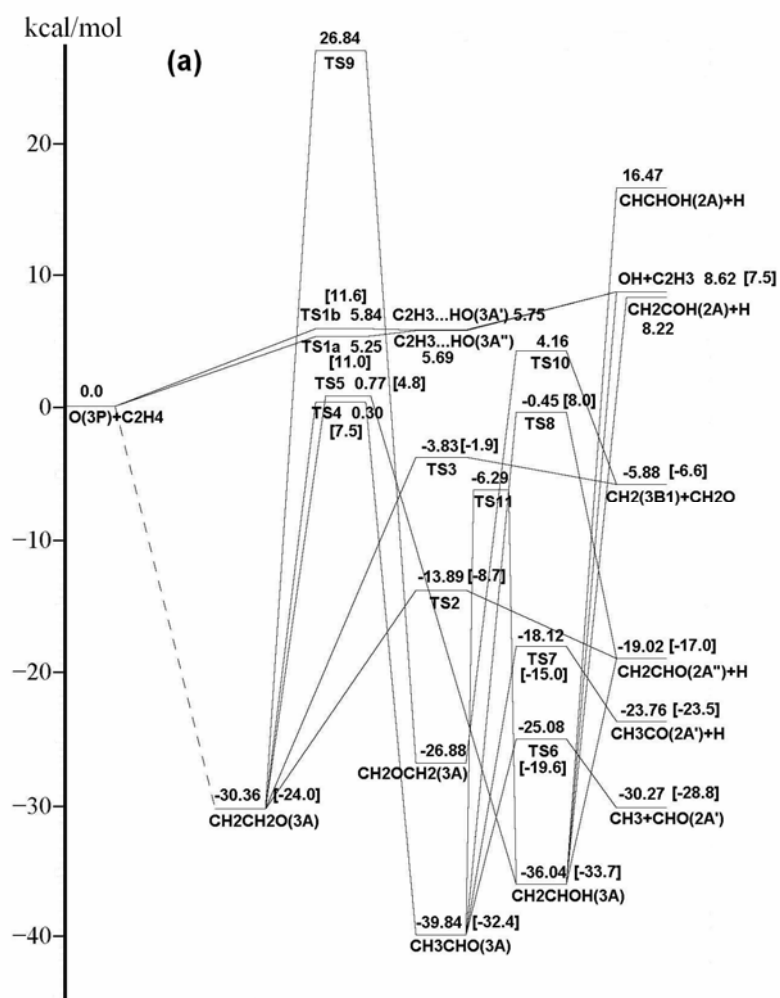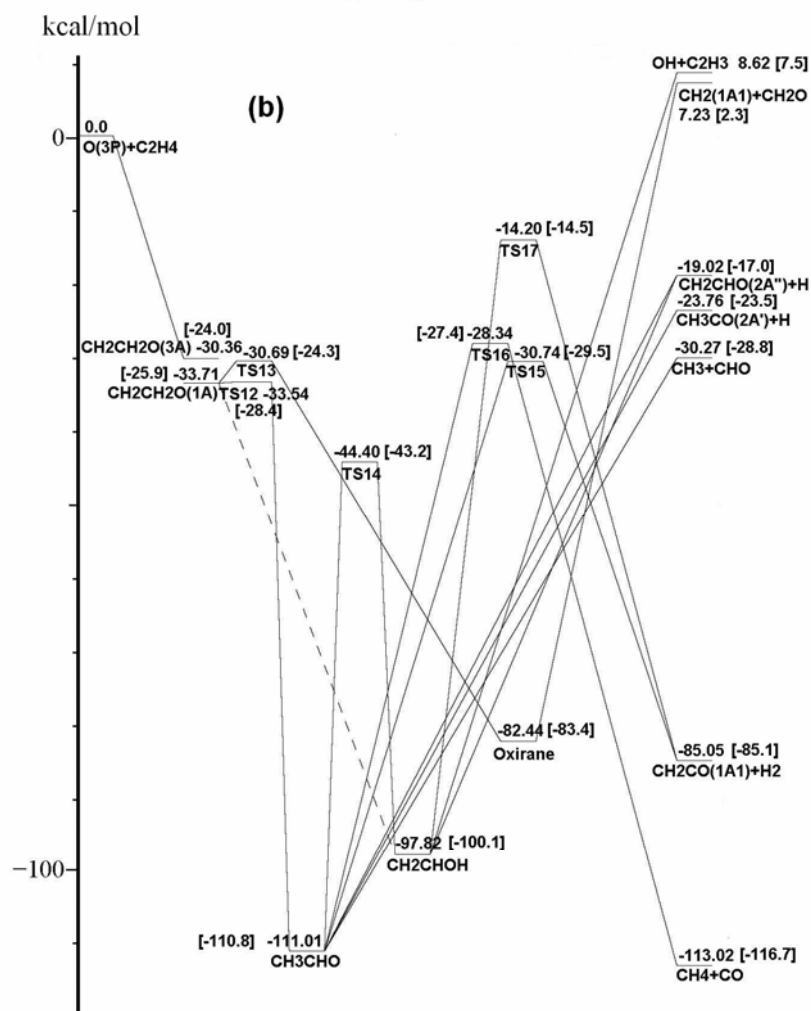
The direct H abstraction by O (^{3}P) to form OH and C_2H_3 is the only primary channel that proceeds without going through the O addition intermediate. As noted by Nguyen and coworkers, there are two similar transition states (TS1a is of ^{3}A″ symmetry,

and TS1b is of $^3A'$ symmetry) involved in H abstraction. Their relative energies, however, are only 5-6 kcal mol^{-1} in our B3LYP/6-31G (d, p) calculations, even lower than that of the product OH + C_2H_3 (8.6 kcal mol^{-1}). This suggests the existence of a post-TS weakly-bonded complex formed between C_2H_3 and OH moieties on the B3LYP surface. Indeed TS1a and TS1b correlate with two hydrogen-bonded CH_2=CH…HO complexes of $^3A''$ and $^3A'$ symmetry, respectively. Though the ZPE-inclusive energies of the complexes are somewhat higher than their corresponding TSs, the classical energy curves (before ZPE correction) do show a drop from the TSs to the hydrogen-bonded complexes. In any event, the formation of OH + C_2H_3 is not important in the crossed-beam experiments of Casavecchia et al., so this defect in the potential surface is of minor significance to our reaction dynamics studies.

The large majority of reactions occur through the formation of the CH_2CH_2O biradical. We were unable to locate a saddle point to O addition on the B3LYP surface, and it is very likely that there is no barrier on the B3LYP PES. The recommended thermal rate coefficient has an activation energy of only 2 kcal mol^{-1},[168] so the error caused by the lack of a barrier is again a minor issue to this work. The CH_2CH_2O biradical may exist in either the triplet or the singlet state. Our unrestricted B3LYP calculations locate the singlet biradical ~3.3 kcal mol^{-1} below the triplet state. Thus the S—T crossing can occur during the formation of the CH_2CH_2O biradical, or at any time thereafter until it dissociates. Figure 5-2 depicts the minimum energy path as the triplet oxygen approaches one of the carbon atoms, along with the singlet energies calculated at

the optimized triplet geometries. In contrast to the analogous curves that have been constructed using multireference perturbation theory (CASPT2, Figure 2 of ref. 175), the energy barrier to O addition is barely seen on the B3LYP surface. However, what is common is that the triplet and singlet curves are very close over a wide range of C-O distances (1.3-1.7 Å) in the biradical region. This means that there are numerous singlet-triplet surface crossings after the biradical complex is formed, so even though the crossing probability for each hop is typically quite small, the overall ISC probability for a long-lived intermediate can be quite large.

After the initial formation of the triplet CH_2CH_2O complex, it may subsequently isomerize to CH_3CHO (^3A), CH_2CHOH (^3A), and CH_2OCH_2 (^3A) through relatively high barriers, followed by further decomposition. The energetically more accessible pathways for CH_2CH_2O are dissociation via TS2 and TS3 to produce $H + CH_2CHO$ ($^2A''$) and $CH_2O + CH_2$ ($^3B_1$), respectively. Note that barriers TS4 and TS5 corresponding to 1,2-H atom transfer to the C and O atoms, respectively, are not as high as predicted at the G2M, CBS-QB3 and G3 levels. However, they are close to the energy of the reactants on the B3LYP surface, and thus are not particularly accessible under conditions which mimic the Casavecchia et al. experiment.

Reactions on the singlet surface start from CH_2CH_2O (^1A). By surmounting very small barriers, CH_2CH_2O rearranges to form three low-lying intermediate complexes, CH_3CHO ($^1A'$), CH_2CHOH ($^1A'$) and the three-member ring isomer, oxirane ($^1A_1$). B3LYP failed to locate the TS leading to vinyl alcohol. There is also the possibility of

direct H_2 elimination from $^1CH_2CH_2O$ to yield H_2 and ketene. This process was observed as a minor pathway in our dynamics calculations, but the corresponding saddle point on the PES has never been found.

Figure 5-2. Crossing seam of the triplet and singlet potential energy surfaces as O (^3P) attacks one of the carbon atoms in ethylene to form the triplet adduct CH_2CH_2O. The triplet curve corresponds to constrained optimization at fixed C-O distances on the triplet surface. The singlet energies are calculated at the triplet optimized geometries.
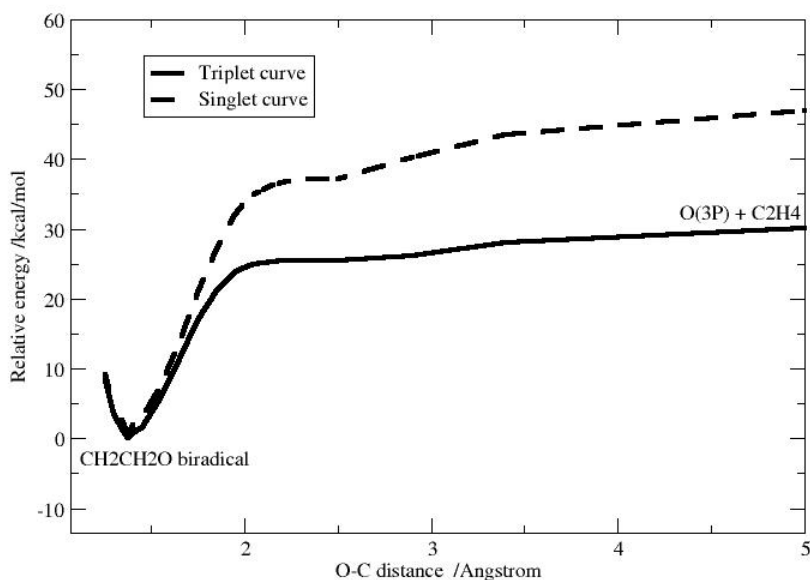
Acetaldehyde is the lowest-lying singlet isomer. Several dissociation channels are open to this molecule for energies accessible starting from O + C_2H_4. These include direct bond cleavage to give CH_3 + CHO, CH_3CO + H and CH_2CHO + H, as well as concerted reactions to produce CH_4 + CO and H_2 + CH_2CO ($^1A_1$). Vinyl alcohol is the

next lowest-energy isomer and is accessible from acetaldehyde via a barrier (TS14) that is lower than any of the dissociation pathways of the latter. Fragmentation of vinyl alcohol, i.e., the C-OH and the O-H bond breakage or through TS17 to give H_2 + CH_2CO, requires much more energy. The ring-opening behavior of oxirane has been studied previously.[167] It was found that the C-O bond rupture back to singlet CH_2CH_2O is energetically favored over C-C breakage to form the biradical ·CH_2—O—CH_2·. We were unable to characterize the C-C bond breaking reaction path with the unrestricted B3LYP calculations, including the formation of singlet CH_2OCH_2 in different face-to-face, edge-to-edge configurations as described in ref. 167. The study of Wortmann-Saleh et al. indicates the possibility of S—T ISC during the oxirane ring opening via C-C bond rupture, but this is not likely to play an important role in the present simulations since isomerization of oxirane to give acetaldehyde dominates in the oxirane dynamics.

5.3.2 Dynamics at Low Energy

In this section we present the results of our direct dynamics TSH calculations at E_{coll} = 0.56 eV (12.9 kcal mol^{-1}). This is the energy for which Casavecchia and coworkers[164] have determined the relative yields $\sigma_i / \sum_i \sigma_i$ (σ_i being the reactive cross section for channel i) for five primary product channels: H + CH_2CHO, CH_3 + CHO, CH_2 + H_2CO, H + CH_3CO and H_2 + CH_2CO. Note that this collision energy is just above the H abstraction barrier (11-12 kcal mol^{-1}) reported by Nguyen et al.,[175] but 7-8 kcal mol^{-1}

higher than the B3LYP/6-31G(d, p) barrier (5-6 kcal mol^{-1}). Since OH + C$_2$H$_3$ is the only endothermic reaction that involves reaction over a higher barrier than is involved in O addition, almost all previous experimental and theoretical studies disregarded this channel. Due to the low H abstraction barrier on the B3LYP surface, we expect an overestimation of this channel in our dynamical results.

For the O (^3P) + C$_2$H$_4$ simulations at 0.56 eV, 545 trajectories were generated, among which 143 trajectories are reactive. We initially propagated the trajectories for a maximum of 4,000 steps (about 960 fs); at the end of that period the ratio of trajectories in the triplet to singlet state is 41:59. Among the reactive trajectories, 14 involve direct H abstraction by O to produce OH + C$_2$H$_3$. The rest involve O addition to form the CH$_2$CH$_2$O triplet adduct. If ISC is not allowed to occur, the excess energy (collision energy + exothermicity) of the activated triplet biradical is rapidly randomized over its internal vibration modes and it can dissociate to various triplet products. However, since the system repeatedly traverses the S—T crossing seam in the vicinity of the biradical intermediate, ISC to the singlet surface is rather efficient. Out of the 129 trajectories that go through the triplet CH$_2$CH$_2$O, 81 hop to the singlet at the end of 4000 steps.

The 48 trajectories that remain on the triplet surface mostly decompose via C-H or C-C bond breaking to give H + CH$_2$CHO or CH$_2$ + CH$_2$O. Isomerization of the CH$_2$CH$_2$O intermediate to triplet CH$_3$CHO is negligible at low collision energies. Within 4,000 integration steps (0.96ps), 21 out of the 48 trajectories dissociate to give H +

CH_2CHO (18 trajectories) and $CH_2 + CH_2O$ (3 trajectories). For the 27 trajectories not decayed at 4000 steps, ISC competes with decomposition in determining product yields.

After the system undergoes *T—S* transition, the singlet CH_2CH_2O rearranges instantaneously to give oxirane (37 out of 81 trajectories), acetaldehyde (38 out of 81), and vinyl alcohol (2 out of 81) within 0.96 ps collision time, along the almost barrierless isomerization reaction paths. We note that the vinyl alcohol channel is much less probable than the acetaldehyde and oxirane channels. Acetaldehyde is about 13 kcal mol^{-1} below vinyl alcohol on the PES, and is thus thermodynamically more favorable. At the same time, however, oxirane lies about 15 kcal mol^{-1} above vinyl alcohol. So the prevalence of the oxirane channel over the vinyl alcohol channel can only be explained from dynamical considerations: the CH_2CH_2O ring-closure process does not have to break any molecular bond, while isomerization to CH_2CHOH involves concerted C-H bond breaking and O-H bond formation. Other than the aforementioned isomerization reactions, the singlet CH_2CH_2O can also decompose via direct H_2 elimination, leading to H_2 + ketene (1 out of 81 trajectories), or H elimination to produce $H + CH_2CHO$ on the singlet surface.

The hot acetaldehyde, oxirane and vinyl alcohol formed upon CH_2CH_2O isomerization on the singlet surface can isomerize among themselves and can undergo further decomposition to various products. For oxirane, the dissociation channels are energetically much more demanding than the ring-opening steps. In fact no direct dissociation of oxirane has been observed in our low-energy trajectories, and only

occasionally does oxirane open its three-membered ring via C-C bond rupture to form CH_2OCH_2, which transforms back to oxirane shortly afterwards. It is worth mentioning that as is the case of CH_2CH_2O, there are crossings of the triplet and singlet surfaces in the vicinity of the CH_2OCH_2 biradical. The short lifetime of the singlet CH_2OCH_2, however, precludes them from playing an important role in the ISC processes. The most frequent reaction of oxirane is to break the C-O bond back to CH_2CH_2O, which rearranges mainly to acetaldehyde. Similarly, vinyl alcohol most likely transforms to its more stable isomer acetaldehyde. Starting from acetaldehyde, there are several competing dissociation pathways: direct bond breakage to produce $CH_3 + CHO$, $H + CH_3CO$, and $H + CH_2CHO$ (in the order of increasing dissociation energy), and molecular elimination to form $CO + CH_4$ and $H_2 + CH_2CO$. Although the CO- and H_2- elimination pathways lead to products that are much lower in energy, the barriers to be surmounted are somewhat higher than the C-C bond dissociation energy, so that the C-C bond breaking to $CH_3 + CHO$ is energetically slightly and dynamically more favorable. Due to the relatively long lifetime of these intermediate complexes, there are only three trajectories that successfully exit the deep valley of CH_3CHO in the first 4000 integration steps, and all lead to $CH_3 + CHO$.

After an initial propagation of 4000 steps (0.96 ps), the majority of reactive trajectories are still trapped as reaction intermediates (27 trajectories as $^3CH_2CH_2O$, 3 as $^1CH_2CH_2O$, 35 as acetaldehyde, 37 as oxirane, and 2 as vinyl alcohol). In order to determine their final dissociation pathways, we further propagated these trajectories for

up to 24,000 steps (for a total of 5.76 ps). We find that the triplet CH_2CH_2O biradicals almost all decompose or transform to CH_3CHO, oxirane and CH_2CHOH within the first 14,000 integration steps. By 24,000 steps, all the triplet complexes have decayed. Thus the triplet to singlet ratio is converged to 25:75 in our direct dynamics TSH calculations, much lower than the experimental ratio of about 43:57.[164] Even after 24,000 steps, there are still 69 singlet trajectories that have not yet decayed (34 as acetaldehyde, 30 as oxirane, and 5 as vinyl alcohol). Of those singlets that do decay, 25 trajectories end up as $CH_3 + CHO$, 3 as $H_2 + CH_2CO$, 2 as $CO + CH_4$, 1 as $H + CH_3CO$ and 1 as $H + CH_2CHO$.

Figure 5-3 plots the reaction cross sections for formation of the various dissociation product pairs as a function of total integration time. This shows that dissociation on the triplet surface via the vinoxy and methylene channels occurs quickly relative to dissociation on the singlet surface. Dissociation of acetaldehyde gradually leads to the production of (mostly) $CH_3 + CHO$ on the singlet surface, and eventually this will become the dominant product.

Figure 5-3.   Reaction cross sections as a function of integration time for the observed dissociation products as well as for the major intermediate complexes on (a) the triplet surface and on (b) the singlet surface. The integration time step is 0.24 fs.
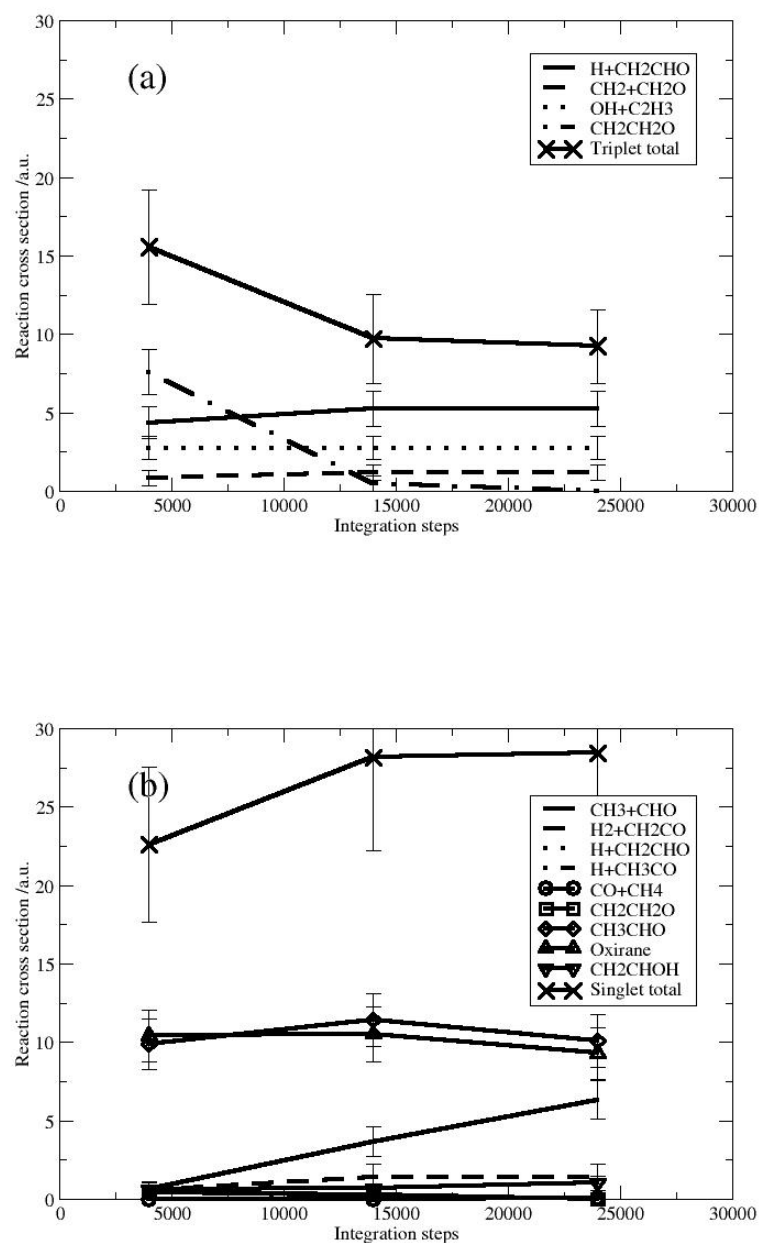
From these results, we can estimate the branching ratios for the primary product channels as follows. Firstly, the OH + C_2H_3, H + CH_2CHO, and CH_2 + CH_2O cross sections (2.8 ± 0.7 a_0^2, 5.3 ± 1.1 a_0^2, and 1.2 ± 0.5 a_0^2, respectively) on the triplet surface are converged since all triplet CH_2CH_2O have dissociated. On the singlet surface, ketene can be produced via the H_2 elimination from singlet CH_2CH_2O or from CH_3CHO. The three trajectories that give H_2 + CH_2CO all belong to the first category (the cross section is 1.4 ± 0.8 a_0^2). For the remaining singlet trajectories, we can assume that oxirane and CH_2CHOH will eventually convert to CH_3CHO, which further undergoes unimolecular decomposition to give product yields that can be determined by extrapolation. Compared to the C-C bond breakage product (CH_3 + CHO), the other dissociation channels (H + CH_3CO, H + CH_2CHO, CO + CH_4, and H_2 + CH_2CO) are minor. At the end of 0.96 ps, the CH_3 + CHO channel cross section is 0.7 ± 0.4 a_0^2, the other channels altogether are zero, which means a 100% rate of production for CH_3 + CHO. At 3.36 ps, the CH_3 cross section increases to 3.7 ± 0.9 a_0^2, while that of the other channels is only 0.1 ± 0.1 a_0^2 (97% branching for CH_3 + CHO). By 5.76 ps, the former becomes 6.3 ± 1.2 a_0^2, and the latter increases slightly to 0.2 ± 0.2 a_0^2 (96% for CH_3 + CHO). In a second set of 545 trajectories that we generated (described below) for a SOC of 50 cm^{-1}, the rate of production of CH_3 + CHO among the acetaldehyde reaction channels is found to be 70%. Nominally this ratio should be the same no matter what the SOC is, as dissociation of acetaldehyde on the singlet surface is largely unaffected by the ISC processes. However,

the statistics of both sets of calculations is poor, corresponding to fewer than 30

trajectories dissociating on the singlet surface. To provide an overall estimate of the

branching, we used an average value from the two sets of calculations, ~83%, for the

branching fraction to give C-C bond breakage. This is a similar result to that obtained in

the experiment, where the methyl channel is responsible for roughly 75% of all singlet

products, assuming that channels R4 through R7 arise only from the singlet surface.

Overall the calculated cross section for the singlet intermediate complexes that have not

dissociated by 5.76 ps is $20.4 \pm 3.8\, a_0^2$, so, assuming that 83% of them decay via C-C

breakage, the total CH_3 + CHO reaction cross section is estimated to be

$$\left(6.3 + 20.4 \times 83\%\right) \pm \left(1.2 + 3.8 \times 83\%\right) = 23.2 \pm 4.4 a_0^2 .$$

Table 5-1. Reactive cross sections (in units of a_0^2) of the five primary product channels
from our direct dynamics calculations at low and hyperthermal collision energies.

		$H +$ CH_2CHO	$CH_2 +$ CH_2O	$OH +$ C_2H_3	$CH_3 +$ CHO	$H_2 +$ CH_2CO
E_{coll}=0.56 eV	V_{13}=70 cm^{-1}	5.3±1.1	1.2±0.5	2.8±0.7	23.2±4.4[*]	>1.4±0.8 and <4.9±1.5[*]
	V_{13}=50 cm^{-1}	7.6±1.8	1.0±0.4	1.9±0.6	18.5±4.4[*]	>1.1±0.6 and <4.4±1.3[*]
E_{coll}=3.0 eV	V_{13}=70 cm^{-1}	8.3±1.4	10.5±1.6	7.4±1.5	4.6±1.1	0.3±0.3

[*] These values are extrapolated from trajectories that remained trapped in local potential
wells after an integration time of 5.76 ps as described in the text.

Table 5-2. Product relative yields for the O(^3P) + C$_2$H$_4$ reaction at E_{coll}=0.56 eV

		H + CH$_2$CHO	CH$_2$ + CH$_2$O	OH + C$_2$H$_3$	CH$_3$ + CHO	H$_2$ + CH$_2$CO
Theory	V_{13}=70 cm^{-1}	14±6%	3±2%	7±4%	62±27%	>4±3% and <13±7%
	V_{13}=50 cm^{-1}	22±12%	3±2%	6±3%	55±29%	>3±3% and <13±8%
Experiment[164]		27±6%	16±8%		43±11%	13±3%

Table 5-1 tabulates the reactive cross sections (either calculated or estimated from our trajectory calculations) for the primary product channels at E_{coll}=0.56 eV using a V_{13}=70 cm^{-1}. The results obtained using a smaller V_{13} of 50 cm^{-1} as well as at a hyperthermal collision energy of 3.0 eV are also listed. We further compare in Table 5-2 our calculated branching ratios for these products with those from the experiment at E_{coll}=0.56 eV. Obviously the two product channels that are much overestimated are OH + C$_2$H$_3$ and CH$_3$ + CHO. The former is due to an H abstraction barrier on the B3LYP surface that is too low. In fact, this channel has not been observed in low-energy experiments. The 62% relative yield of the methyl channel (the experimental branching is 43%) can only be explained by too much ISC in our trajectory calculations. We assess this point later when we present results for smaller SOC values.

There has been much uncertainty in past experimental work concerning the yield of the ketene channel, the second most important dissociation product on the singlet surface. As discussed above, H$_2$ + CH$_2$CO comes from either direct dissociation of

singlet CH_2CH_2O or unimolecular decomposition of acetaldehyde. Our trajectories show that the first route dominates for short propagation times, and by 5.76 ps the ketene formation cross section is $1.4 \pm 0.8\,a_0^2$ (corresponding to 4% of the total yield), comparable to the methylene channel cross section of $1.2 \pm 0.5\,a_0^2$. Given longer integration times, the ketene channel will increase due to H_2 elimination from acetaldehyde. This gives us a lower bound of >4% for the ketene channel. An upper bound can be determined by assuming that all of the acetaldehyde which does not dissociate to give the methyl channel gives the ketene channel instead. This gives an estimate of <13% as noted in Table 5-2. As to the triplet products $H + CH_2CHO$ and $CH_2 + CH_2O$, their yields are underestimated due to the overestimated ISC. In particular, the branching ratio of the methylene channel is only 25% of that of the vinoxy channel, lower than the experimental ratio of about 60%.

We tested two smaller values of SOC, 50 cm^{-1} and 30 cm^{-1}, for calculating the transition probabilities at the T—S crossing points along the trajectories. The ratios of the triplet to singlet yields are compared in Figure 5-4 for the three values of the SOC parameter used in the direct dynamics simulations. It is found that a V_{13} of 50 cm^{-1} still results in too much ISC in the trajectory output, with the triplet to singlet ratio being 30:70 while the experimental ratio is 43:57. When V_{13} is further decreased to 30 cm^{-1}, there is a sharp reduction in intersystem crossing, such that after 4,000 steps the triplet to singlet branching is 88:12. Thus to match experimental triplet/singlet branching, a SOC between 30 cm^{-1} and 50 cm^{-1} is needed. This would be comparable to that estimated from

our CASSCF calculations (35 cm^{-1}) as described earlier. However, a precise match with experiment using the CASSCF value is not expected due to approximations in the dynamics calculations. There are a variety of factors in the TSH method that would lead to deviations between theory and experiment, including the quality of the potential energy surfaces, the neglect of surface hopping away from the intersection points, and approximations in the basic TSH algorithm. Past comparisons of more sophisticated TSH calculations with accurate quantum results[176(a), 182] suggest that transition probabilities can often be off by a factor of two, so in this respect, the agreement between theory and experiment in the present application is actually quite good.

Figure 5-4. Branching fractions $\sigma_i \big/ \sum_i \sigma_i$ for the triplet products when different values of the spin-orbit coupling V_{13} are used to compute the transition probabilities at the triplet—singlet crossing points. The experimental value[164] is 0.43. The integration time step is 0.24 fs.
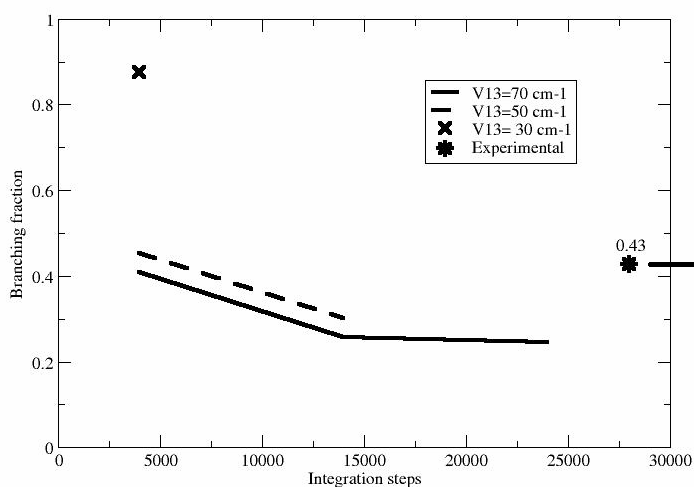
Figure 5-5. Angular distributions expressed as normalized differential cross sections (DCS, $(2\pi/\sigma)(d\sigma/d\Omega')$) in (a) the center-of-mass frame and (b) the laboratory frame for the vinoxy and methyl products from the B3LYP trajectory calculations. The inset shows the lab distribution and the Newton circle from the experiment.[164]
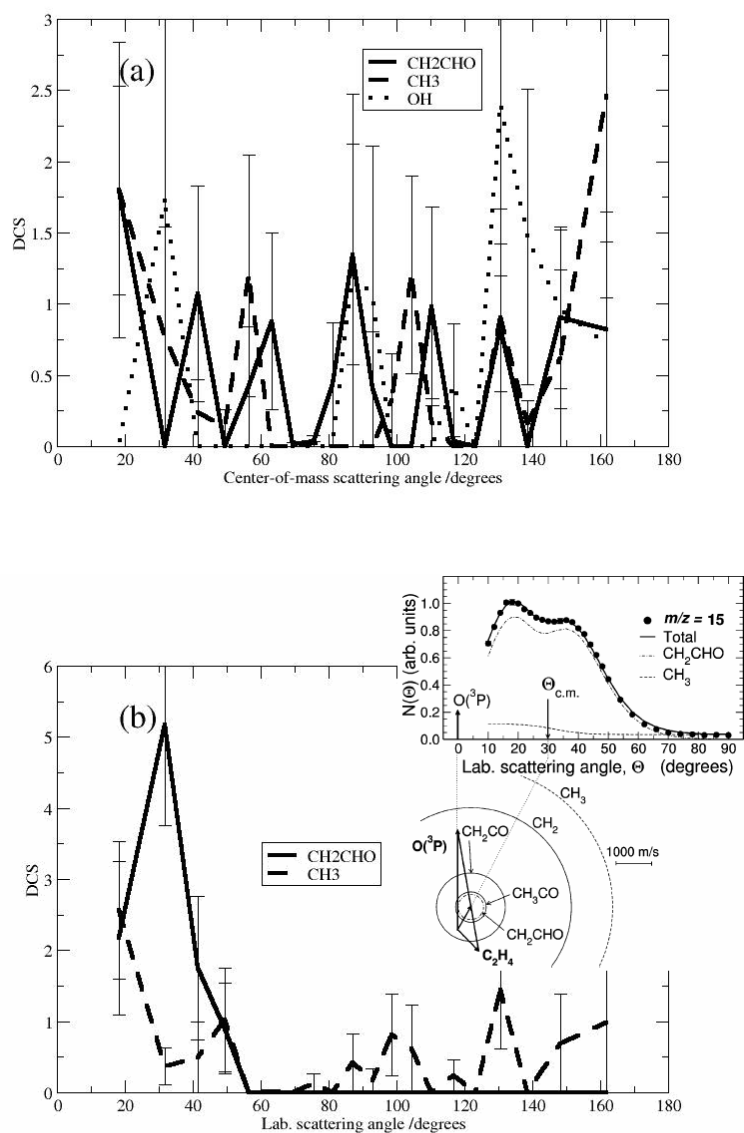
Based on calculations using V_{13}=50 cm^{-1}, we determined the product branching ratios that are also listed in Table 5-2. It is shown that the methyl channel relative yield decreases to 55% and the vinoxy channel increases to 22% due to a reduction in ISC when SOC is lowered from 70 cm^{-1} to 50 cm^{-1}. However, we do not see a corresponding increase in the methylene channel relative yield. Both the methylene and the ketene channels are underestimated as compared to the experiment.

We now examine the product angular distributions for the vinoxy channel, the methyl channel, and the hydroxyl channel, obtained at 5.76 ps integration time with the SOC parameter of 70 cm^{-1}. The OH center-of-mass angular distribution shows a small preference for the backward direction with respect to the incoming oxygen atom (Figure 5-5a), which is consistent with a rebound mechanism for direct abstraction in which O attacks along the C-H bond and the resulting OH bounces back the same way. The angular distributions for CH$_2$CHO and CH$_3$ are almost forward-backward symmetric, which is typical of reactions that proceed through long-lived intermediate complexes. The Casavecchia et al. experiment measured the lab frame angular distributions for CH$_2$CHO and CH$_3$. By converting the velocities into the lab frame, we obtain lab angular distributions that can be compared with the experiment (Figure 5-5b). We see qualitative agreement between theory and experiment, with CH$_2$CHO scattered in the forward hemisphere and CH$_3$ scattered in all directions, consistent with the picture that can be drawn from the Newton diagram.

5.3.3 Dynamics at Hyperthermal Energy

Collisions of the reactant molecules in the hyperthermal regime allow areas of the PES that are forbidden at low energy to be accessed; therefore, high-energy barrier reaction pathways are now open, as well as secondary steps in which the products further dissociate. In addition, as the reactivity on the triplet surface is very much enhanced, ISC plays a less important role at high energies.

A total of 592 trajectories were calculated for E_{coll} = 3.0 eV (69.2 kcal mol^{-1}), among which 236 are reactive. We integrated the trajectories for a maximum of 4,000 steps (0.96 ps), and only 20 trajectories are trapped as intermediate complexes at the end of the propagation (1 as triplet CH_2CH_2O, 5 as oxirane, 3 as acetaldehyde, 2 as triplet CH_2CHOH, and 9 as singlet CH_2CHOH). The triplet yield versus the singlet yield is determined to be 71:29, much larger than for low energy trajectories (25:75). Note that we still use a SOC of 70 cm^{-1} in these calculations, so the formation of singlet products is likely less important than we estimate.

Another noticeable difference is an increase in importance of the CH_2CHOH channel at high energies. As we discussed earlier, vinyl alcohol is the least favorable among the CH_2CH_2O isomerization reactions on the singlet surface. As the collision energy increases, however, isomerization of the triplet CH_2CH_2O biradical is possible in addition to the direct decomposition to H + CH_2CHO and CH_2 + CH_2O. We even observed one trajectory that undergoes a $^3CH_2CH_2O \xrightarrow{\text{TS9}} {}^3CH_2OCH_2$ transformation on the triplet surface, for which the barrier is as high as 57.2 kcal mol^{-1}. So a considerable

amount of CH_2CHOH can be produced in the triplet state. The triplet and singlet surfaces cross close to the triplet configuration of CH_2CHOH, so when a trajectory is trapped in the triplet CH_2CHOH valley, surface hops to the singlet state are possible. This provides an alternative route to the formation of CH_2CHOH in the singlet state. Starting from triplet and singlet CH_2CHOH, a variety of decomposition channels are now accessible: O-H bond breakage to give $H + CH_2CHO$, C-O bond breaking to $OH + C_2H_3$, C-H bond breaking to $H + CH_2COH$ or $H + CHCH(OH)$, and even molecular elimination to $H_2O + C_2H_2$ or $H_2O + CH_2C$. The $^3CH_2CH_2O \rightarrow {}^3CH_3CHO$ isomerization is another important reaction on the triplet surface, which subsequently leads to mainly $CH_3 + CHO$ via C-C bond breakage.

The above mechanisms are still minor channels compared to CH_2CH_2O dissociation to $H + CH_2CHO$ and $CH_2 + CH_2O$ on the triplet surface and to acetaldehyde C-C breakage to give $CH_3 + CHO$ on the singlet surface. There is also an increase in the production of $CO + CH_4$ from acetaldehyde. We should emphasize that products that exclusively come from the singlet surface such as $CH_3 + CHO$ and $H_2 + CH_2CO$, or exclusively come from the triplet surface such as $OH + C_2H_3$, $H + CH_2CHO$ and $CH_2 + CH_2O$ in low energy collisions, can now be produced by both triplet and singlet mechanisms. For instance, about 37% of the total $CH_3 + CHO$ yield arises from triplet CH_3CHO decomposition. In Figure 5-6, we plot the reaction cross sections as function of collision energy for the four major dissociation products. Due to diminished ISC, the $OH + C_2H_3$, $H + CH_2CHO$ and $CH_2 + CH_2O$ channels, which orginate mainly from reactions

on the triplet surface, dominate the overall product yields at 3.0 eV collision energy. The

CH_3 + CHO channel, which is the primary product at 0.56 eV, rapidly loses its

dominance to other channels as collision energy increases. The methylene cross section

increases much more rapidly with increasing energy than do vinoxy and hydroxyl

channels so that CH_2 + CH_2O becomes the most abundant product at 3.0 eV. In summary,

our computed product branching ratios at 3.0 eV are as follows: 32±14% for CH_2 +

CH_2O, 25±12% for H + CH_2CHO, 23±11% for OH + C_2H_3, 14±8% for CH_3 + CHO,

4±3% for CO + (CH_4 or CH_3 +H, or CH_2 + H_2), and roughly 1% for H_2 + CH_2CO.

Figure 5-6.   Reactive cross sections for the primary dissociation products at 0.56 eV and 3.0 eV collision energies.
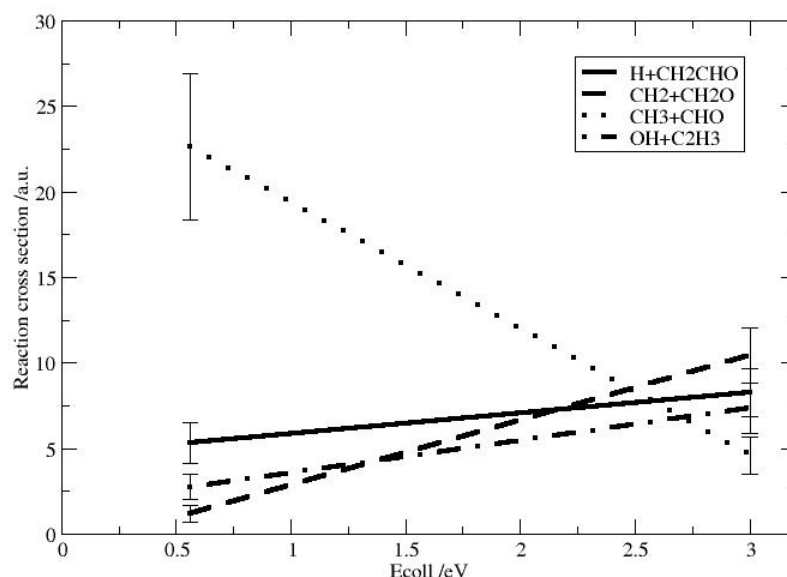
5.4 Summary

This chapter has explored intersystem crossing effects in the O (^3P) + C_2H_4 reaction dynamics. We first examined low energy collisions at 0.56 eV in order to simulate the crossed molecular beam experiment by Casavecchia et al.[164] We used a simplified version of the quasiclassical trajectory surface hopping method in which the Landau-Zener formula is employed to calculate transition probabilities with a constant spin-orbit coupling at all triple—singlet surface crossing points. The potential energy surfaces are generated "on the fly" at the unrestricted B3LYP/6-31G(d, p) level. We found that ISC effects were sensitive to the value of the SOC parameter used in our trajectory simulations. When a SOC of 70 cm^{-1} was used to compute the transition probabilities, the rate of triple—singlet transitions was significantly overestimated with the singlet product CH_3 + CHO accounting for 62±27% of the overall reaction yield (the experimental ratio is 43±11%), much higher than the second most abundant triplet product H + CH_2CHO (14±6% versus the experimental 27±6%). A SOC of 50 cm^{-1} brings down the singlet ratio and leads to better agreement with experiment as to the methyl and vinoxy product relative yields. As we go to higher collision energy (3 eV), ISC plays a much less important role due to the enhanced reactivity on the triplet surface. As a result triplet products dominate over singlet products at hyperthermal energies. Furthermore, the triplet channel CH_2 + CH_2O exceeds that of the H + vinoxy and methyl

+ CHO channels and becomes the most abundant products. Some novel reaction channels that are inaccessible at low energy are also found.

Bibliography

1. Zare, R. N. *Science* **1998**, *279*, 5358.
2. Levine, R. D.; Bernstein, R. B. *Molecular Reaction Dynamics and Chemical Reactivity*, Oxford University, London, 1987.
3. Zewail, A. H. *Femtochemistry: Atomic-Scale Dynamics of the Chemical Bond Using Ultrafast Lasers*, The Nobel Prize in Chemistry, 1999.
4. Arrhenius, S. *Z. Physik. Chem*. **1889**, *4*, 226.
5. Trautz, M. *Z. Anorg. Allgem. Chem*. **1916**, *96*, 1.
6. Lewis, W. C. McC. *J. Chem. Soc*. **1918**, *113*, 471.
7. Eyring, H. *J. Chem. Phys*. **1935**, *3*, 107.
8. Evans, M. G.; Polanyi, M. *Trans. Faraday Soc*. **1935**, *31*, 875.
9. Wigner, E. *J. Chem. Phys*. **1937**, *5*, 720; Horiuti, J. *Bull. Chem. Soc. Japan*. **1938**, *13*, 210; Keck, J. C. *J. Chem. Phys*. **1960**, *32*, 1035; Keck, J. C. *Adv. Chem. Phys*. **1967**, *13*, 85; Truhlar, D. G.; Garrett, B. C. *Annu. Rev. Phys. Chem*. **1984**, *35*, 159.
10. Fernandez-Ramos, A.; Ellingson, B. A.; Garrett, B. C.; Truhlar, D. G. Variational Transition State Theory with Multidimensional Tunneling, in *Reviews in Computational Chemistry*, Vol. 23, Lipkowitz, K. B.; Cundari, T. R., Eds., Wiley-VCH, Hoboken, NJ, 2007, pp. 125-232.
11. Garrett, B. C.; Truhlar, D. G. Transition State Theory, in *The Encyclopedia of Computational Chemistry*, Schleyer, P. v. R.; Allinger, N. L.; Clark, T.; Gasteiger, J.; Kollman, P. A.; Schaefer III, H. F.; Schreiner, P. R., Eds., John Wiley & Sons, Chichester, 1998, pp. 3094-3104.
12. (a) Herschbach, D. R. *Angew. Chem. Int. Ed. Engl*. **1987**, *26*, 1221; (b) Lee, Y. T. *Science* **1987**, *236*, 793; (c) Polanyi, J. C. *Science* **1987**, *236*, 680; (d) Zewail, A. H. *J. Phys. Chem. A* **2000**, *104*, 5660.
13. Eyring, H.; Polanyi, M. *Z. Physik. Chem*. **1931**, *B12*, 279.
14. Schatz, G. C. *J. Phys. Chem*. **1996**, *100*, 12839.
15. Bowman, J. M.; Schatz, G. C. *Annu. Rev. Phys. Chem*. **1995**, *46*, 169.
16. Polanyi, J. C.; Wong, W. H. *J. Chem. Phys*. **1969**, *51*, 1439.
17. Schatz, G. C.; Elgersma, H. *Chem. Phys. Lett*. **1980**, *73*, 21; Elgersma, H.; Schatz, G. C. *Int. J. Quant. Chem. Quant. Chem. Symp*. **1981**, *15*, 611; Schatz, G. C.; Colton, M. C.; Grant, J. L. *J. Phys. Chem*. **1984**, *88*, 2971.

18. Sinha, A.; Hsiao, M. C.; Crim, F. F. *J. Chem. Phys.* **1990**, *92*, 6333; Bronikowski, M. J.; Simpson, W. R.; Girard, B.; Zare, R. N. *J. Chem. Phys.* **1991**, *95*, 8647.

19. Schrödinger, E. *Ann. Physik.* **1926**, *81*, 109.

20. Born, M.; Oppenheimer, R. *Ann. Phys.* **1927**, *84*, 457; Born, M.; Huang, K. *The Dynamical Theory of Crystal Lattices*, Oxford University Press, Oxford, U.K., 1954.

21. Clary,D. C. *Science* **1998**, *279*, 1879; Althorpe, S. C.; Clary, D. C. *Annu. Rev. Phys. Chem*. **2003**, *54*, 493.

22. Hu, W.; Schatz, G. C. *J. Chem. Phys.* **2006**, *125*, 132301.

23. Pack, R. T *J. Chem. Phys.* **1974**, *53*, 633; McGuire, P.; Kouri, D. J. *J. Chem. Phys.* **1974**, *60*, 2488; Bowman, J. M. *Adv. Chem. Phys.* **1985**, *61*, 115; Gerber, R. B.; Ratner, M. A. *Adv. Chem. Phys.* **1988**, *70*, 97; Walker, R. B.; Light, J. C. *Annu. Rev. Phys. Chem*. **1980**, *31*, 401.

24. (a) Karplus, M.; Porter, R. N.; Sharma, R. D. *J. Chem. Phys.* **1965**, *43*, 3259; (b) Bunker, D. L.; Porter, R. N. *Annu. Rev. Phys. Chem*. **1974**, *25*, 317.

25. Miller, W. H.; *J. Chem. Phys.* **1970**, *53*, 1949; Marcus, R. A. *Chem. Phys. Lett.* **1970**, *7*, 525.

26. Tully, J. C.; Preston, R. K. *J. Chem. Phys.* **1971**, *55*, 562; Miller, W. H.; George, T. F. *J. Chem. Phys.* **1972**, *56*, 5637.

27. Child, M. S. Semiclassical Methods in Molecular Collision Theory, in *Dynamics of Molecular Collisions*, Part B, Miller, W. H. Ed., Plenum Press, N.Y., 1976.

28. Zhang, J. Z. H. *Theory and Application of Quantum Molecular Dynamics*, Chap. 1, World Scientific, Singapore, 1999.

29. Tully, J. C. Non-adiabatic Process in Molecular Collisions, in *Dynamics of Molecular Collisions*, Part B, Miller, W. H. Ed., Plenum Press, N.Y., 1976.

30. Jasper, A. W.; Kendrick, B. K.; Mead, C. A.; Truhlar, D. G. Non-Born-Oppenheimer Chemistry: Potential Surfaces, Couplings, and Dynamics, in *Modern Trends in Chemical Reaction Dynamics: Experiment and Theory*, Part 1, Yang, X.; Liu, K. Eds., World Scientific, Singapore, 2004.

31. Topaler, M. S.; Allison, T. C.; Schwenke, D. W.; Truhlar, D. G. *J. Chem. Phys.* **1998**, *109*, 3321; Hack, M. D.; Truhlar, D. G. *J. Phys. Chem. A* **2000**, *104*, 7917.

32. Worth, G. A.; Robb, M. A. *Adv. Chem. Phys.* **2002**, *124*, 355; Meyer, H. D.; Worth, G. A. *Theor. Chem. Acc.* **2003**, *109*, 251.

33. Murrel, J. N.; Carter, S.; Farantos, S. C.; Huxley, P.; Varandas, A. J. C. *Molecular Potential Energy Functions*, Wiley, New York, 1984.

34. Dunning, T. H., Jr.; Harding, L. B. Ab Initio Determination of Potential Energy Surfaces for Chemical Reactions, in *Theory of Chemical Reaction Dynamics*, Vol. I, Baer, M. Ed., CRC Press, Boca Raton, FL, 1985.

35. Schatz, G. C. *Rev. Mod. Phys.* **1989**, *61*, 669; Varandas, A. J. C. *Adv. Chem. Phys.* **1988**, *74*, 255; Schatz, G. C. Fitting Potential Energy Surfaces, in *Reaction and Molecular Dynamics* (*Lecture Notes in Chemistry*, Vol. 75), Lagana, A.; Riganelli, A. Eds., Springer, Berlin, 2000.

36. Car, R.; Parrinello, M. *Phys. Rev. Lett.* **1985**, *55*, 2471.

37. Bolton, K.; Hase, W. L.; Peslherbe, G. H. Direct Dynamics Simulations of Reactive Systems, in *Modern Methods for multidimensional Dynamics Computations in Chemistry*, Thompson, D. L. Ed., World Scientific, Singapore, 1998.

38. Raff, L. M.; Thompson, D. L. The Classical Trajectory Approach to Reactive Scattering, in *Theory of Chemical Reaction Dynamics*, Vol. III, Baer, M. Ed., CRC Press, Boca Raton, FL, 1985.

39. Hirschfelder, J.; Eyring, H.; Topley, B. *J. Chem. Phys.* **1936**, *4*, 170.

40. Schatz, G. C. *J. Chem. Phys.* **1983**, *79*, 5386; Lu, D.-H.; Hase, W. L. *J. Chem. Phys.* **1988**, *89*, 6723; Miller, W. H.; Hase, W. L.; Darling, L. *J. Chem. Phys.* **1989**, *91*, 2863; Bowman, J. M.; Gazdy, B.; Sun, Q. *J. Chem. Phys.* **1989**, *91*, 2856; Sewell, T. D.; Thompson, D. L.; Gezelter, J. D.; Miller, W. H. *Chem. Phys. Lett.* **1992**, *193*, 512; Peslherbe, G. L.; Hase, W. L. *J. Chem. Phys.* **1994**, *100*, 1179; Ben-Nun, M.; Levine, R. D. *J. Chem. Phys.* **1994**, *101*, 8768.

41. Miller, W. H. *J. Phys. Chem. A* **2001**, *105*, 2942.

42. Schatz, G. C.; ter Horst, M.; Takayanagi, T. Computational Methods for Polyatomic Bimolecular Reactions, in *Modern Methods for Multidimensional Dynamics Computations in Chemistry*, Thompson, D. L. Ed., World Scientific, Singapore, 1998.

43. Aoiz, F. J.; Banares, L.; Herrero, V. J. *J. Chem. Soc., Faraday Trans.* **1998**, *94*, 2483.

44. Schreider, Y. A. *The Monte-Carlo Method*, Pergamon Press, Inc., Elmsford, N.Y., 1966.

45. *Dynamics of Molecules and Chemical Reactions*, Wyatt, R. E.; Zhang, J. Z. H. Eds., Marcel Dekker, N.Y., 1996, Chaps. 13-16; *Advances in Classical Trajectory Methods*, Hase, W. L. Ed., JAI, Greenwich, CT, 1998, Vol. 3.

46. Schatz, G. C. *J. Phys. Chem.* **1995**, *99*, 516.

47. Schatz, G. C. in *Molecular Collision Dynamics (Topics in Current Physics*, Vol. 33), Bowman, J. M. Ed., Heidelberg, Springer-Verlag, 1983, pp 25-60.

48. Percival, I. C. *Adv. Chem. Phys.* **1977**, *36*, 1.

49. Noid, D. W.; Koszykowski, M. L.; Marcus, R. A. *Annu. Rev. Phys. Chem.* **1981**, *32*, 267.

50. Eaker, C. W.; Schatz, G. C. *J. Chem. Phys.* **1984**, *81*, 2394; Eaker, C. W.; Schatz, G. C.; DeLeon, N.; Heller, E. J. *J. Chem. Phys.* **1984**, *81*, 5913; Binney, J.; Spergel, D. *Monthly Notices Roy. Astron. Soc.* **1984**, *206*, 159; Martens, C. C.; Ezra, G. S. *J. Chem. Phys.* **1985**, *83*, 2990.

51. Skodje, R. T.; Borondo, F.; Reinhardt, W. P. *J. Chem. Phys.* **1985**, *82*, 4611; Huang, J.; Valentini, J. J.; Muckerman, J. T. *J. Chem. Phys.* **1995**, *102*, 5695.

52. Goldstein, H. *Classical Mechanics*, Addison-Wesley, Reading, Mass., 1965.

53. Bunker, D. L.; Porter, R. N. *Annu. Rev. Phys. Chem.* **1974**, *25*, 317.

54. *Numerical Recipes in FORTRAN: The Art of Scientific computing*, 2nd Ed. Press,

W. H.; Flannery, B. P.; Teukolsky, S. A.; Vetterling, W. T. Cambridge[England]; New York, NY, USA, Cambridge University Press. 1992.

55. Porter, R. N.; Raff, L. M.; Miller, W. H. *J. Chem. Phys.* **1975**, *63*, 2214.

56. Blais, N. C.; Truhlar, D. G. *J. Chem. Phys.* **1976**, *65*, 5335.

57. Landau, L. D. *Phys. Z. Sowjetunion* **1932**, *2*, 46.

58. Zener, C. *Proc. Roy. Soc. London A* **1932**, *137*, 696.

59. Stueckelberg, E. C. G. *Helv. Phys. Acta* **1932**, *5*, 369.

60. Nikitin, E. E. *Chem. Phys. Lett.* **1967**, *1*, 179.

61. Tully, J. C.; Preston, R. K. *J. Chem. Phys.* **1971**, *55*, 562.

62. Tully, J. C. *J. Chem. Phys.* **1990**, *93*, 1061.

63. Topaler, M. S.; Hack, M. D.; Allison, T. C.; Liu, Y.-P.; Mielke, S. L.; Schwenke, D. W.; Truhlar, D. G. *J. Chem. Phys.* **1997**, *106*, 8699.

64. Meyer, H. -D.; Miller, W. H. *J. Chem. Phys.* **1979**, *70*, 1979; *ibid.* **1979**, *70*, 3214.

65. Gerber, R. B.; Buch, V.; Ratner, M. A. *J. Chem. Phys.* **1982**, *77*, 3022.

66. Buch, V.; Gerber, R. B.; Ratner, M. A. *Chem. Phys. Lett.* **1983**, *101*, 44.

67. Micha, D. A. *J. Chem. Phys.* **1983**, *78*, 7138.

68. Durup, J. *Chem. Phys. Lett.* **1990**, *173*, 537.

69. Alimi, R.; Gerber, R. B.; Hammerich, A. D.; Kosloff, R.; Ratner, M. A. *J. Chem. Phys.* **1990**, *93*, 6484.

70. García,-Vela, A.; Gerber, R. B.; Imre, D. G. *J. Chem. Phys.* **1992**, *97*, 7242.

71. Warnatz, J. in *Combustion Chemistry* J. Gardiner, W. C., Ed. (Springer-Verlag, New York, 1984) pp. 197-360.

72. Kurylo, M. J.; Hollinden, G. A.; Timmons, R. B. *J. Chem. Phys.* **1970**, *52*, 1773.

73. Shaw, R. *J. Phys. Chem. Ref. Data* **1978**, *7*, 1179.

74. Sepehrad, A.; Marshall, R. M.; Purnell, H. *J. Chem. Soc., Faraday Trans. 1* **1979**, *75*, 835.

75. Baulch, D. L.; Cobos, C. J.; Cox, R. A.; Esser, C.; Frank, P.; Just, T.; Kerr, J. A.; Pilling, M. J.; Troe, J.; Walker, R. W.; Warnatz, J. *J. Phys. Chem. Ref. Data* **1992**, *21*, 411; Rabinowitz, M. J.; Sutherland, J. W.; Patterson, P. M.; Klemm, B. R. *J. Phys. Chem.* **1991**, *95*, 674; Marquaire, P. M.; Dastidar, A. G.; Manthorne, K. C.; Pacey, P. D. *Can. J. Chem.* **1994**, *72*, 600; Bryukov, M. G.; Slagle, I. R.; Knyazev, V. D. *J. Phys. Chem. A* **2001**, *105*, 3107.

76. Sutherland, J. W.; Su, M.-C.; Michael, J. V. *Int. J. Chem. Kinet.* **2001**, *33*, 669.

77. Tsang, W.; Hampson, R. F. *J. Phys. Chem. Ref. Data* **1986**, *15*, 1087; Baeck, H. J.; Shin, K. S.; Yang, H.; Qin, Z.; Lissianski, V.; Gardner, J. *J. Phys. Chem.* **1995**, *99*, 15925; Knyazev, V. D.; Bencsura, A.; Stoliarov, S. I.; Slagle, I. R. *J. Phys. Chem.* **1996**, *100*, 11346.

78. Germann, G.; Huh, Y.; Valentini, J. *J. Chem. Phys.* **1992**, *96*, 1957.

79. Camden, J. P.; Bechtel, H. A.; Zare, R. N. *Angew. Chem. Int. Ed.* **2003**, *42*, 5227.

80. Kuntz, P. J.; Nemeth, E. M.; Polanyi, J. C.; Wong, W. H. *J. Chem. Phys.* **1969**, *52*, 4654.

81. Raff, L. M. *J. Chem. Phys.* **1974**, *60*, 2220.

82. Valencich, T.; Bunker, D. L. *J. Chem. Phys.* **1974**, *61*, 21.

83. Chattopadhyay, A.; Tasaki, S.; Bersohn, R.; Kawasaki, M. *J. Chem. Phys.* **1991**, *95*, 1033.

84. Walch, S. P. *J. Chem. Phys.* **1980**, *72*, 4932.

85. Schatz, G. C.; Walch, S. P.; Wagner, A. F. *J. Chem. Phys.* **1980**, *73*, 4536.

86. Schatz, G. C.; Wagner, A. F. Dunning, T. H. J. *J. Phys. Chem.* **1984**, *88*, 221.

87. Kraka, E.; Gauss, J.; Cremer, D. *J. Chem. Phys.* **1993**, *99*, 5306.

88. Dobbs, K. D.; Dixon, D. A. *J. Phys. Chem.* **1994**, *98*, 5290.

89. Bunker, D. L.; Pattengill, M. D. *J. Chem. Phys.* **1970**, *53*, 3041.

90. Valencich, T.; Bunker, D. L. *Chem. Phys. Lett.* **1973**, *20*, 50.

91. Chapman, S.; Bunker, D. L. *J. Chem. Phys.* **1975**, *62*, 2890.

92. Steckler, R.; Dykema, K. J.; Brown, F. B.; Hancock, G. C.; Truhlar, D. G.; Valencich, T. *J. Chem. Phys.* **1987**, *87*, 7024.

93. Joseph, T.; Steckler, R.; Truhlar, D. G.; *J. Chem. Phys.* **1987**, *87*, 7036.

94. Jordan, M. J. T.; Gilbert, R. G. *J. Chem. Phys.* **1995**, *102*, 5669.

95. Huang, J.; Valentini, J. J.; Muckerman, J. T. *J. Chem. Phys.* **1995**, *102*, 5695.

96. Takayanagi, T. *J. Chem. Phys.* **1996**, *104*, 2237.

97. Yu, H.-G.; Nyman, G. *J. Chem. Phys.* **1999**, *111*, 3508.

98. Yu, H.-G. *Chem. Phys. Lett.* **2000**, *332*, 538.

99. Wang, M. L.; Li, Y.; Zhang, J. Z. H.; Zhang, D. H. *J. Chem. Phys.* **2000**, *113*, 1802.

100. Wang, D.; Bowman, J. M.; *J. Chem. Phys.* **2001**, *115*, 2055.

101. Yang, M.; Zhang, D. H.; Lee, S.-Y. *J. Chem. Phys.* **2002**, *117*, 9539.

102. Palma, J.; Echave, J.; Clary, D. C. *J. Phys. Chem. A* **2002**, *106*, 8256.

103. Huarte-Larrañaga, F.; Manthe, U. *J. Chem. Phys.* **2000**, *113*, 5115.

104. Bowman, J. M.; Wang, D.; Huang, X.; Huarte-Larrañaga, F.; Manthe, U. *J. Chem. Phys.* **2001**, *114*, 9683.

105. Huarte-Larrañaga, F.; Manthe, U. *J. Phys. Chem. A* **2001**, *105*, 2522.

106. Huarte-Larrañaga, F.; Manthe, U. *J. Chem. Phys.* **2002**, *116*, 2863.

107. Pu, J.; Corchado, J. C.; Truhlar, D. G. *J. Chem. Phys.* **2001**, *115*, 6266.

108. Pu, J.; Truhlar, D. G. *J. Chem. Phys.* **2002**, *116*, 1468.

109. Espinosa-García, J.; Corchado, J. C. *J. Chem. Phys.* **2000**, *112*, 5731.

110. Espinosa-García, J. *J. Chem. Phys.* **2002**, *112*,10664.

111. Zhang, X.; Yang, G. H.; Han, K. L.; Wang, M. L. Zhang, J. Z. H. *J. Chem. Phys.* **2003**, *118*,9266.

112. Wu, T.; Manthe, U. *J. Chem. Phys.* **2003**, *119*, 14.

113. Kerkeni, B.; Clary, D. C. *J. Chem. Phys.* **2004**, *120*, 2308.

114. Zhao, Y.; Yamamoto, T.; Miller, W. H. *J. Chem. Phys.* **2004**, *120*, 3100.

115. Wu, T.; Werner, H.-J.; Manthe, U. *Science* **2004**, *306*, 2227.

116. Duchovic, R. J.; Hase, W. L.; Schlegel, H. B. *J. Phys. Chem.* **1984**, *88*, 1339.

117. Jordan, M. J. T.; Thompson, K. C.; Collins, M. A. *J. Chem. Phys.* **1995**, *102*, 5647.

118. Thompson, K. C.; Jordan, M. J. T.; Collins, M. A. *J. Chem. Phys.* **1998**, *108*, 8302.

119. Simpson, W. R.; Orr-Ewing, A. J.; Rakitzis, T. P. Kandel, S. A.; Zare, R. N. *J. Chem. Phys.* **1995**, *103*, 7299.

120. Camden, J. P.; Bechtel, H. A.; Brown, D. J. A.; Martin, M. R.; Zare, R. N.; Hu, W.; Lendvay, G.; Troya, D.; Schatz, G. C. *J. Am. Chem. Soc.* **2005**, *127*, 11898; Camden, J. P.; Hu, W.; Bechtel, H. A.; Brown, D. J. A.; Martin, M. R.; Zare, R. N.; Lendvay, G.; Troya, D.; Schatz, G. C. *J. Phys. Chem. A*, **2006**, *110*, 677; Hu, W.; Lendvay, G.; Troya, D.; Schatz, G. C.; Camden, J. P.; Bechtel, H. A.; Brown, D. J. A.; Martin, M. R.; Zare, R. N. *ibid.* **2006**, *110*, 3017.

121. Ahlswede, B.; Jug, K. *J. Comput. Chem.* **1999**, *20*, 563; Jug, K.; Geudtner, G.; Homann, T. *J. Comput. Chem.* **2000**, *21*, 974; Bredow, T.; Geudtner, G.; Jug, K. *J. Comput. Chem.* **2001**, *22*, 89.

122. Becke, A. D. *J. Chem. Phys.* **1993**, *98*, 5648; Lee, C.; Yang, W.; Parr, R. G. *Phys. Rev. B*. **1988**, *37*, 785.

123. Kong, J.; White, C. A.; Krylov, A. I.; Sherrill, C. D.; Adamson, R. D.; Furlani, T. R.; Lee, M. S.; Lee, A. M.; Gwaltney, S. R.; Adams, T. R.; Ochsenfeld, C.; Gilbert, A. T. B.; Kedziora, G. S.; Rassolov, V. A.; Maurice, D. R.; Nair, N.; Shao, Y.; Besley, N. A.; Maslen, P. E.; Dombroski, J. P.; Dachsel, H.; Zhang, W. M.; Korambath, P. P.; Baker, J.; Byrd, E. F. C.; Voorhis, T. V.; Oumi, M.; Hirata, S.; Hsu, C. P.; Ishikawa, N.; Florian, J.; Warshel, A.; Johnson, B. G.; Gill, P. M. W.; Head-Gordon, M.; Pople, J. A. *Q-Chem* **2000**, *version 2.0; Q-Chem, Inc.: Export, PA*.

124. Dewar, M. J. S.; Zoebisch, E. G.; Healy, E. F.; Stewart, J. J. P. *J. Am. Chem. Soc.* **1993**, *115*, 5348.

125. Stewart, J. J. P. *J. Comput. Chem.* **1989**, *10*, 209; **1989**, *10*, 221.

126. Schmidt, M. W.; Baldridge, K. K.; Boatz, J. A.; Elbert, S. T.; Gordon, M. S.; Jensen, J. H.; Koseki, S.; Matsunaga, N.; Nguyen, K. A.; Su, S.; Windus, T. L.; Dupuis, M.; Montgomery, J. A. *J. Comput. Chem.* **1993**, *20*, 1347.

127. Camden, J. P.; Bechtel, H. A.; Brown, D. J. A.; Zare, R. N. *J. Chem. Phys.* **2005**, *123*, 134301.

128. Ayers, J. D.; Pomerantz, A. E.; Fernandez-Alonso, F.; Ausfelder, F.; Bean, B. D.; Zare, R. N. *J. Chem. Phys.* **2003**, *119*, 4662.

129. Troya, D.; Gonzalez, M.; Schatz, G. C. *J. Chem. Phys.* **2001**, *114*, 8397.

130. Shafer, N. E.; Orr-Ewing, A. J.; Simpson, W. R.; Xu, H.; Zare, R. N. *Chem. Phys. Lett.* **1993**, *212*, 155.

131. Simpson, W. R.; Rakitzis, T. P.; Kandel, S. A.; LevOn, T.; Zare, R. N. *J. Phys. Chem.* **1996**, *100*, 7938.

132. Bechtel, H. A.; Camden, J. P.; Brown, D. J. A.; Zare, R. N. *J. Chem. Phys.* **2004**, *120*, 5096.

133. Zhou, J.; Lin, J. J.; Shiu, W.; Pu, S. C.; Liu, K. *J. Chem. Phys.* **2003**, *119*, 2538.

134. Jacobs, A.; Volpp, H. −R.; Wolfrum, J. *Chem. Phys. Lett.* **1994**, *218*, 51.

135. *Evaluated Kinetic Data on Gas Phase Hydrogen Transfer Reactions of Methyl Radicals*, Kerr, J. A.; Parsonage, M. J.   Butterworths, London, 1976.

136. (a) Andresen, P.; Luntz, A. C. *J. Chem. Phys.* **1980**, *72*, 5842; (b) Luntz, A. C.; Andresen, P. *J. Chem. Phys.* **1980**, *72*, 5851.

137. Sweeney, G. M.; Watson, A.; McKendrick, K. G. *J. Chem. Phys.* **1997**, *106*, 9172.; Sweeney, G. M.; McKendrick, K. G. *J. Chem. Phys.* **1997**, *106*, 9182.; Ausfelder, F.; McKendrick, K. G. *Prog. React. Kinet.* **2000**, *25*, 299.

138. Tsurumaki, H.; Fujimura, Y.; Kajimoto, O. *J. Chem. Phys.* **2000**, *112*, 8338.

139. Hartney, M. S.; Hess, D. W.; Soane, D. S. *J. Vac. Sci. Technol. A* **1989**, *7*, 1; Joubert, O.; Pelletier, J.; Arnal, Y. *J. Appl. Phys.* **1989**, *65*, 5096; Chan, C. M.; Ko, T. M.; Hiraoka, H. *Surf. Sci. Rep.* **1996**, *24*, 1; Nguyen, T. P.; Lahmar, A.; Jonnard, P. *J. Adhes.* **1998**, *66*, 303.

140. Herron, J. T.; Huie, R. E. *J. Phys. Chem.* **1969**, *73*, 3327.

141. Kim, P.; Timmons, R. B. *Int. J. Chem. Kinet.* **1975**, *7*, 143.

142. Miyoshi, A.; Tsuchiya, K.; Yamauchi, N.; Matsui, H. *J. Phys. Chem.* **1994**, *98*, 11452.

143. Baulch, D. L.; Cobos, C. J.; Cox, R. A.; Esser, C.; Frank, P.; Just, T. H.; Kerr, J. A.; Pilling, M. J.; Troe, J. J.; Walker, R. W.; Warnatz, J. *J. Phys. Chem. Ref. Data* **1992**, *21*, 468.

144. Minton, T. K.; Garton, D. J. Dynamics of Atomic-Oxygen-Induced Polymer Degradation in Low Earth Orbit, in *Advanced Series in Physical Chemistry: Chemical Dynamics in Extreme Environments*, Dressler, R. A., Ed., World Scientific, Singapore, 2001, pp. 420-489.

145. Jursa, A. *U. S. Standard Atmosphere*, U. S. Government Printing Office, Washington, DC, 1976.

146. Leger, L. J.; Visentine, J. T. *J. Spacecraft* **1986**, *23*, 505.

147. Leger, L. J. *Oxygen Atom Reaction with Shuttle Materials at Orbital Altitudes*, NASA Technical Memorandum 58246, NASA, Houston, TX, 1982.

148. (a) Garton, D. J.; Minton, T. K.; Troya, D.; Pascual, R.; Schatz, G. C. *J. Phys. Chem. A* **2003**, *107*, 4583; (b) Troya, D.; Pascual, R.; Garton, D. J.; Minton, T. K.; Schatz, G. C. *J. Phys. Chem. A* **2003**, *107*, 7161; (c) Troya, D.; Pascual, R.; Schatz, G. C. *J. Phys. Chem. A* **2003**, *107*, 10497; (d) Troya, D.; Schatz, G. C.; Garton, D. J.; Brunsvold, A. L.; Minton, T. K. *J. Chem. Phys.* **2004**, *120*, 731.

149. Troya, D.; Schatz, G. C. *J. Chem. Phys.* **2004**, *120*, 7696.

150. Mahmud, K.; Marshall, P.; Fontijn, A. *J. Chem. Phys.* **1988**, *88*, 2393.

151. Miyoshi, A.; Tsuchiya, K.; Yamauchi, N.; Matsui, H. *J. Phys. Chem.* **1994**, *98*, 11452.

152. Yan, T.; Hase, W. L.; Doubleday, C. *J. Chem. Phys.* **2004**, *120*, 9253.

153. Gindulyte, A.; Massa, L.; Banks, B. A.; Rutledge, S. K. *J. Phys. Chem. A* **2000**, *104*, 9976.

154. Zhang, J.; Garton, D. J.; Minton, T. K. *J. Chem. Phys.* **2002**, *117*, 6239.

155. Lee, Y. T.; McDonald, J. D.; LeBreton, P. R.; Herschbach, D. R. *Rev. Sci. Instrum.* **1969**, *40*, 1402; O'Loughlin, M. J.; Reid, B. P.; Sparks, R. K. *J. Chem. Phys.* **1985**, *83*, 5647.

156. Caledonia, G. E.; Krech, R. H.; Green, D. B. *AIAA J.* **1987**, *25*, 59.

157. Lee, Y. T. in *Atomic and Molecular Beam Methods*, Scoles, G., Ed., Oxford University Press, New York, 1988, Vol. 1, Chap. 22, pp. 553-568.

158. Blank, D. A.; Hemmi, N.; Suits, A. G.; Lee, Y. T. *Chem. Phys.* **1998**, *231*, 261.

159. DeMore, W. B.; Sander, S. P.; Golden, D. M.; Hampson, R. F.; Kurylo, M. J.; Howard, C. J.; Ravishankara, A. R.; Kolb, C. E.; Molina, M. J. *Chemical Kinetics and Photochemical Data for Use in Stratospheric Modeling*, Evaluation No. 11, JPL Publ. 94-26, NASA Panel for Data Evaluation, Jet Propulsion Laboratory, California Institute of Technology, Pasadena, 1994.

160. Troya, D.; Schatz, G. C. *Int. Rev. Phys. Chem.* **2004**, *23*, 341.

161. Lu, D.-H.; Hase, W. L. *J. Chem. Phys.* **1989**, *91*, 7490.

162. Gardiner, W. C., Jr. *Gas-Phase Combustion Chemistry*; Springer-Verlach: New York, 2000.

163. Cvetanović, R. J. *J. Chem. Phys.* **1955**, *23*, 1375; Cvetanović, R. J. *Advan. Photochem.* **1963**, *1*, 115; Cvetanović, R. J. *J. Phys. Chem.* **1970**, *74*, 2730.

164. Casavecchia, P.; Capozza, G.; Segoloni, E.; Leonori, F.; Balucani, N.; Volpi, G. G. *J. Phys. Chem. A*. **2005**, *109*, 3527, and the references therein.

165. Bader, R. F. W.; Stephens, M. E.; Gangi, R. A. *Can. J. Chem.* **1977**, *55*, 2755.

166. Dupuis, M.; Wendoloski, J. J.; Takada, T.; Lester, W. A., Jr. *J. Chem. Phys.* **1982**, *76*, 481.

167. Wortmann-Saleh, D.; Engels, B.; Peyerimhoff, S. D. *J. Phys. Chem.* **1994**, *98*, 9541.

168. Baulch, D. L.; Cobos, C. J.; Cox, R. A.; Frank, P.; Hayman, G.; Just, Th.; Kerr, J. A.; Murrells, T.; Pilling, M. J.; Troe, J.; Walker, R. W.; Warnatz, J. *J. Phys. Chem. Ref. Data* **1994**, *23*, 847.

169. Yamaguchi, K.; Yabushita, S.; Fueno, T. Kato, S.; Morokuma, K. *Chem. Phys. Lett.* **1980**, *70*, 27.

170. Fueno, T.; Takahara, Y.; Yamaguchi, K. *Chem. Phys. Lett.* **1990**, *167*, 291.

171. Melius, C. F. unpublished results cited in Schmoltner, A. M., Chu, P. M.; Brudzynski, R. J.; Lee, Y. T. *J. Chem. Phys.* **1989**, *91*, 6926.

172. Jursic, B. S. *THEOCHEM* **1999**, *492*, 85.

173. Smith, B. J.; Nguyen, M. T.; Bouma, W. J.; Radom, L. *J. Am. Chem. Soc.* **1991**, *113*, 6452.

174. Joshi, A.; You, X.; Barckholtz, T. A.; Wang, H. *J. Phys. Chem. A*. **2005**, *109*, 8016.

175. Nguyen, T. L.; Vereecken, L.; Hou, X. J.; Nguyen, M. T.; Peeters, J. *J. Phys. Chem. A*. **2005**, *109*, 7489.

176. (a) Hoffmann, M. R.; Schatz, G. C. *J. Chem. Phys.* **2000**, *113*, 9456; (b) Maiti, B.; Schatz, G. C. *J. Chem. Phys.* **2003**, *119*, 12360; (c) Maiti, B.; Schatz, G. C.;

Lendvay, G. *J. Phys. Chem. A*. **2004**, *108*, 8772.

177. Stine, J. R.; Muckerman, J. T. *J. Chem. Phys*. **1976**, *65*, 3975; **1978**, *68*, 185.

178. Knuts, S.; Minaev, B.; Vahtras, O.; Ågren, H. *Int. J. Quant. Chem*. **1995**, *55*, 23.

179. Fedorov, D. G.; Gordon, M. S. *J. Chem. Phys*. **2000**, *112*, 5611.

180. Dunning, T. H., Jr. *J. Chem. Phys*. **1989**, *90*, 1007.

181. Zhu, C.; Nakamura, H. *J. Chem. Phys*. **1995**, *102*, 7448; **1997**, *106*, 2599; Zhu, C.; Teranishi, Y.; Nakamura, H. *Adv. Chem. Phys*. **2001**, *117*, 127.

182. Gray, S. K.; Petrongolo, C.; Drukker, K.; Schatz, G. C. *J. Phys. Chem.* **1999**, *103*, 9448; Gray, S. K.; Balint-Kurti, G. G.; Schatz, G. C.; Lin, J. J.; Liu, X.; Harich, S.; Yang, X. *J. Chem. Phys.* **2000**, *113*, 7330.

Vita

This thesis is based on the following published and unpublished papers:

1. **Hu, W.**; Schatz, G. C., "Theories of Reactive Scattering", *J. Chem. Phys.*, **2006**, *125*, 132301.
2. Camden, J. P.; **Hu, W.**; Bechtel, H. A.; Brown, D. J. A.; Martin, M. R.; Zare, R. N.; Lendvay, G.; Troya, D.; Schatz, G. C., "H + CD$_4$ Abstraction Reaction Dynamics: Excitation Function and Angular Distributions", *J. Phys. Chem. A*, **2006**, *110*, 677.
3. **Hu, W.**; Lendvay, G.; Troya, D.; Schatz, G. C.; Camden, J. P.; Bechtel, H. A.; Brown, D. J. A.; Martin, M. R.; Zare, R. N., "H + CD$_4$ Abstraction Reaction Dynamics: Product Energy Partitioning", *J. Phys. Chem. A,* **2006**, *110*, 3017.
4. Camden, J. P.; Bechtel, H. A.; Ankeny Brown, D. J.; Martin, M. R.; Zare, R. N.; **Hu, W.**; Lendvay, G.; Troya, D.; Schatz, G. C., "A Reinterpretation of the Mechanism of the Simplest Reaction at an sp3-Hybridized Carbon Atom: H + CD$_4$ → CD$_3$ + HD", *J. Am. Chem. Soc.* **2005**, *127*, 11898.
5. Garton, D. J.; Minton, T. K.; **Hu, W.**; Schatz, G. C., "Experimental and Theoretical Investigations of the Inelastic and Reactive Scattering Dynamics of O (^{3}P) Collisions with C$_2$H$_6$", in preparation.
6. **Hu, W.**; Lendvay, G.; Maiti, B.; Schatz, G. C., "A Trajectory Surface Hopping Study of the O (^3P) + Ethylene Reaction Dynamics", in preparation.